Spring 1988

Investigation of Supersonic Chemically Reacting and Radiating Channel Flow

Mortaza Mani
Old Dominion University

INVESTIGATION OF SUPERSONIC CHEMICALLY REACTING AND RADIATING CHANNEL FLOW

By

Mortaza Mani
B.S., Mechanical Engineering, December 1977
Kansas State University

M.S., Mechanical Engineering, December 1982
Kansas State University

A Dissertation Submitted to the Faculty of
Old Dominion University in Partial Fulfillment of the
Requirements for the Degree of

DOCTOR OF PHILOSOPHY

MECHANICAL ENGINEERING

OLD DOMINION UNIVERSITY
May 1988

Approved By:

Dr. Surendra N. Tiwari (Director)

Dr. Oktay Baysal

Dr. J. Philip Drummond

Dr. J. Mark Dorrepaal

Dr. Ernst von Lavante

ABSTRACT

Mortaza Mani
Old Dominion University, 1988
Director: Dr. Surendra N. Tiwari

The two-dimensional time dependent Navier-Stokes equations are used to investigate supersonic flows undergoing finite rate chemical reaction and radiation interaction for a hydrogen-air system. The explicit multi-stage finite volume technique of Jameson is used to advance the governing equations in time until convergence is achieved. The chemistry source term in the species equation is treated implicitly to alleviate the stiffness associated with fast reactions. The multi-dimensional radiative transfer equations for a nongray model are provided for a general configuration, and then reduced for a planer geometry. Both pseudo-gray and nongray models are used to represent the absorption-emission characteristics of the participating species.

The supersonic inviscid and viscous, nonreacting flows are solved by employing the finite volume technique of Jameson and the unsplit finite difference scheme of MacCormack. The specific problem considered is of the flow in a channel with a ten degree compression-expansion ramp. The calculated results are compared with the results of an upwind scheme. The problem of chemically reacting and radiating flows are solved for the flow of premixed hydrogen-air through a channel with parallel boundaries, and a channel with a compression corner. Results obtained for specific conditions indicate that the radiative interaction can have a significant influence on the entire flow field.

ACKNOWLEDGEMENTS

I would like to express my sincere appreciation to Professor S. N. Tiwari for his guidance, valuable suggestions and continuous encouragement during my coursework and throughout my research. I would also like to thank my committee members, Drs. von Lavante, Baysal and Dorrepaal for their help; my gratitude is greatest to Dr. J. P. Drummond of NASA Langley for his guidance, helpful discussion, support and continuous encouragement during the course of this study. I extend my thanks to NASA Langley for giving me the opportunity to use the excellent computer facilities.

I would like to thank my friends Dr. J. S. Abolhassani and Mr. K. Daryabeigi for copying and delivering this dissertation and contributing their valuable time to the preparation of this manuscript; I am greatful for their help in every way possible to me during this period. Special thanks goes to Ms. Diane Riddick for typing my work.

But most of all, I would like to thank my wife Marcia and my children Rosaly and Camran, to whom this work is dedicated, for their patience and continuous support.

This work was supported by the NASA Langley Research Center through grants NAG-1-363 and NAG-1-423.

TABLE OF CONTENTS

LIST OF TABLES

LIST OF FIGURES

LIST OF SYMBOLS

A	band absorptance, m^{-1}
A_o	band width parameter, m^{-1}
C_j	concentration of the jth species, kg-mole/m^3
C_o	correlation parameter, $(N/m^2)^{-1}\ m^{-1}$
C_p	constant pressure specific heat, J/Kg-K
D	diffusion coefficient
e_b	black body radiation, $\sigma\ T^4$, J/m^2-s
e_ω	Planck's function, J/m^2-s
E	total internal energy, J/Kg
f_j	mass fraction of the jth species
h	static enthalpy of mixture, J/Kg
H	total enthalpy, J/kg
I	identity matrix
I_ν	spectral intensity, J/m-s
$I_{b\nu}$	spectral Planck function
$I_{\nu c}$	spectral intensity evaluated at ν_c, J/m-s
$I_{b\nu c}$	spectral Planck function evaluated at ν_c, J/m-s
k	thermal conductivity, J/m-s-K
K_b	backward rate constant
K_f	forward rate constant
$\vec{\ell}$	unit vector in the direction of $\overline{PP}_w$
M_j	molecular weight of the jth species, kg/kg-mole
P	pressure or a point, N/m^2

P_j	partial pressure of the jth species, N/m^2
P_e	equivalent broadening pressure ratio
Pr	Prandtl number
P_w	a point on the wall
q_R	total radiative heat flux, J/m^2-s
q_{R_ω}	spectral radiative heat flux
R	gas constant, J/kg-K
r_w	distance between the points P and P_w, m
S	integrated band intensity, $(N/m^2)^{-1}$-m^{-2}
T	temperature, K
u	velocity in x and y direction, m/s; dimensionless coordinate = SPy/A_o
v	velocity in y direction, m/s
$\dot{w}_j$	production rate of the jth species, kg/m^3-s
x,y	physical coordinate, m
z	dummy variable in the y direction, m

Greek symbols

α	heat diffusion
γ	ratio of specific heats
Δt_{ch}	chemistry time step, s
Δt_f	fluid-dynamic time step, s
κ	absorption coefficient
$\kappa_\lambda, \kappa_\nu$	spectral absorption coefficient, m^{-1}
κ_p	Planck mean absorption coefficient
λ	second coefficient of visocity, wave length, m
μ	dynamic viscosity (laminar flow), kg/m-s
ξ,η	computational coordinates

ρ	density, kg/m^3
σ	Stefan-Boltzmann constant, $erg/s\text{-}cm^2\text{-}K^4$
τ	shear stress, N/m^2
τ_ω	optical thickness
ϕ	equivalence ratio
ω	wave number, m^{-1}
Ω	solid angle in Chap. 3
ν_c	frequency at the band center

Chapter 1

INTRODUCTION

In the last several years, there has been a great deal of research toward development of a hypersonic transatmospheric vehicle. At the NASA Langley Research Center, the hydrogen-fueled supersonic combustion ramjet (scramjet) engine has been a strong candidate for propelling such a vehicle. Both experimental and numerical techniques are being employed for a better understanding of the complex flow field in different regions of the engine. Numerical modeling of the flow in various sections has proven to be a valuable tool for gaining more insight into the complex nature of these flows [1-5]*.

During the past two decades, a tremendous progress has been made in the field of radiative energy transfer in nonhomogeneous nongray gaseous systems. In recent years, radiation heat transfer has received attention because of its application in fire and combustion research, entry and reentry phenomena, and hypersonic propulsion. In the hypersonic propulsion system, the temperature ranges from 1000-5000 K. In this range, various nonsymmetric molecules such as H_2O, CO_2 and OH become highly radiative participating. Infrared absorption and emission of thermal radiation is a consequence of coupled vibrational and rotational energy transitions. Diatomic molecule is the simplest

*The numbers in brackets indicate references.

molecule that will undergo such transitions. However, symmetric diatomic molecules, such as H_2, O_2 and N_2, have no permanent dipole moment and thus are transparent to infrared radiation. For unsymmetric diatomic and triatomic molecules, such as OH, CO, CO_2 and H_2O, the infrared spectrum will consist of fundamental vibration-rotation bands occurring at the fundamental vibrational frequencies of the molecule followed by the overtone and combination bands [6].

In the past, radiative transfer analysis, due to the complexity of the formulations and the computer resource requirements, was limited to one-dimensional formulations. Even for one-dimensional cases, the non-gray radiative heat transfer calculations required enormous amount of computational time. Important works in nongray one-dimensional formulation are reviewed in Refs. 6-9.

Since the late 1960's, efforts have been directed toward formulating efficient and accurate multi-dimensional equations for radiative transfer. Latko and Pomraning [10] suggested a synthesis method for solving two-dimensional time dependent radiative transfer equations. The synthesis method is an attempt to reduce the computer time requirements by constructing the two-dimensional problem from a small number of one-dimensional calculations. The method is alternated from cycle to cycle. On odd cycles, the two-dimensional calculation is constructed from N one-dimensional x-direction (y=const.) cuts. On even cycles, the two-dimensional calculation is constructed from M one-dimensional y-direction (x-const.) cuts. Berg and Crosbie [11] developed an exact formulation for the radiative flux and emissive power for a two-dimensional finite planer, absorbing-emitting gray medium in radiative equilibrium. Exact expressions were obtained for a medium

subjected to the following types of boundary conditions: (A) cosine varying collimated radiation, (B) a strip of collimated radiation, (C) cosine varying diffuse radiation, and (D) a uniform temperature strip. The solution for the cosine varying collimated radiation model was used to construct the solutions for the other boundary conditions. The two-dimensional equations were reduced to one-dimensional equations by the method of separation of variables.

Tsai and Chan [12] presented a general formulation of radiative heat flux and its divergence for multi-dimensional radiative problems involving nongray absorbing-emitting gases. The expressions obtained are in terms of total band absorptance rather than the spectral absorption coefficients. Thus the expressions are more compact. Modest [13] developed a new multi-dimensional model to calculate the spectrally-integrated total radiative-flux for a molecular gas band based on the solution of two simple differential equations. This model employs the exponential-wide band model and, therefore, considerably reduces the numerical efforts required. Yuen and Wong [14] solved two-dimensional radiative transfer equations for gray medium by a point alocation method in which the temperature profile is expressed as a polynomial of a successively higher order. It was shown that the technique provides a rapid convergence in comparison to the Hottel's Zonal Method [15] with the same number of unknowns. Their approach represents a reduction in computational time by about one order of magnitude. This technique requires the evaluation of finite number of single integrals for a complete solution to the problem.

In the combustion temperature range, some diatomic and triatomic molecules are highly radiative participating species. Various

investigators have studied the effect of radiative transfer for channel flows. Martin and Hwuang [16] solved the energy equation for steam flowing between two parallel black walls. The flow was assumed to be steady and the radiation transfer in the flow direction was neglected. It was shown that the radiative flux peaks at a small distance from the wall, instead of at the wall. This effect was also noted by Viskanta in a gray analysis of radiation and convection between plates of constant temperatures [17]. This is because at the wall the effect of positive radiant heat flux from the wall is partially cancelled by the negative flux from the layers of hot gas next to the wall. At small distances into the stream, however, the flux from both the wall and the hot gas combine to give a maximum heat flux. Kobiyama et al. [18] studied the problem of combined radiation and convection for compressible laminar flow between two isothermal parallel plates. A comparison between temperature profiles calculated with the treatment of one- and two-dimensional radiation shows a considerable temperature difference at the entrance region of the heating zone. The problem of combined convection and radiation in a rectangular duct was also studied by Im and Ahluwalia [19] for compressible turbulent flows. The moment method was employed in this study to solve the radiative flux equation. This method reduces the general radiation transport equations to a set of equations in x, y, and z directions. It was concluded that the radiative transfer causes the thermal boundary layer to grow and skin friction to decrease. The velocity profile was not affected by the radiative heat transfer.

Chung and Kim [20] solved a two-dimensional combined mode heat transfer problem by using the finite element technique. The effect of scattering was also included in the radiative formulation. It was

concluded that the standard Galerkin finite elements may be used if the convection domination is relatively small (Re Pr < 1000). If conduction energy transfer dominates over radiation, there are few effects of optical thickness on the temperature profile in the absence of scattering. For converging channels, the radiation effect on the temperature profiles is insignificant even when conduction and convection are small.

Tiwari and Singh [21, 22] investigated the transient radiative interactions of nongray absorbing-emitting species in laminar fully developed flows between two parallel plates. The particular species considered were OH, CO, CO_2, H_2O and different mixture of these species. Their results demonstrated that, H_2O is a highly radiation participating species as compared to CO_2, CO and OH. The effects of radiation increase with increasing plate spacing, and the radiative transfer is more pronounced at higher wall temperatures and pressures. It was also shown that optically thin limits overestimate the influence of radiation. Soufiani and Taine [23] studied the H_2O-air mixtures for the above geometry and reached the same conclusions.

James and Edwards [24] added the nongray radiation described by the exponential model for molecular gas bands to the numerical solution of turbulent combustion of methane in a planner, enclosed, jet-diffusion flame. The planner jet of methane was injected with velocity U_{fuel} into a stream of air flowing with velocity U_{air} parallel to the fuel. Diffusion-controlled combustion occurred in the mixing region of the jet. Plane-parallel isothermal black walls symmetrically located above and below the jet formed the combustion chamber. A soot-free flame was assumed to exist so that the molecular gas bands determined the thermal

radiative transfer to the walls. In this study, 40 percent of the computation time was devoted to the radiation calculation. The goal of the study was to show the effect of radiation upon combustion temperatures for different channel sizes. Three channel widths of 0.2, 2.0 and 20.0 meters were selected. It was noted that as the channel width reduced, the effects of radiation were also reduced, and for the channel width of 0.2m, there was no effect on the temperature profile.

For the numerical investigation of chemically reacting and radiating flows, an appropriate chemistry model must also be selected. Depending on the ratio of the chemical and fluid dynamic time scales, the suitable chemistry model could be a frozen flow model, a finite rate model, an equilibrium model, or a complete reaction model. In general, the finite-rate model is the most accurate one. In the last several years, a number of finite rate chemistry models for hydrogen-air systems have been introduced in the literature. Rogers and Schexnayder [25] proposed as many as 60 reaction paths in their model; this is certainly one of the most complete representatives of hydrogen-air reaction. Unfortunately, the enormous number of reaction paths and chemical species involved in the model makes it unfeasible for numerical investigation of engineering problems. Intermediate level models are reduced to 12 species, 25 reaction paths, eight species and eight reaction paths [26]. Except for some inaccuracies during the ignition delay period, the eight reaction models perform as well as the 25-reaction path model. Although these models are less tedious than the 60-path model, they are expected to be too costly for use in routine parametric studies. The global two-step chemistry model of Rogers and Chinitz [27] is an inexpensive and attractive model for primary

investigation of reacting flows. This model was deduced by fitting the temperature history of a 28-reaction model [25] used in a series of constant-pressure stream-tube calculations. There are a number of limitations to this model, such as ignition phase inaccuracy and a tendency to overpredict the flame temperature. But as pointed out earlier, it is considered to be an appropriate model for the initial parametric study of overall mixing and extent of combustion.

The global two-step chemistry model was used successfully by several investigators to solve chemically reacting supersonic flows. Drummond et al. [2] used the global chemistry model to solve the flow in a rapid expansion nozzle. The governing equations describing the flow were solved by the two-stage Runge-Kutta method for integrating in time, and a Chebyshev spectral method for integrating the equations in space. The results were compared with the two finite difference schemes of Adam-Moulton and MacCormack. The comparison showed that the spectral method with the Runge-Kutta Scheme gives the same accuracy on much coarser grids as compared to the finite-difference procedure. This results in a significant gain in the computational efficiency. Bussing and Murman [28] solved the time-dependent Navier-Stokes equations for supersonic reacting flows. Several efficient acceleration techniques were used for calculating steady state chemically reacting supersonic flows. The techniques included preconditioning the conservation equations, and a preconditioned multiple-grid accelerator. Chitsomboon et al. [4] used two-dimensional parabolized Navier-Stokes and parabolized species equations to investigate supersonic chemically reacting flows related to scramjet-engine configurations. A linearized, fully-coupled, fully-implicit finite difference algorithm was used to

develop a computer code to solve the governing equations by marching in space rather than time. Results obtained by using the parabolized formulation were compared with the results obtained by using the elliptic equations. The comparisons indicated fairly good agreement between the results of the two formulations.

A more realistic chemistry model was used by Drummond [5] in numerical simulation of a supersonic chemically reacting mixing layer. To explore the behavior of such flows, detailed physical models of convective and diffusive mixing and finite rate chemical reaction in supersonic flow were developed. The finite rate chemistry model consisted of eighteen reaction paths and nine species. In this study, two numerical algorithms were constructed to solve the governing equations. The first algorithm was developed by modifying the unsplit finite difference scheme of MacCormack. The second algorithm employed a hybrid pseudo-spectral technique in the normal direction to the flow for improved resolution of the reacting flow field. The finite difference scheme was used in the streamwise direction. It was suggested that more attention be given to the development of spectral methods that could be more easily applied to high gradient regions like shocks in supersonic reacting flows. The case considered with the spectral method was shockless and a small degree of damping was applied in the regions of high gradients. Several important conclusions were drawn from this study, and interested readers should refer to Ref 5. Here, it is important to point out that the use of a more complete chemistry model rather than the global model in the fluid dynamics equations did not result in a set of temporally stiff equations.

Incorporation of the finite rate chemistry model into the fluid dynamics equations can create a set of stiff differential equations. The stiffness is due to a disparity in the time scales of the governing equations. In the time-accurate solution, after the fast transients have decayed and solutions are changing slowly, taking a larger time step is necessary for efficiency purposes, but explicit methods still require small time steps to maintain stability. An eigenvalue problem associated with stiff ordinary differential equations (ODE) has been solved to express this point clearly in [29]. The literature related to stiff differential equations is not reviewed in this study, but there are interesting reviews of this topic available in Refs. 29 and 30. One way around the problem is to use a fully implicit method. This method, however, requires the inversion of a block multi-diagonal system of algebraic equations. The use of a semi-implicit technique, suggested by several investigators [28, 31, 32], provides an alternative to the above problems. In this technique, the source term which is the cause of the stiffness is treated implicitly, and other terms in the governing equations are treated explicitly.

The literature survey indicates that a great deal of effort has been directed toward the formulation of radiative heat transfer equations. Most applications of these formulations have been restricted to nonreacting homogeneous systems. Only a limited number of studies are available on applications of radiative energy transfer in combustion processes rocket exhaust plume analyses, and fire research. Virtually no efforts have been made to investigate the interaction of radiation heat transfer in chemically reacting, viscous, subsonic and supersonic flows of molecular species.

The objective of this study is to investigate the effects of radiative heat transfer in chemically reacting supersonic flow in a scramjet combustor. The products of hydrogen-air combustion are gases such as water vapor and hydroxyl radical. These species are highly absorbing and emitting. The presence of such gases makes the study of radiative heat transfer in chemically reacting flows an important issue. It is essential to employ an accurate and nonoscillatory numerical scheme to solve the governing equations involving radiative heat transfer. This is because the rate of radiative heat transfer is influenced strongly by the temperature and pressure of the medium. Consequently, another objective of this study is to explore the feasibility of employing the Jameson's four-stage Runge-Kutta time stepping scheme [33] for the solution of chemically reacting and radiating viscous flows. This scheme has proven to be efficient and robust for the solution of the Euler equations. For the steady state solution, various techniques can be implemented to accelerate the convergence [34-36].

A brief discussion of the scramjet engine and the governing equations are presented in Chap. 2. Chapter 3 provides the formulation for nongray, pseudo-gray, and optically thin radiation models. The grid generation technique and solution procedures for the governing equations are presented in Chap. 4. Discussion of the results for several specific cases are provided in Chap. 5, and specific conclusions and recommendations for future studies are provided in Chap. 6.

Chapter 2

GENERAL FORMULATION

A brief discussion is presented on various components of the scramjet engine. Special attention is directed to discussion of the basic equations that are applicable in analyzing the flow field in different parts of the engine. The relations for the thermodynamic and chemistry models are also provided in this section.

2.1 Physical System and Model

As mentioned in the introduction, the scramjet engine has been a candidate for propelling hypersonic vehicles. In Fig. 2.1, various air-breathing and rocket propulsion alternatives are shown [37, 38]. For Mach numbers of zero to three, turbojet air-breathing systems have the highest performance. Above Mach number of three, turbine inlet temperatures constrain performance, and then the ramjet becomes more attractive. At about a Mach number of six, the performance of the ramjet is greatly reduced. This is due to dissociation of the reaction products, which is caused by slowing the supersonic flow to subsonic flow through the normal shock that exists in a ramjet. Therefore, it is more efficient to allow the engine internal flow to remain at a supersonic speed. Thus for Mach numbers of six and beyond, the fixed geometry scramjet is clearly superior for propelling a vehicle at hypersonic speed. Hydrogen has been selected as the fuel for the scramjet due to its capability of cooling the engine and the airframe and also because of its high impulse level.

The scramjet engine is made up of several identical modules and it is installed underneath the aircraft as shown in Fig. 2.2. Each module is made up of inlet, combustor and nozzle regions. As part of the engine design concept [37], the forebody of the aircraft acts as an inlet for precompression and the afterbody as a nozzle for post expansion.

The inlet region starts with the forebody of the vehicle and ends up with the minimum cross sectional area of each module. In the first part, the air flow is compressed by the oblique shock generated from the forebody before it enters the engine. For numerical solution, the flow is best represented by the Navier-Stokes equation in the actual inlet area of the engine. Using the Euler equation away from the wall and the boundary layer equation near the wall region can be complicated by oblique shock interaction with the boundary layer. This can cause flow separation, which means flow can not be represented accurately by these equations. Three-dimensional Navier-Stokes equations have been employed by Kumar [1] to investigate the flow field in this region with reasonable success. Chitsomboon et al. [4] have employed the parabolized Navier-Stokes equations with limited success.

The combustor region is by far the most complex part of the scramjet engine. As a result, a great deal of research is directed toward better understanding of the combustor flow field. The flow in this region is nearly supersonic, but does have subsonic regions near fuel injections (Fig. 2.3). The fluid dynamics become complicated by the fuel injection, flame holding, chemistry, radiation and turbulence. The flow field in this region is represented by the Navier-Stokes equations (including turbulence, chemistry and radiation). In

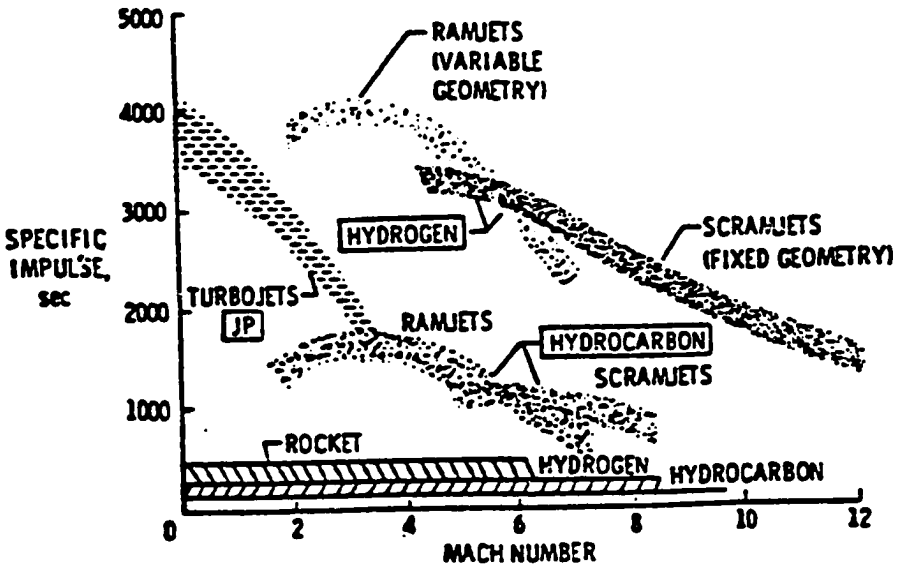

Fig. 2.1 Propulsion alternatives.

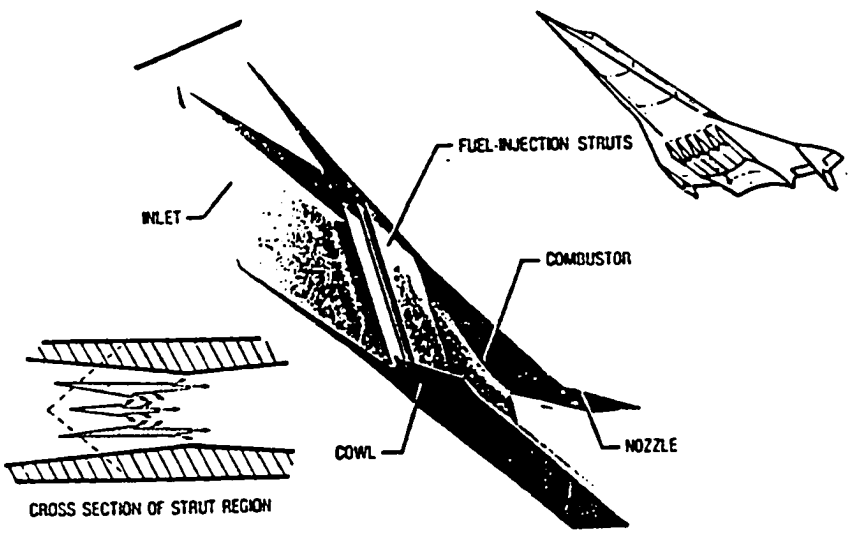

2.2 Airframe-integrated supersonic combustion.

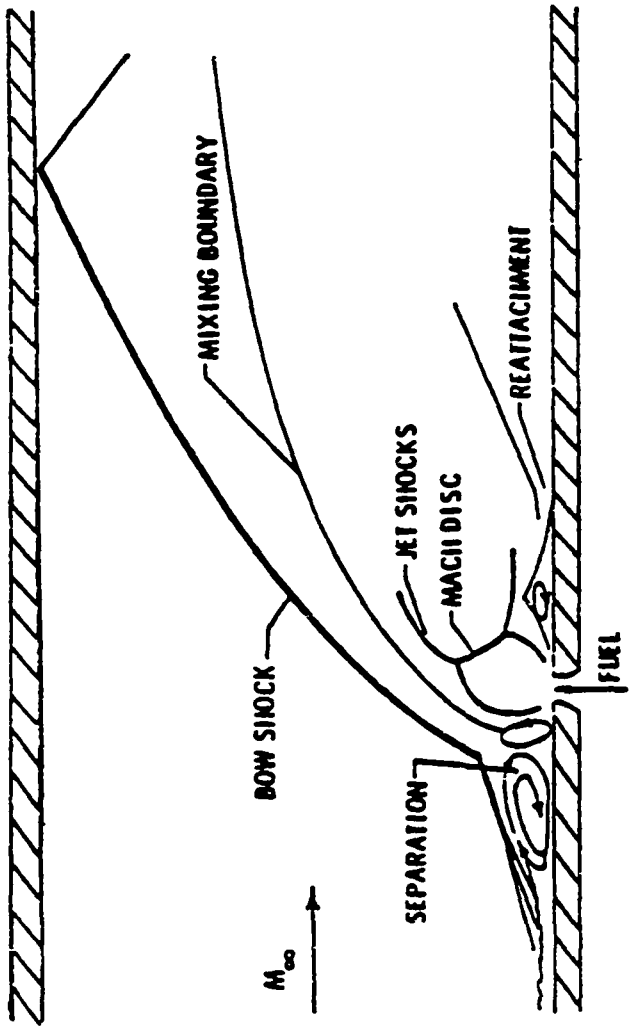

Fig. 2.3 Flow field near an injector.

the farfield (downstream of the fuel injection strut, where the flow is only supersonic), the flow can be represented by the parabolized Navier-Stokes equations [4].

The nozzle and subsurface of the afterbody provide about fifty percent of the thrust at Mach number six [38]. The flow through the nozzle is supersonic. The combustor exit flow consists of multicomponents of the reacting species, multiple shock, and 3-D viscous effects. For engineering accuracy, the flow can be represented by the parabolized Navier-Stokes equations.

2.2 Basic Governing Equations

The two-dimensional Navier-Stokes and species continuity equations are represented in the physical domain by

$$\frac{\partial U}{\partial t} + \frac{\partial F}{\partial x} + \frac{\partial G}{\partial y} + H = 0 \tag{2.1}$$

where vectors U, F, G and H are expressed as

$$U = \begin{bmatrix} \rho \\ \rho u \\ \rho v \\ \rho E \\ \\ \rho f_j \end{bmatrix} \qquad F = \begin{bmatrix} \rho u \\ \rho u^2 + \tau_{xx} \\ \rho uv + \tau_{xy} \\ (\rho E + \tau_{xx})\, u + \tau_{xy}\, v + q_{cx} + q_{rx} \\ \rho u f_j - \rho D \dfrac{\partial f_j}{\partial x} \end{bmatrix}$$

$$G = \begin{bmatrix} \rho v \\ \rho uv + \tau_{yx} \\ \rho v^2 + \tau_{yy} \\ (\rho E + \tau_{yy})\, v + \tau_{xy}\, u + q_{cy} + q_{ry} \\ \rho v f_j - \rho D \dfrac{\partial f_j}{\partial y} \end{bmatrix} \qquad H = \begin{bmatrix} 0 \\ 0 \\ 0 \\ 0 \\ -\dot{W}_j \end{bmatrix}$$

The viscous stress tensors in the F and G terms of Eq. (2.1) are given as

$$\tau_{xx} = P - \lambda\left(\frac{\partial u}{\partial x} + \frac{\partial v}{\partial y}\right) - 2\mu \frac{\partial u}{\partial x} \tag{2.2a}$$

$$\tau_{xy} = -\mu\left(\frac{\partial u}{\partial y} + \frac{\partial v}{\partial x}\right) \tag{2.2b}$$

$$\tau_{yy} = P - \lambda\left(\frac{\partial u}{\partial x} + \frac{\partial v}{\partial y}\right) - 2\mu \frac{\partial v}{\partial y} \tag{2.2c}$$

The quantities q_{cx} and q_{cy} in the F and G terms are the components of the conduction heat flux and are expressed as

$$q_{cx} = -k \frac{\partial T}{\partial x} - \rho D \sum_{j=1}^{m} [(\partial f_j/\partial x) h_j] \tag{2.3a}$$

$$q_{cy} = -k \frac{\partial T}{\partial y} - \rho D \sum_{j=1}^{m} [\partial f_j/\partial y) h_j] \tag{2.3b}$$

where

$$h_j = h_j^o + \int_{T_o}^{T} C_{p_j}\, dT; \quad T_o = 0 \text{ K}$$

It should be noted here that D represents the effective binary diffusion coefficent and is used for all species. Assuming that the Lewis number (α/D) is unity, Eqs. (2.3) reduce to (see Appendix A)

$$q_{cx} = -\frac{\gamma\mu}{Pr} \frac{\partial e}{\partial x} \tag{2.4a}$$

$$q_{cy} = -\frac{\gamma\mu}{Pr} \frac{\partial e}{\partial y} \tag{2.4b}$$

where

$$e = h - P/\rho$$

The molecular viscosity, μ_ℓ is assumed to be temperature dependent and it is evaluated from the Sutherland's formula as

$$\mu_\ell = \mu_o \left(\frac{T}{T_o}\right)^{3/2} \frac{T_o + S}{T + S} \tag{2.5}$$

where μ_0 and T_0 are reference values for individual species and S is the Sutherland constant. In this study, reference values were selected for pure air because the flow is dominated by nitrogen. The total internal energy E in Eq. (2.1) is given by

$$E = P/\rho + \frac{u^2 + v^2}{2} + \sum_{i=1}^{m} h_i f_i \tag{2.6}$$

Specific relations are needed for the chemistry and thermodynamic models and for the radiative transport. The chemistry and thermodynamic models are discussed briefly in the following sections. The formulations for radiative transport are presented in Chap. 3.

Instead of solving the partial differential equations, sometimes it is desirable to solve the integral form of these equations using the finite volume method. The integral form of the governing equations can be expressed as

$$\frac{\partial}{\partial t} \iint_{\Omega} U dxdy + \int_{\partial\Omega} M \cdot n \, ds + \iint_{\Omega} H \, dxdy = 0 \tag{2.7}$$

where n is a normal vector pointing outward, Ω is the region of interest and $\partial\Omega$ is the boundary curve. In two-dimensions, the volume has a unit depth. The second order tensor M in Eq. (2.7) is defined by

$$M = F \, i_x + G \, i_y \tag{2.8}$$

where F and G are defined in Eq. (2.1). Equation (2.7) can be written in Cartesian form as

$$\frac{\partial}{\partial t} \iint_{\Omega} U dxdy + \int_{\partial\Omega} (Fdy - Gdx) + \iint_{\Omega} H \, dxdy = 0 \tag{2.9}$$

The finite volume formulation is used with the Runge-Kutta time-stepping scheme. The details of the formulation and the solution schemes are presented in Chap. 4.

2.3 Chemistry Model

For the numerical solution of reacting flows, a chemistry model is needed to represent the combustion process. The chemistry model used in this study is the two-step, global, finite-rate, hydrogen-air combustion model developed by Rogers and Chinitz [27]. This chemistry model was deduced from a 28 reaction model and is adequate for initial temperatures between 1,000 K and 2,000 K and for equivalence ratios between 0.2 and 2.0. In the first step, hydrogen and air react and produce hydroxyl radical, and in the second step, hydroxyl radical and hydrogen react to produce water vapor. The reactions are expressed as

$$H_2 + O_2 \underset{K_{b_1}}{\overset{K_{f_1}}{\rightleftharpoons}} 2\ OH \tag{2.10}$$

$$2OH + H_2 \underset{K_{b_2}}{\overset{K_{f_2}}{\rightleftharpoons}} 2\ H_2O \tag{2.11}$$

where K_{f_i} and K_{b_i} represent the forward and reverse reaction rate constants respectively. The relations for K_{f_i} are obtained from an Arhenius equation as

$$K_{f_i} = A_i(\phi)T^{N_i} \exp(-E_i/RT) \tag{2.12}$$

The values of the parameters $A_i(\phi)$, N_i, and E_i in Eq. (2.12) are

$$A_1(\phi) = (8.917\ \phi + 31.433/\phi$$

$$- 28.95)x\ 10^{47} \sim cm^3/g\text{-}mol\text{-}S$$

$$E_1 = 4865\ Cal/mol;\ N_1 = -10.$$

$$A_2(\phi) = (2. + 1.333/\phi$$

$$- .833\phi)x10^{64} \sim cm^6/mol^2 - s$$

$$E_2 = 42500\ Cal/mol;\ N_2 = -13$$

where ϕ is the fuel-air ratio. The reverse rate constants can be evaluated by

$$K_{b_i} = \frac{K_{f_i}}{K_i} \tag{2.13}$$

where

$$K_1 = 26.164\ \exp(-8992/T)$$

$$K_2 = (2.682x10^{-6})\ (T)\ \exp(69415/T)$$

Knowing the reaction rate constant K_{f_i} and K_{b_i} the production of species can be evaluated from the law of mass action. Consider the general chemical reaction

$$\sum_{j=1}^{N} \nu'_{j,i}\ C_j \underset{K_{b_i}}{\overset{K_{f_i}}{\rightleftharpoons}} \sum_{j=1}^{N} \nu''_{j,i}\ C_j \qquad i=1,2,\ldots,m \tag{2.14}$$

where $\nu'_{j,i}$ and $\nu''_{j,i}$ represent the stoichiometric coefficents of the reactants and products respectively and N is the number of species. The

law of mass action states that the rate of change of concentration of species j by reaction i is given by [39]

$$(\dot{C}_j) = (\nu''_{ji} - \nu'_{ji}) \left[K_{f_i} \prod_{j=1}^{N} C_j^{\nu'_{ji}} - K_{b_i} \prod_{j=1}^{N} C_j^{\nu''_{ji}}\right] \tag{2.15}$$

The net rate of production of species j in all reactions is given by

$$\dot{C}_j = \sum_{i=1}^{m} (\dot{C}_j)_i \tag{2.16}$$

where m is the number of reactions. Finally, the chemistry source terms, on a mass basis, are found by multiplying the molar changes and corresponding molecular weight

$$\dot{w}_j = \dot{C}_j M_j \tag{2.17}$$

By applying the law of mass action to the global model, the chemistry source terms of the four species are obtained as

$$\dot{C}_{O_2} = - K_{f1} C_{H_2} C_{O_2} + K_{b_1} C_{OH}^2 \tag{2.18}$$

$$\dot{C}_{H_2O} = 2(K_{f2} C_{OH}^2 C_{H_2} - K_{b_2} C_{H_2O}^2) \tag{2.19}$$

$$\dot{C}_{H_2} = \dot{C}_{O_2} - 1/2 \dot{C}_{H_2O} \tag{2.20}$$

$$\dot{C}_{OH} = - (2 \dot{C}_{O_2} + \dot{C}_{H_2O}) \tag{2.21}$$

where

$$C_j = \rho f_j / M_j$$

2.4 Thermodynamic Model

The specific heat of individual species, C_{p_i}, is assumed to be a linear function of temperature, i.e.,

$$C_{p_j} = a_j T + b_j \tag{2.22}$$

where a_j and b_j are constants which are obtained by curve fitting the thermochemical data of Ref. 40. The numerical values of these constants are given in Table 2.1. The specific heat of the mixture is computed by summing specific heats of individual species weighted by species mass fraction

$$\bar{C}_p = \sum_{j=1}^{m} C_{p_j} f_j \tag{2.23}$$

The static enthalpy of the mixture can be expressed as

$$h = \sum_{j=1}^{m} \left[h_j^o + \int_{T_o}^{T} C_{p_j} dT\right] f_j \tag{2.24}$$

The total enthalpy can now be evaluated as

$$H = h + 0.5 (u^2 + v^2) \tag{2.25}$$

Combining Eqs. (2.22), (2.24) and (2.25), the total enthalpy is expressed as

$$H = \sum_{j=1}^{m} \left[h_j^o + \frac{a_j T^2}{2} + b_j T\right] f_j + 0.5 (u^2 + v^2) \tag{2.26}$$

where h_j^o is the sensible enthalpy of individual species at a reference temperature (T_o = 0 K). The gas constant for the mixture also is evaluated by a mass weighted summation over all the species as

$$\bar{R} = \sum_{j=1}^{m} f_j R_j \tag{2.27}$$

The equation of state for the mixture of the gases therefore can be written as

$$P = \rho \bar{R} T \tag{2.28}$$

Table 2.1 Numerical Values of Various Constants

Species	H°(J/kg)	a	b
O_2	-271267.025	0.119845	947.937
H_2O	-13972530.24	0.43116	1857.904
H_2	-4200188.095	2.0596	12867.46
OH	+1772591.157	0.16564	1672.813
N_2	-309483.98	0.10354	1048.389

Chapter 3

RADIATION TRANSPORT MODELS

In order to include the effects of radiative interaction in a physical problem, it is essential to accurately model the absorption-emission characteristics of participating species and provide a correct formulation of the radiative transfer processes. These are discussed briefly in this section.

3.1 Radiation Absorption Models

Many models are available in the literature to represent the absorption-emission characteristics of molecular species; a review of important models is available in [41]. Perhaps the simplest model is the gray gas model where the absorption coefficient is assumed to be independent of the wavelength. Many nongray models are also available in the literature. Both gray and nongray absorption models are discussed here briefly.

3.1.1 Gray Gas Models

In the gray model, it is assumed that the absorption coefficient is independent of the wavelength. This is rarely a physically realistic approximation, but it serves as an initial step for studying the effect of radiative heat transfer. The absorption coefficient for the gray gas is evaluated by employing the Planck mean absorption coefficient defined as

$$\kappa_p = \frac{\int_0^\infty \kappa_\omega \, e_{b\omega}(T) \, d\omega}{e_b(T)} \tag{3.1}$$

By assuming that within a band the Planck function does not vary significantly with the wave number, and by evaluating its value at the band center, the relation for κ_p for a single-band gas can be written as

$$\kappa_p = \frac{e_{b\omega_c}(T)}{\sigma T^4(y)} \int_{\Delta\omega} \kappa_\omega \, d\omega \tag{3.2}$$

where ω_c represents the band center. For a multiband gaseous system of n gases, κ_p is given by

$$\kappa_p = \sum_{k=1}^{n} \left[\frac{e_{b\omega_k}(T)}{\sigma T^4(y)} \int_{\Delta\omega} \kappa_\omega \, d\omega\right] \tag{3.3}$$

where ω_k represents the band center of the kth band of a particular species. For a specific band of a given gas, the integrated band intensity S_k is defined as

$$S_\kappa = \frac{1}{P_j} \int_{\Delta\omega} \kappa_\omega \, d\omega \tag{3.4}$$

Substituting Eq. (3.4) into Eq. (3.3), κ_p is expressed as

$$\kappa_p = \frac{P_j}{\sigma T^4(y)} \sum_{k=1}^{n} e_{b\omega_k}(T) \, S_k(T) \tag{3.5}$$

where

$$e_{b\omega_k}(T) = \frac{C_1 \omega_k^3}{\exp\left[C_2 \omega_k / T\right] - 1}$$

In Eq. (3.5), P_j is species partial pressure, and C_1 and C_2 are constants [6]. Note that κ_p is a function of temperature and species partial pressure.

3.1.2 Nongray Gas Models

Important nongray models available in the literature are as follows:

1. Line Models:
   (a) Lorentz
   (b) Doppler
   (c) Lorentz-Doppler (Voigt)

2. Narrow Band Models:
   (a) Elsasser
   (b) Statistical
   (c) Random-Elsasser
   (d) Quasi-Random

3. Wide Band Models
   (a) Box or Coffin
   (b) Modified box
   (c) Exponential
   (d) Axial

The relative importance and range of applicability of these models are discussed in Ref. 41. In the moderate temperature range (500-5000K), use of the wide band models and correlations provide sufficient accuracies. These models render significant computational efficiency over the line by line or narrow band models.

The expression for the total band absorptance is given as

$$A(y) = \int_{\Delta\nu} [1-e^{-\int_0^r \kappa_\nu(\xi)d\xi}]d\nu \qquad (3.6a)$$

Differentiation of Eq. (3.6a) gives

$$A'(r) = \int_{\Delta\nu} \kappa_\nu \, e^{-\int_0^r \kappa_\nu(\xi)\, d\xi} \, d\nu \tag{3.6b}$$

$$A''(r) = \int_{\Delta\nu} \kappa_\nu^2 \, e^{-\int_0^r \kappa_\nu(\xi)\, d\xi} \, d\nu \tag{3.6c}$$

These relations are used to obtain expressions for the total radiative flux.

The radiative flux term usually involves multiple integrals even for the simple geometries. As a result, numerical calculations for energy transfer becomes very time consuming. Therefore, it is desirable to replace the relation for the total band absorptance as given by Eq. (3.6a) with a continuous correlation [8, 9, 42]. Several correlations are available in the literature for the wide band absorptance. The first correlation to satisfy the linear, square-root and logrithmic limits of the wide band absorptance was proposed by Edward and Menard [43]. The most widely used correlation is the Tien and Lowder continuous correlation, and this is given by [42]

$$\tilde{A} = \ell n \left[uf(\beta) \left(\frac{u+2}{u+2f(\beta)} \right) + 1. \right] \tag{3.7}$$

$$f(\beta) = 2.94 \left[1-\exp(-2.6\beta) \right]$$

$$\beta = B^2 P_e$$

The form of $f(\beta)$ was chosen to give agreement with the correlation of Edward and Menardo. The Tien and Lowder correlation is employed in this study for the nongray gas formulation.

3.2 Radiative Flux Equations

The equations of radiative transport are expressed generally in integro-differential form; the integration involves both the frequency spectrum and physical coordinates. To overcome the complexity of the radiative transport equations, a tangent slab approximation was employed in [44, 45]. This approximation treats the gas layer as a one-dimensional slab in evaluation of the radiative flux. The multi-dimensional equations of radiative heat transfer are formulated for an arbitrary geometry, and then an approximate method is used to present the formulation for gray and nongray gases.

3.2.1 Basic Formulation

The radiative transport equations in the present study are obtained only for an absorbing-emitting medium contained within solid walls of arbitrary configuration as shown in Fig. 3.1. The general formulation of radiative transfer for the gas under the condition of local thermodynamic equilibrium is given by [12].

$$I_\nu(P) = I_\nu(P_W)\, e^{-\int_0^{r_W} \kappa_\nu(\xi)\, d\xi} + \int_0^{r_W} \kappa_\nu(P')\, I_{b\nu}(P')\, e^{-\int_0^{r'} \kappa_\nu(\xi)\, d\xi}\, dr' \tag{3.8}$$

The first term on the right hand side represents the contribution from the wall to the intensity at P, and the second term, the contribution from the intervening gases between P and P_W. The origin of the coordinate system in Eq. (3.8) is chosen at the point P.

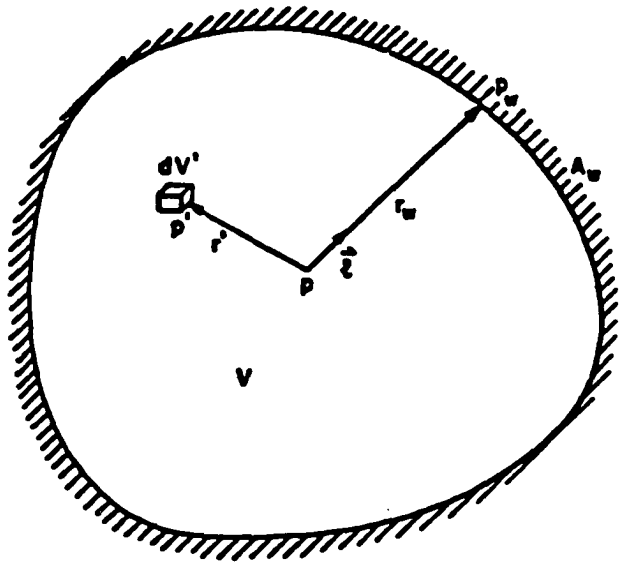

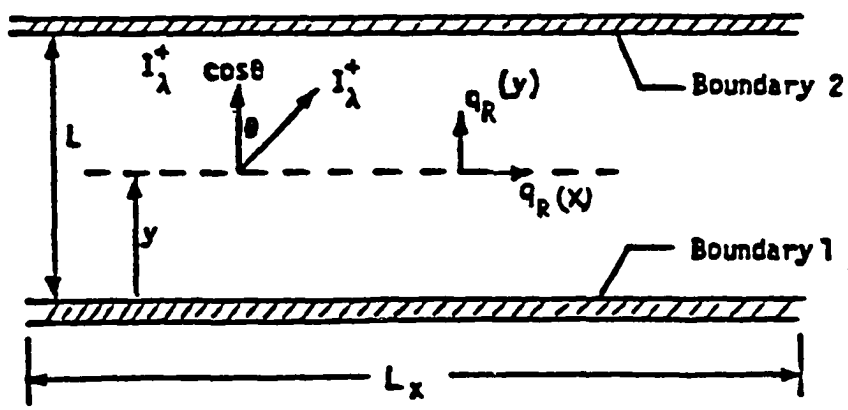

Fig. 3.2 Plane radiating layer between parallel boundaries.

The radiative flux at the point P in the direction of $\vec{\ell}$ is

$$\vec{q}_R = \int_{4\pi} \int_0^{\infty} I_\nu \, \vec{\ell} \, d\nu \, d\Omega \tag{3.9}$$

Substituting Eq. (3.8) into Eq. (3.9), the radiative flux is expressed as

$$\vec{q}_R = \int_{4\pi} \int_0^{\infty} I_\nu(P_w) \, e^{-\int_0^{r_w} \kappa_\nu(\xi) \, d\xi} \, \vec{\ell} \, d\nu \, d\Omega$$

$$+ \int_{4\pi} \int_0^{\infty} \int_0^{r_w} \kappa_\nu(P') \, I_{b\nu}(P') \, e^{-\int_0^{r'} \kappa_\nu(\xi) \, d\xi} \, \vec{\ell} \, dr' \, d\nu \, d\Omega \tag{3.10}$$

The divergence of the radiative flux is formulated as

$$\nabla \cdot \vec{q}_R = \int_{4\pi} \int_0^{\infty} \vec{\ell} \cdot \nabla I_\nu \, d\nu \, d\Omega \tag{3.11a}$$

A beam of intensity $I_\nu(r, \Omega)$ traveling in the $\vec{\ell}$ direction satisfies the equation of radiative transfer

$$\vec{\ell} \cdot \nabla I_\nu = \gamma_\nu I_\nu + \kappa_\nu I_{b\nu} - \beta_\nu I_\nu \tag{3.11b}$$

where γ_ν is the scattering coefficients and $\beta_\nu = \gamma_\nu + \kappa_\nu$ is referred to as the extinction coefficient. For negligible scattering ($\gamma_\nu = 0$), Eq. (3.11b) reduces to

$$\vec{\ell} \cdot \nabla I_\nu = \kappa_\nu (I_{b\nu} - I_\nu) \tag{3.11c}$$

By combining Eqs. (3.11a) and (3.11c), one obtains

$$\nabla \cdot \vec{q}_R = \int_{4\pi} \int_0^\infty \kappa_\nu \, (I_{b\nu} - I_\nu) \, d\nu \, d\Omega \qquad (3.11d)$$

Now substituting Eq. (3.8) into Eq. (3.11b), the divergence of the radiative flux is expressed as

$$\nabla \cdot \vec{q}_R = 4\pi \int_0^\infty \kappa_\nu \, (p) \, I_{b\nu} \, (P) \, d\nu - \int_{4\pi} \int_0^\infty \kappa_\nu \, (P) \, I_\nu \, (P_w) \, e^{-\int_0^{r_w} \kappa_\nu(\xi) \, d\xi}$$

$$- \int_{4\pi} \int_0^\infty \int_0^{r_w} \kappa_\nu \, (P) \, \kappa_\nu \, (P') \, I_{b\nu} \, (P') \, e^{-\int_0^{r'} \kappa_\nu \, (\xi) \, d\xi} \, dr' \, d\nu \, d\Omega \qquad (3.12)$$

Equations (3.10) and (3.12) are used to obtain various approximate forms for the radiative flux and its divergence.

3.2.2 Gray Formulation

In the previous section, it was observed that the radiative flux terms are represented by an integro-differential equation. Solving these equations is extremely time consuming because of the complexity of integration over space and frequency. Therefore, a pesudo-gray model is selected for efficient parametric studies. To express the radiative flux for a gray medium, one may assume that κ_ν is independent of the frequency. This is rarely a physically realistic approximation; but it serves as an initial stepping stone towards nongray analyses. Therefore, Eqs. (3.10) and (3.12) for a gray medium are written as

$$q_R = \int_{4\pi} I(P_w) \, e^{-\int_0^{r_w} \kappa(\xi) \, d\xi} \, d\Omega + \int_{4\pi} \int_0^{r_w} \kappa(P') \, I_b(P') \, e^{-\int_0^{r'} \kappa(\xi) \, d\xi} \, dr' \, d\Omega \qquad (3.13)$$

and

$$\nabla \cdot q_R = 4\pi\, \kappa(P)\, I_b(P) - \int_{4\pi} \kappa(P)\, I(P_w)\, e^{-\int_0^{r_w} \kappa(\xi)\, d\xi}\, d\Omega$$

$$- \int_{4\pi} \int_0^{r_w} \kappa(P)\, \kappa(P')\, I_b(P')\, e^{-\int_0^{r'} \kappa(\xi)\, d\xi}\, dr'\, d\Omega \qquad (3.14)$$

To solve the radiative flux terms for the gray medium, one can transform the above equations into the Cartesian coordinates and then apply any of the standard integration techniques to evaluate the radiative flux terms. It is a lot more convenient and efficient to convert the equations to a set of ordinary differential equations (ODE). For the present case, differentiating Eq. (3.14) by using the Leibnitz rule results in

$$\nabla^2 q_R = 4\kappa(P) \frac{\partial e_b}{\partial r} + \int_{4\pi} \kappa^2(P)\, I(P_w)\, e^{-\int_0^{r_w} \kappa(\xi)\, d\xi}\, d\Omega$$

$$+ \int_{4\pi} \int_0^{r_w} \kappa^w(P)\, \kappa(P')\, I_b(P')\, e^{-\int_0^{r'} \kappa(\xi)\, d\xi}\, dr'\, d\Omega \qquad (3.15)$$

A substitution of Eq. (3.15) into Eq. (3.13) gives a second order nonhomogenious ordinary differential equation as

$$\frac{d^2 q_R}{dr^2} - \kappa^2(P)\, q_R = 4\kappa(P) \frac{de_b}{dr} \qquad (3.16)$$

It should be pointed out that if the tangent slab approximation is employed, then the method of exponential kernal approximation is used to convert the equations to a set of ODE's. The result is of the same form as Eq. (3.16) but the coefficients are different, i.e.,

$$\frac{d^2 q_R}{dr^2} = \frac{9}{4} \kappa^2(P)\, q_R = 3\, \kappa(P) \frac{de_b}{dr} \tag{3.17}$$

Equations (3.16) and (3.17) differ in the coefficients due to the employment of the exponential kernal approximation in the second approach. These equations require two boundary conditions. For nonblack diffuse surfaces, the boundary conditions corresponding to Eq. (3.17) are given as

$$\left(\frac{1}{\varepsilon_1} - \frac{1}{2}\right) \kappa_p\, q_R\,(r)\,\Big|_{r=0} - \frac{1}{3} \frac{dq_R}{dr}\Big|_{r=0} = 0 \tag{3.18a}$$

$$\left(\frac{1}{\varepsilon_2} - \frac{1}{2}\right) \kappa_p\, q_R\,(r)\,\Big|_{r=L} + \frac{1}{3} \frac{dq_R}{dr}\Big|_{r=L} = 0 \tag{3.18b}$$

Detailed derivation of Eqs. (3.17) and (3.18) are given in [44].

3.2.3 Nongray Formulation

For simplicity in notation, it is assumed that the molecular gas has only one band. The following analysis is also applicable to the gas having more than one band. Since the Planck function within a wide band can usually be approximated by its value at the band center, Eqs. (3.10) and (3.12) can be written as

$$\vec{q}_r = \int_{4\pi} \int_{\Delta\nu} I_\nu(P_w) \left[e^{-\int_0^{r_w} \kappa_\nu(\xi)d\xi} - 1\right] \vec{\ell}\, d\nu\, d\Omega + \int_{4\pi} \int_{\Delta\nu} I_\nu(P_w)\, \vec{\ell} \cdot d\nu\, d\Omega$$

$$+ \int_{4\pi} \int_0^{r_w} I_{b\nu c}(P')\, \vec{\ell}\, dr' d\Omega \int_{\Delta\nu} \kappa_\nu(P')\, e^{-\int_0^{r'} \kappa_\nu(\xi)\, d\xi} d\nu \tag{3.19}$$

and

$$\nabla \cdot \vec{q}_R = 4\pi\, I_{b\nu e}(P)\left(\int_{\Delta\nu} \kappa_\nu d\nu\right) - \int_{4\pi} I_{\nu c}(P_w)\left[\int_{\Delta\nu} \kappa_\nu(P_w) e^{-\int_0^{r_w} \kappa_\nu(\xi)\, d\xi} d\nu\right] d\Omega$$

$$+ \int_{4\pi} \int^{r_w} \left[I_{b\nu c}(P')\, \vec{\ell}\, dr' d\Omega \int_{\Delta\nu} \kappa_\nu(P')\, e^{-\int_0^{r'} \kappa_\nu(\xi) d\xi} d\nu\right] dr' d\Omega \quad (3.20)$$

Substituting Eqs. (3.6a-3.6c) into Eqs. (3.19) and (3.20), rearranging, one gets

$$\vec{q}_R = \int_{4\pi} I(P_w)\, \vec{\ell}\, d\Omega - \int_{4\pi} I_{\nu c}(P_w)\, A(r_w)\, \vec{\ell}\, d\Omega$$

$$+ \int_{4\pi} \int_0^{r_w} I_{b\nu c}(P')\, A'(r')\, \vec{\ell}\, dr' d\Omega \quad (3.21)$$

$$\nabla \cdot \vec{q}_R = 4\pi\, I_{b\nu c}(P) A'(0) - \int_{4\pi} I_{\nu c}(P_w) A'(rw) d\Omega + \int_{4\pi} \int_0^{r_w} I_{b\nu c}(P') A''(r') dr' d\Omega \quad (3.22)$$

The first term on the right hand side of Eq. (3.21) represents the radiative flux in the absence of participating medium; the second term gives the portion of the wall radiation which is absorbed by the gas, and the last term indicates the emission from the gas which arrives at point p. Since I_b and A' are independent of Ω, the first term in Eq. (3.22) can be written as

$$4\pi\, I_{b\nu c}(P) A'(0) = \int_{4\pi} I_{b\nu c}(P) A'(0) d\Omega$$

$$= \int_{4\pi} I_{b\nu c}(P) A'(r_w) d\Omega + \int_{4\pi} I_{b\nu c}(P)[A'(0) - A'(r_w)] d\Omega$$

$$= \int_{4\pi} I_{b\nu c}(P) A'(r_w) d\Omega \int_{4\pi} \int_0^{r_w} I_{b\nu c}(P) A''(r') dr' d\Omega \quad (3.23)$$

A substitution of Eq. (3.23) into Eq. (3.22) results in

$$\nabla \cdot \vec{q}_R = \int_{4\pi} [I_{b\nu c}(P) - I_{\nu c}(P_w)] A'(r_w) d\Omega$$

$$- \int_{4\pi} \int_{0}^{r_w} [I_{b\nu c}(P) - I_{b\nu c}(P')] A''(r') dr' d\Omega \qquad (3.24)$$

The first term on the right hand side of Eq. (3.24) represents the net exchange of radiation between the gas element at P and the walls; the second term represents the net exchange between the gas element of P and the other gas elements.

For a nongray planer system with two parallel walls at different temperatures (Fig. 3.2), Eqs. (3.21) and (3.24) reduce to

$$\vec{q}_r = e_1 - e_2 - \int_{-\infty}^{\infty} \int_{-\infty}^{\infty} \int_{0}^{y} e_{\nu c_1}(x', z') A(r_1) \frac{dx' dy' dz'}{\pi r_1^3}$$

$$+ \int_{-\infty}^{\infty} \int_{-\infty}^{\infty} \int_{y}^{L} e_{\nu c_2}(x', z') A(r_2) \frac{dx' dy' dz'}{\pi r_2^3}$$

$$+ \int_{-\infty}^{\infty} \int_{-\infty}^{\infty} \int_{0}^{L} e_{\nu c}(x', y', z') \frac{A'(r')}{\pi r_1^2} dx' dy' dz' \qquad (3.25)$$

and

$$\nabla \cdot \vec{q}_R = [A'(r_1) + A'(r_2)] e_{\nu c}(x, y, z)$$

$$- \int_{-\infty}^{\infty} \int_{-\infty}^{\infty} e_{\nu c_1}(x', z') A'(r_1) \frac{y}{\pi r_1^3} dx' dz'$$

$$- \int_{-\infty}^{\infty} \int_{-\infty}^{\infty} e_{\nu c_2}(x', z')\, A'(r_2)\, \frac{L-y}{\pi r_2^3}\, dx'\, dz'$$

$$- \int_{-\infty}^{\infty} \int_{-\infty}^{\infty} \int_{0}^{L} [e_{\nu c}(x, y, z) - e_{\nu c}(x', y, z')]\, \frac{A''(r')}{\pi r'^2}\, dx'\, dy'\, dz' \qquad (3.26)$$

where

$$r_1 = [(x-x')^2 + (y)^2 + (z-z')^2]^{1/2}$$

$$r_2 = [(x-x')^2 + (y-L)^2 + (z-z')^2]^{1/2}$$

$$r' = [(x-x')^2 + (y-y')^2 + (z-z')^2]^{1/2}$$

The y coordinate is normal to the wall and x and z coordinates are in a plane parallel to the wall. For one-dimensional radiative transfer, Eqs. (3.25) and (3.26) reduce to

$$\vec{q}_R = e_1 - e_2 - e_{\nu c_1} A(y) + e_{\nu c_2} A(L-y)$$

$$+ \int_0^y e_{\nu c}(y')\, A'(y-y')dy' - \int_y^L e_{\nu c}(y')\, A'(y'-y)dy' \qquad (3.27)$$

and

$$\nabla \cdot \vec{q}_R = [e_{\nu c}(y) - e_{\nu c_1}]A'(y) + [e_{\nu c}(y) - e_{\nu c_2}]\, A'(L-y)$$

$$- \int_0^y [e_{\nu c}(y) - e_{\nu c}(y')]A''\,(y-y')dy'$$

$$- \int_y^L [e_{\nu c}(y) - e_{\nu c}(y) - e_{\nu c}(y')]A''\,(y'-y)dy \qquad (3.28)$$

Equations (3.27) and (3.28) can be rearranged and written for a multi-band gaseous system as (see Appendix B)

$$q_R(y) = e_1 - e_2 + \sum_{i=1}^{N} \{\int_0^y F_{1\nu c_i}(y')\, A_i'(y-y')\, dy' - \int_y^L F_{2\nu c_i}(y')\, A_i'(y'-y)dy'\} \tag{3.29}$$

and

$$\nabla \cdot q_R(y) = \sum_{i=1}^{N} \{[F_{1\nu c_i}(y) + F_{2\nu c_i}(y)] \int_{\Delta\nu_i} \kappa_{\nu_i}\, d\nu_i + \int_0^y F_{1\nu c_i}(y')\, A_i''(y-y')\, dy' + \int_0^L F_{2\nu c_i}(y')\, A_i''(y'-y)\, dy' \tag{3.30}$$

where

$$F_{1\nu c}(y) = e_{\nu c}(y) - e_{\nu c_1}$$

and

$$F_{2\nu c}(y) = e_{\nu c}(y) - e_{\nu c_2}$$

The equations resulting from employing the tangent slab approximation and exponential kernal approximation for evaluating the exponetial function are of the same general form as Eqs. (3.29) and (3.30). These equations are derived in detail in Ref. 9 and are expressed here as

$$q_R(y) = e_1 - e_2 + \frac{3}{2}\left\{\int_0^y F_{1\omega c_i}(y')\, A_i'\left[\frac{3}{2}(y-y')\right] dy' - \int_y^L F_{2\omega c_i}(y')\, A_i'\left[\frac{3}{2}(y'-y)\right] d'\right\} \qquad (3.31)$$

and

$$\nabla\cdot q_R(y) = \frac{3}{2}\sum_{i=1}^{n}\left\{\left[F_{1\omega c_i}(y) + F_{2\omega c_i}(y)\right]\int_{\Delta\omega_i}\kappa_{\omega_i}\, d\,\omega_i\right\} + \frac{9}{4}\sum_{i=1}^{n}\left\{\int_0^y F_{1\omega c_i}(y')\, A_i''\left[\frac{3}{2}(y-y')\right]dy' + \int_y^L F_{2\omega c_i}(y')\, A_i''\left[\frac{3}{2}(y'-y)\right]dy'\right\} \qquad (3.32)$$

Equations (3.29-3.32) are in proper form for obtaining the nongray solutions of molecular species. However, in order to be able to use the band model correlations, these equations must be transformed in terms of the correlation quantities. For the temperature range considered, the radiative process is in the optically thin limit [39]. As a result, there is no significant difference between the two approaches. It should be noted here that for nongray gases, the divergence of radiative flux is used as a source term in the energy equation. This is more convenient and also avoids scheme dependency in the computation. The correlation quantities and details of transformations are given in Ref. 20. After the transformation, Eq. (3.32) is written as

$$\frac{dq_R(u)}{du} = \frac{9}{4} \sum_{i=1}^{n} A_{o_i} \{ \int_{o}^{u_i} F_{1\omega_i}(u') \bar{A}_i'' [\frac{3}{2}(u_i - u_i')] du_i'$$

$$+ \int_{u_i}^{u_{c_i}} F_{2\omega_i}(u') \bar{A}_i'' [\frac{3}{2}(u_i' - u_i)] du_i' \}$$

$$+ \frac{3}{2} \sum_{i=1}^{n} A_{o_i} [F_{1\omega_i}(u) + F_{2\omega_i}(u)] \qquad (3.33)$$

Note that $\bar{A}''(u)$ expresses the second derivative of $\bar{A}(u)$ with respect to u and

$$\frac{dq_R}{dy} = \frac{dq_R}{du} \frac{du}{dy} = [PS(T)/A_o] \frac{dq_R}{du}$$

By defining $\frac{u}{u_o} = \frac{y}{L}$ and $\frac{u'}{u_o} = \frac{y'}{L}$, Eq. (3.33) is expressed as

$$dq_R(y)/dy = 9/4 \sum_{i=1}^{n} A_{o_i} u_{o_i}^2/L^2 \{ \int_{o}^{y} F_{1\omega_i}(y') \bar{A}_i'' [\frac{3}{2} \frac{u_{o_i}}{L} (y-y')] dy'$$

$$+ \int_{y}^{L} F_{2\omega_i}(y') \bar{A}_i'' [\frac{3}{2} \frac{u_{o_i}}{L} (y'-y)] dy' \}$$

$$+ \frac{3}{2} \sum_{i=1}^{n} \frac{A_{o_i} u_{o_i}}{L} [F_{1\omega_i}(y') F_{2\omega_i}(y')] \qquad (3.34)$$

It is often desirable and convenient to express the proceeding equation in terms of $\bar{A}'$ rather than $\bar{A}''$. This is accomplished by integrating Eq. (3.34) by parts. The detail of the integration by parts is given in Ref. 9 and the result is given by

$$\frac{dq_R}{dy} = \frac{3}{2} \sum_{i=1}^{n} \frac{A_{o_i} u_{o_i}}{L} \left\{ \int_0^y \frac{de_{\omega_i}(y')}{dy'} \bar{A}'_i \left[\frac{3}{2} \frac{u_{o_i}}{L} (y-y') \right] dy' \right.$$

$$\left. - \int_y^L \frac{de_{\omega_i}(y')}{dy'} \bar{A}'_i \left[\frac{3}{2} \frac{u_{o_i}}{L} (y'-y) \right] dy' \right\} \qquad (3.35)$$

Equation (3.35) and the Tien and Lowder correlation given by Eq. (3.7) can be used to evaluate the radiative flux.

3.2.4 Optically Thin Formulation

In the optically thin limit, the fluid does not absorb any of its own emitted radiation; however, it does absorb radiation emitted from the boundaries [6-9]. In general, the optical thickness of an absorbing-emitting system is defined as

$$\tau_{o\omega} = \int_0^L \kappa_\omega \, dy \qquad (3.36)$$

If it is assumed that κ_ω is independent of the temperature, then Eq. (3.36) is expressed as

$$\tau_{o\omega} = \kappa_\omega L \qquad (3.37)$$

A radiating system is considered to be in the optically thin limit when $\tau_{o\omega} << 1$.

In the optically thin limit, the expressions for the radiative flux and its divergence can be obtained from the general expressions by following the procedure outlined in [6]. For the gray gas approximation and black-bounding surfaces, Eq. (3.14) is expressed for one-dimensional optically thin radiation as

$$\frac{dq_R}{dy} = 2\,\kappa_\omega\,[2\,e_{b_\omega}(y) - e_{b_1} - e_{b_2}] \tag{3.38}$$

For the pseudo-gray gas model, κ_ω is replaced by κ_p through use of Eqs. (3.1) - (3.5).

For the case of nongray gas formulation, $\bar{A}(u) = u$ and $\bar{A}'(u) = 1$ in the optically thin limit [6, 7]. Consequently, Eq. (3.35) reduces in this limit to

$$\frac{dq_R}{dy} = \frac{3}{2}\sum_{i=1}^{n}\frac{A_{o_i}\,u_{o_i}}{L}\,[2\,e_{\omega_i}(y) - e_{1_{\omega_i}} - e_{2_{\omega_i}}] \tag{3.39}$$

It should be pointed out that it is considerably more efficient to solve numerically the system of governing equations for the case of optically thin radiation than for the general case. In a preliminary study, the optical thickness of the present physical problem were calculated. It was found that the optical thickness varied between 0.003 to 0.4 in the temperature range of 1,000 to 5,000 K and pressure between one to three atmospheres.

Chapter 4

METHOD OF SOLUTION

The grid generation technique and solution procedures for the governing equations using the unsplit MacCormack [46] technique and modified Runge-Kutta time stepping scheme of Jameson [32] are briefly discussed in this section.

4.1 Grid Generation

Grids are generated using an algebraic grid generation technique developed by Smith and Weigel [47]. From the computational point of view, it is desirable to have a uniform rectangular grid enclosed in a cube, where the exterior of the cube represents the physical boundaries. To have such grids, the body-fitted coordinate system is transformed linearly from the physical domain (x, y) to the computational domain (ξ, η) as follows:

$$\begin{aligned} X_1 &= X(\xi,0) \\ y_1 &= Y(\xi,0) \end{aligned} \qquad \text{Lower Boundary} \qquad (4.1a)$$

$$\begin{aligned} X_2 &= X(\xi,1) \\ y_2 &= Y(\xi,1) \end{aligned} \qquad \text{Upper Boundary} \qquad (4.1b)$$

$$\begin{aligned} X &= X(\xi,1)\,\eta + X(\xi,0)\,(1-\eta) \\ y &= Y(\xi,1)\,\eta + Y(\xi,0)\,(1-\eta) \end{aligned} \qquad \text{Between the Boundaries} \qquad (4.1c)$$

where

$$0 < \xi < 1 \quad ; 0 < \eta < 1$$

The grid should be concentrated in the regions of high gradients to accurately predict the solution. Therefore, more grid points are required near the solid boundaries. The concentration of the grid in the η-direction can be accomplished by

$$\bar{\eta} = \frac{(\beta_y+1) - (\beta_y-1)\exp[-C(\eta-1+\alpha)/(1-\alpha)]}{(2\alpha+1)\{1+\exp[1C(\eta-1+\alpha)/(1-\alpha)]\}} \tag{4.2}$$

where

$$C = \ell n \left(\frac{\beta_y+1}{\beta_y-1}\right)$$

If α is equal to zero ($\alpha=0$), the compression takes place only near the lower wall ($\eta=0$), and if α is set equal to one half ($\alpha=1/2$), the compression takes place near both walls. The term β_y has a value between one and two, and as it gets closer to one, the grid becomes more concentrated near the walls. Employing this concentration, Eq. (4.1e) is written in terms of $\bar{\eta}$ as

$$X = X(\xi,1)\,\bar{\eta} + X(\xi,0)\,(1-\bar{\eta})$$

$$y = Y(\xi,1)\,\bar{\eta} + Y(\xi,0)\,(1-\bar{\eta}) \tag{4.3}$$

where

$$0 < \bar{\eta} < 1$$

It should be noticed that the grid is concentrated in the normal direction to capture the boundary layer and kept uniform in the flow direction.

4.2 Solution of the Govening Equations

4.2.1 Modified MacCormack's Finite-Difference Scheme

The governing equations, Eqs. (2.1), are expressed in the computational domain as

$$\frac{\partial \hat{U}}{\partial t} + \frac{\partial \hat{F}}{\partial \xi} + \frac{\partial \hat{G}}{\partial \eta} + \hat{H} = 0 \tag{4.4}$$

where

$$\hat{U} = UJ$$

$$\hat{F} = Fy_{\eta} - Gx_{\eta}$$

$$\hat{G} = Gx_{\xi} - Fy_{\xi}$$

$$\hat{H} = HJ$$

$$J = x_{\xi}\, y_{\eta} - y_{\xi}\, x_{\eta}$$

Equation (4.4) is discretized temporally and written as

$$\hat{U}^{n+1} = \hat{U}^{n} - \Delta t \left[\frac{\partial \hat{F}^{n}}{\partial \xi} + \frac{\partial \hat{G}^{n}}{\partial \eta} + \hat{H}^{n+1}\right] \tag{4.5}$$

The source term $\hat{H}^{n+1}$ must next be linearized. It is expanded in a Taylor series in time to give

$$\hat{H}^{n+1} = \hat{H}^{n} + \Delta t \frac{\partial \hat{H}}{\partial t} + O\,(\Delta t)^2 \tag{4.6}$$

or

$$\hat{H}^{n+1} = \hat{H}^{n} + \Delta t \frac{\partial H}{\partial \hat{U}} \left(\frac{\hat{U}^{n+1} - \hat{U}^{n}}{\Delta t}\right) \tag{4.7}$$

A substitution of Eq. (4.7) into Eq. (4.5) gives the temporally discrete equation in delta form as

$$[I + \Delta t \frac{\partial \hat{H}}{\partial \hat{U}}] \Delta \hat{U}^{n+1} = -\Delta t [\frac{\partial \hat{F}}{\partial \xi} + \frac{\partial \hat{G}}{\partial \eta} + \hat{H}]^n \tag{4.8}$$

where $\hat{U}^{n+1} - \hat{U}^n$ is expressed as $\Delta \hat{U}^{n+1}$, $\frac{\partial \hat{H}}{\partial \hat{U}}$ is the Jacobian matrix of H and I is the identity matrix. The components of the Jacobian matrix are given in Appendix C.

Once the temporal discretization used to construct Eq. (4.8) has been performed, the resulting system is spatially differenced using the unsplit MacCormack predictor-corrector scheme. This results in a spatially and temporally discrete, simultaneous system of equations at each grid point. Each simultaneous system is solved using the Householder technique [48, 49] in combination with the MacCormack technique, which is then used to advance the equations in time. The modified MacCormack scheme then becomes

$$[I + \Delta t (\frac{\partial \hat{H}}{\partial \hat{U}})^n_{ij}] \Delta \hat{U}^{\overline{n+1}}_{ij} = - \Delta t [\frac{\partial \hat{F}}{\partial \xi} + \frac{\partial \hat{G}}{\partial \eta} + \hat{H}]^n_{ij} \tag{4.9a}$$

$$\hat{U}^{\overline{n+1}}_{ij} = \hat{U}^n_{ij} + \Delta \hat{U}^{\overline{n+1}}_{ij} \tag{4.9b}$$

$$[I + \Delta t (\frac{\partial \hat{H}}{\partial \hat{U}})^n_{ij}] \Delta \hat{U}^{n+1}_{ij} = - \Delta t [\frac{\partial \hat{F}}{\partial \xi} + \frac{\partial \hat{G}}{\partial \eta} + \hat{H}]^{\overline{n+1}}_{ij} \tag{4.10a}$$

$$\hat{U}^{n+1}_{ij} = \hat{U}^n_{ij} + 0.5 [\Delta \hat{U}^{n+1}_{ij} + \Delta \hat{U}^{\overline{n+1}}_{ij}] \tag{4.10b}$$

Equations (4.9) and (4.10) are used to advance the solution from time n to n+1, and iteration process is continued until a desired integration time has been reached.

4.2.2 Modified Runge-Kutta Finite-Volume Technique

In 1981, Jameson, Schmidt and Turkel [33] proposed an explicit finite volume technique using Runge-Kutta time stepping scheme for the solution of unsteady Euler equations. The scheme is a modified version of the classical four stage Runge-Kutta technique. The method is fourth-order accurate in time for linear equations and second-order accurate for nonlinear equations. The scheme is second-order accurate in space for both linear and nonlinear problems, provided the grid is sufficiently smooth. This scheme was extended by Swanson and Turkel [35] to solve the thin layer Navier-Stokes equations for transonic flow over the airfoil. In the present work, this scheme is being extended to solve supersonic chemically reacting and radiating viscous flows. The governing equation, Eq. (2.9), in integral form for a region Ω with boundary $\partial\Omega$ is rewritten here for the convenience as

$$\frac{\partial}{\partial t}\iint_{\Omega} U\, dxdy + \oint_{\partial\Omega} (F\, dy - G\, dx) + \iint_{\Omega} H\, dxdy = 0 \qquad (4.11)$$

The discretization procedure follows the method of lines in decoupling the approximation of the spatial and temporal terms. The computational domain is divided into quadrilateral cells (Fig. 4.1), and Eq. (4.11) is applied to each cell separately to obtain a system of ordinary differential equations. The resulting equations are solved by the finite volume scheme of Jameson.

Applying Eq. (4.11) to an arbitrary cell, ABCD, and approximating the integrals by the midpoint rule, one obtains

$$\frac{d}{dt}(A_{ij}\, U_{ij}) + L\, U_{ij} + A_{ij}\, H_{ij} = 0 \qquad (4.12)$$

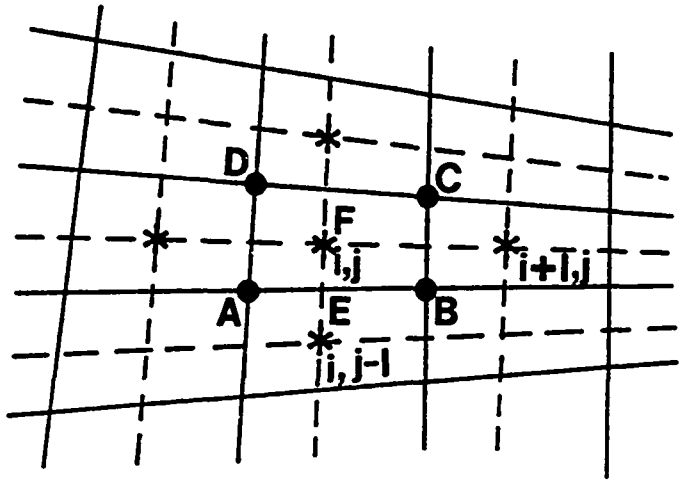

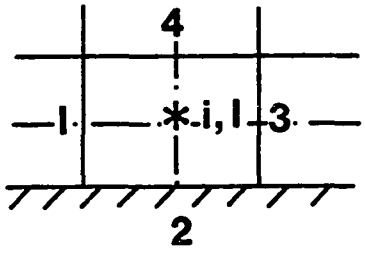

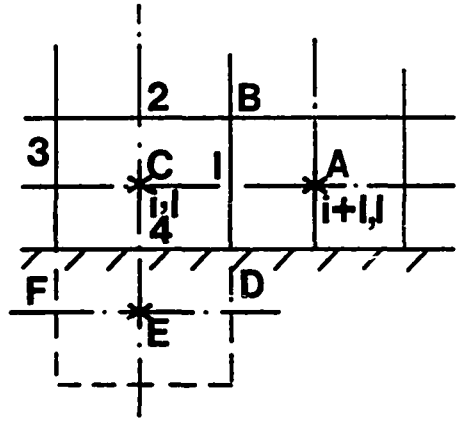

Fig. 4.2 Boundary cells.

Equation (4.12), with the inclusion of artificial viscosity, is written as

$$\frac{d}{dt}(A_{ij}\,U_{ij}) + L\,U_{ij} - D\,U_{ij} + A_{ij}\,H_{ij} = 0 \qquad (4.13)$$

where L is the spatial discretization operator, and

$$L\,U_{ij} = FLX_{AB} + FLX_{BC} + FLX_{CD} + FLX_{DA} \qquad (4.14)$$

The components of U_{ij} are now cell averaged quantities; A_{ij} is the cell area of ABCD. The vector FLX represents the fluxes through the cell sides. For example, FLX_{AB} is written as follows

$$FLX_{AB} = F_{AB}\,\Delta Y_{AB} - G_{AB}\,\Delta X_{AB} \qquad (4.15)$$

where F_{AB} and G_{AB} are viscous and inviscid fluxes through the side AB and

$$\Delta Y_{AB} = Y_B - Y_A;\ \Delta X_{AB} = X_B - X_A$$

Inviscid fluxes are evaluated from two adjacent cells as

$$(F_{AB})_{inv} = (F_{ij} + F_{ij-1})_{inv}/2 \qquad (4.16)$$

To evaluate the viscous fluxes on the cell sides, one must evaluate u_x and u_y. These components are evaluated from Green's theorem as follows:

$$(u_x)_{AB} = (u_x)_{i,j-1/2} = \frac{1}{A_{i,j-1/2}} \iint_{\Omega} u_x\,dxdy = \frac{1}{A_{i,j-1/2}} \oint_{\partial\Omega} u\,dy \qquad (4.17a)$$

$$(u_y)_{AB} = (u_y)_{i,j-1/2} = \frac{1}{A_{i,j-1/2}} \iint_{\Omega} u_y\,dxdy = -\frac{1}{A_{i,j-1/2}} \oint_{\partial\Omega} u\,dx \qquad (4.17b)$$

In discrete form, u_x for the cell side AB in Fig. 4.1 is written as

$$(u_x)_{AB} = \frac{1}{A_{i,j-1/2}} (u_E \Delta Y_E + U_B \Delta Y_B + u_F \Delta Y_F + u_A \Delta Y_A) \qquad (4.17c)$$

Velocities at the cell corners are evaluated from the four adjacent cells, and $A_{i,j-1/2}$ is evaluated as

$$A_{i,j-1/2} = \frac{1}{2} (A_{i,j} + A_{i,j-1})$$

4.2.2.1 Boundary Conditions - So far, only the interior cells have been considered. The implementations of the boundary cells are consider in this section. These include supersonic inflow and outflow, and slip and nonslip wall boundary conditions. To determine the inflow quantities, the flux vectors will be evaluated based on the free stream conditions. For outflow conditions, the quantities are extrapolated from the interior points. For the inviscid flow at the solid wall, a zero wall flux condition is implied, that is

$$\vec{V}_n \Delta S = 0 \qquad (4.18)$$

where V_n is the normal wall velocity and ΔS is the wall cell surface area (Fig. 4.2a). Equation (4.18) is written in Cartesian coordinates as

$$V_n \Delta S = u \Delta y - v \Delta x$$

Thus for inviscid flows, the net fluxes through face 2 (Fig. 4.2a) are

$$\int (F\, dy - G\, dx) = 0 \qquad \text{Continuity Eq.}$$

$$\int (F\, dy - G\, dx) = (P \Delta y) \qquad \text{X-mom. Eq.}$$

$$\int(F\,dy - G\,dx) = (-P\Delta x) \qquad \text{Y-mom. Eq.}$$

$$\int(F\,dy - G\,dx) = 0 \qquad \text{Energy Eq.} \tag{4.19}$$

Pressure at the wall is evaluated by

$$P_w = P_{i,1} - \frac{\partial P}{\partial y}\Delta y + 0\,(\Delta y)^2$$

The pressure gradient is calculated using the three point differencing method. For viscous flow, pressure gradient is set to zero (boundary layer assumptions).

Finally, the no slip boundary conditions for viscous flows must be considered. The wall fluxes are divided into inviscid and viscous parts; the inviscid parts are evaluated from Eqs. (4.19). For viscous flow, the velocity component tangent to the wall must be zero. As the result of this constraint, the viscous flux vector is nonzero. For example, $\frac{\partial u}{\partial y}$ and $\frac{\partial T}{\partial y}$ can be computed on face 1 in Fig. 4.2b as

$$\frac{\partial u}{\partial y} = -\frac{u_A\,\Delta X_A + u_B\,\Delta X_B + u_C\,\Delta X_C}{A_{ABCD}} \tag{4.20a}$$

$$\frac{\partial T}{\partial y} = -\frac{T_A\,\Delta X_A + T_B\,\Delta X_B + T_C\,\Delta X_C + T_D\,\Delta X_D}{A_{ABCD}}$$

$$T_D = 0.5\,(T_{i,1} + T_{i+1,1}) \qquad \text{for an adiabatic wall}$$

For face 4, the gradient of T and u are evaluated from the ghost cell CDEF.

$$\frac{\partial T}{\partial y} = \frac{T_C\,\Delta X_C + T_F\,\Delta X_F + T_E\,\Delta X_E + T_D\,\Delta X_D}{A_{i,1}} \qquad (4.20b)$$

$T_D = T_F = T_E = T_{i,1}$ for an adiabatic wall

$T_D = T_F = T_w$ for constant wall temperature

$T_E = T_{i,1} + 2\,(T_w - T_{i,1})$

and

$$\frac{\partial u}{\partial y} = -\frac{u_E\,\Delta X_E + u_C\,\Delta X_C}{A_{i,1}}\ ;\ u_E = -\,u_C$$

Note that ΔX is direction dependent ($\Delta X_C = -\,\Delta X_E$).

4.2.2.2 Artificial Viscosity - The finite volume scheme (Eq. (4.12)), unlike the MacCormack scheme, is not inherently dissipative and, therefore, it does allow undamped oscillations with an alternate sign at odd and even grid points. To prevent large oscillations caused by a discontinuity, some kind of artificial damping must be added to the scheme. The original damping proposed by Jameson et al. [33] is a blend of second- and fourth-order differencing. The basic idea is to add the fourth-order dissipative terms throughout the domain to provide a base level of dissipation sufficient to prevent nonlinear instability, but not enough to prevent oscillations in the neighorhood of shock waves. For the linear problem with central differencing schemes, the neighboring points decouple. This odd-even decoupling prevents the possibility of driving the residual to machine zero. For the nonlinear equation, the values are evaluated at the cell sides before evaluating the fluxes. This nonlinearity couples all the neighboring points together. However, this coupling is weak and convergence to a steady state can be slow [33]. In order to capture the shock waves, additional

second-order dissipative terms are added locally by a sensor designated to detect the shock waves. In recent years, Jameson has modified the original damping to lead to a scheme which will behave locally like a TVD scheme [50, 51]. Both dampings were tested in this study by solving the two-dimensional Euler equations. The TVD damping prevented the pre- and post-shock oscillations which were observed when the original damping was used. The results of the two dampings are compared in the next chapter. The original dissipation and the TVD dissipation schemes modifications are outlined here. To preserve the conservation form, the dissipative terms are generated by dissipative fluxes. The damping term in Eq. (4.13) is calculated from

$$D_{i,j}(U) = d_{i+1/2,j} - d_{i-1/2,j} + d_{i,j+1/2} - d_{i,j-1/2} \tag{4.21}$$

where the dissipative flux $d_{i+1/2,j}$ is defined by

$$\begin{aligned} d_{i+1/2,j} &= \varepsilon^{(2)}_{i+1/2,j} R_{i+1/2,j} (U_{i+1,j} - U_{i,j}) \\ &\quad - \varepsilon^{(4)}_{i+1/2,j} R_{i+1/2,j} (U_{i+2,j} - 3U_{i+1,j} + 3U_{i,j} - U_{i-1,j}) \end{aligned} \tag{4.22}$$

Here, $\varepsilon^{(2)}_{i+1/2}$ is an $\varepsilon^{(4)}_{i+1/2,j}$ are adaptive coefficients and $R_{i+1/2,j}$ is a coefficient chosen to give the dissipative terms the proper scale. An appropriate scale is [50]

$$R_{i+1/2,j} = \frac{1}{2}\left(\frac{A_{i+1,j}}{\Delta t_{i+1,j}} + \frac{A_{i,j}}{\Delta t_{i,j}}\right) \tag{4.23}$$

An effective sensor of the presence of a shock wave can be constructed by taking the second difference of the pressure. Define

$$\nu_{ij} = \left| \frac{P_{i+1,j} - 2P_{i,j} + P_{i-1,j}}{P_{i+1,j} + 2P_{i,j} + P_{i-1,j}} \right| \tag{4.24}$$

and set

$$\bar{\nu}_{i+1/2,j} = \max(\nu_{i+2,j}, \nu_{i+1,j}, \nu_{i,j}, \nu_{i-1,j})$$

The coefficients $\varepsilon^{(2)}_{i+1/2,j}$ and $\varepsilon^{4}_{i+1/2,j}$ in the original form were written as

$$\varepsilon^{(2)}_{i+1/2,j} = K^{(2)} \bar{\nu}_{i+1/2,j} \tag{4.25a}$$

and

$$\varepsilon^{(4)}_{i+1/2,j} = \max[0., (K^{(4)} - \varepsilon^{(2)}_{i+1/2,j})] \tag{4.25b}$$

where

$$K^{(2)} = 0.25 \quad \text{and} \quad K^{(4)} = 1/256$$

The modified coefficients $\varepsilon^{(2)}$ and $\varepsilon^{(4)}$ that have approximately the TVD property are written as

$$\varepsilon^{(2)}_{i+1/2,j} = \min\left(\frac{1}{2}, K^{(2)} \bar{\nu}_{i+1/2,j}\right) \tag{4.26a}$$

and

$$\varepsilon^{(4)}_{i+1/2,j} = \max(0., K^{(4)} - \alpha \bar{\nu}_{i+1/2,j}) \tag{4.26b}$$

where

$$K^{(2)} = 1, \quad K^{(4)} = 1/64, \quad \text{and } \alpha = 2$$

In a smooth region, $\varepsilon^{(2)}$ is proportional to the square of the mesh width and $\varepsilon^{(4)}$ is of order one, therefore, $d_{i+1/2,j}$ in Eq. (4.22) is of order three. In the shock region, $\varepsilon^{(4)}$ is zero, and, therefore, the fourth-order damping is cut off to prevent oscillation, and $\varepsilon^{(2)}$ is of order one, so that the scheme behaves locally like a first-order scheme. However, this does not effect the global second order accuracy of the finite volume scheme [35].

4.2.2.3 Time-Stepping Scheme - Equation (4.13) is discretized temporally and written as

$$A_{ij}\left(\frac{U_{ij}^{n+1} - U_{ij}^{n}}{\Delta t}\right) + L\,U_{ij} - D\,U_{ij} + A_{ij}\,H_{ij}^{n+1} = 0 \qquad (4.27)$$

Substituting Eq. (4.7) for the source term, Eq. (4.27) is written in delta form as

$$\left[I + \Delta t\left(\frac{\partial H}{\partial U}\right)^{n}\right]\Delta U^{n+1} = -\frac{\Delta t}{A_{ij}}\left[L\,U_{ij}^{n} - D\,U_{ij}^{n} + A_{ij}\,H_{ij}^{n}\right] \qquad (4.28)$$

To advance Eq. (4.28) in time, the modified four-stage R-K technique in combination with the householder technique [46, 47] is employed. At time level n, the scheme is written as

$$U^{(0)} = U^{(n)}$$

$$\left[I + \Delta t\left(\frac{\partial H}{\partial U}\right)\right]\Delta U^{k} = -\alpha_k \frac{\Delta t}{A_{ij}}\left[L\,U^{K-1} - DU(0) + A_{ij}\,H_{ij}^{n}\right]$$

$$U^{K} = U^{0} + \Delta U^{K}$$

$$K = 1,4 \quad \alpha_1 = 1/4,\ \alpha_2 = 1/3,\ \alpha_3 = 1/2,\ \alpha_4 = 1$$

$$U^{(n+1)} = U^{(4)}$$

For efficiency purposes, the natural and artificial viscosities are evaluated at the first stage and frozen for the remaining stages.

For time accurate solution, the computational time step, Δt, must satisfy the smallest time scales of the fluid and chemistry, i.e., $\Delta t = \min\ (\Delta t_f, \Delta t_{ch})$. If the steady state solution is sought (as in this study), it is possible to speed up the convergence by using a

larger time scale due to the so-called preconditioning matrix (left hand side bracket in Eqs. (4.8) and (4.28)), the purpose of which is to normalize the various time scales so that they are of the same order [28]. To further speed up the convergence, the solution is advanced in time with a time step dictated by the local stability limit. In the present work, the local Δt is based on the Courant-Friedrichs-Lewy (CFL) stability limit. Local time stepping allows faster signal propagation, and thus faster convergence.

The radiative flux term is evaluated for both gray and nongray gaseous systems. In the nongray gas formulation, the divergence of the radiative flux is evaluated using a central differencing scheme and is treated as radiative source term in the energy equation. Since the radiative flux term is in integro-differential form, unlike the other flux terms which are only in a differential form, it is uncoupled and treated separately. In the gray gas formulation, Eqs. (3.17) and (3.18) are discretized by central differencing, forming a tridiagonal matrix (see Appendix D). This tridiagonal matrix can be solved efficiently by the Thomas algorithm. The radiative fluxes and chemistry rates are evaluated at the first stage and frozen in the remaining stages.

Chapter 5

RESULTS AND DISCUSSION

Based on the theory and the computational procedures described previously, two algorithms were developed to solve the two-dimensional Navier-Stokes equations for chemically reacting and radiating supersonic flows. The performances of two damping schemes are compared by solving the Euler equations for supersonic flow through a channel with a ten degree compression-expansion ramp (Fig 5.1). Then, the Navier-Stokes equations are solved by a finite difference and a finite volume scheme, and results are compared with another computational method. Finally, the extent of the radiative heat transfer in supersonic chemically reacting flows is investigated.

For simplicity in the rest of this discussion, the original damping is referred to as Damp1 and the modified TVD version as Damp2. In the numerical experiment with Damp1, it was found that the tangential component of the second order dissipation ($\varepsilon^{(2)}$) becomes large at the inlet region and this causes the flow to separate near the boundary. The excessive damping is because of the pressure jump caused by the leading edge shock. This behavior was also observed by Turkel [34] at the leading and trailing edges of the airfoil. He suggested multiplying the viscosity by $(M/M_\infty)^4$. Chen et al. [52] suggested multiplying $\varepsilon^{(2)}$ by a linear factor which is zero near the boundary and one in the farfield. The coefficients $K^{(2)}$ and $K^{(4)}$ must be readjusted each time

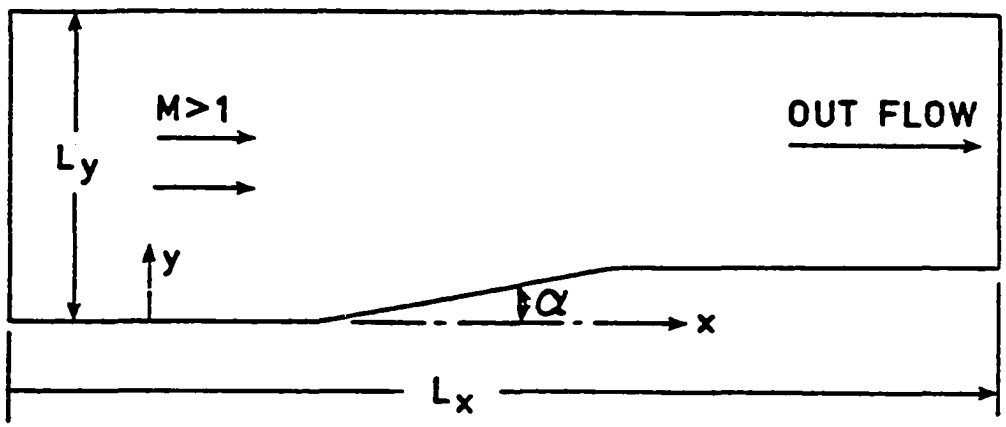

Fig. 5.1 Flow in a channel with compression-expansion corners.

by changing the free stream conditions or the grid size. The above problems make Damping1 less desirable. On the other hand, Damp2 leads to a scheme which will behave locally like TVD scheme as long as $\epsilon^{(2)}$ in Eq. (4.26a) is equal to 1/2 in the neighborhood of a shock wave.

5.1 Non-Reacting Flows

The non-reacting flow equations are solved first for inviscid and then for viscous flows. The inviscid flows are considered for comparing the performance and accuracies of two damping schemes (Damp1 and TVD Damp) in the finite volume scheme. The results are compared with calculated results of the inviscid flow by the finite difference scheme of MacCormack. In the remainder of this chapter, wherever finite difference and finite volume schemes are referred, the reference is to the MacCormack and Jameson schemes, respectively.

The Euler equations were solved for ideal gas flowing at $M_\infty = 5$, $T_\infty = 293$ K, and $P_\infty = 1$ atm in the channel with a compression-expansion ramp (Fig. 5.1). A 51x51 grid with uniform spacing in both the flow and normal direction was used to solve the flow. Figures 5.2-5.4 show the results for the temperature, pressure, and density variations, as a function of x for three locations across the channel (lower boundary, center of the channel and upper boundary). The results are obtained by employing the finite volume scheme with Damp1. Similar results are illustrated in Figs. 5.5-5.7 when Damp2 is employed in the finite volume scheme. Comparing the results of Figs. 5.2-5.4 with the results of Figs. 5.5-5.7, it is seen that pre- and post-shock oscillations are removed by employing Damp2. As mentioned previously, employing Damp2, the scheme behaves locally like a TVD scheme as long as

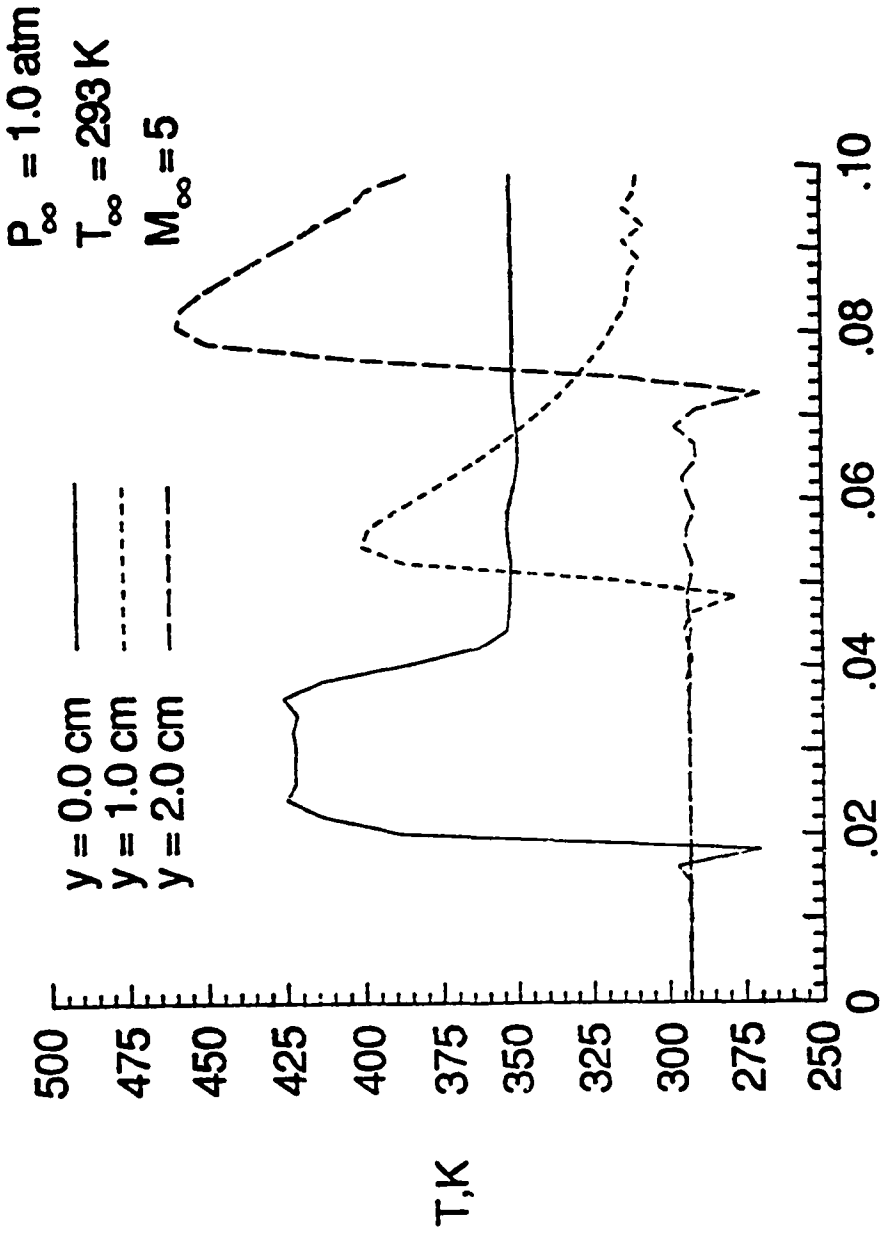

Fig. 5.2 Temperature variation with x for inviscid flow by finite volume scheme.

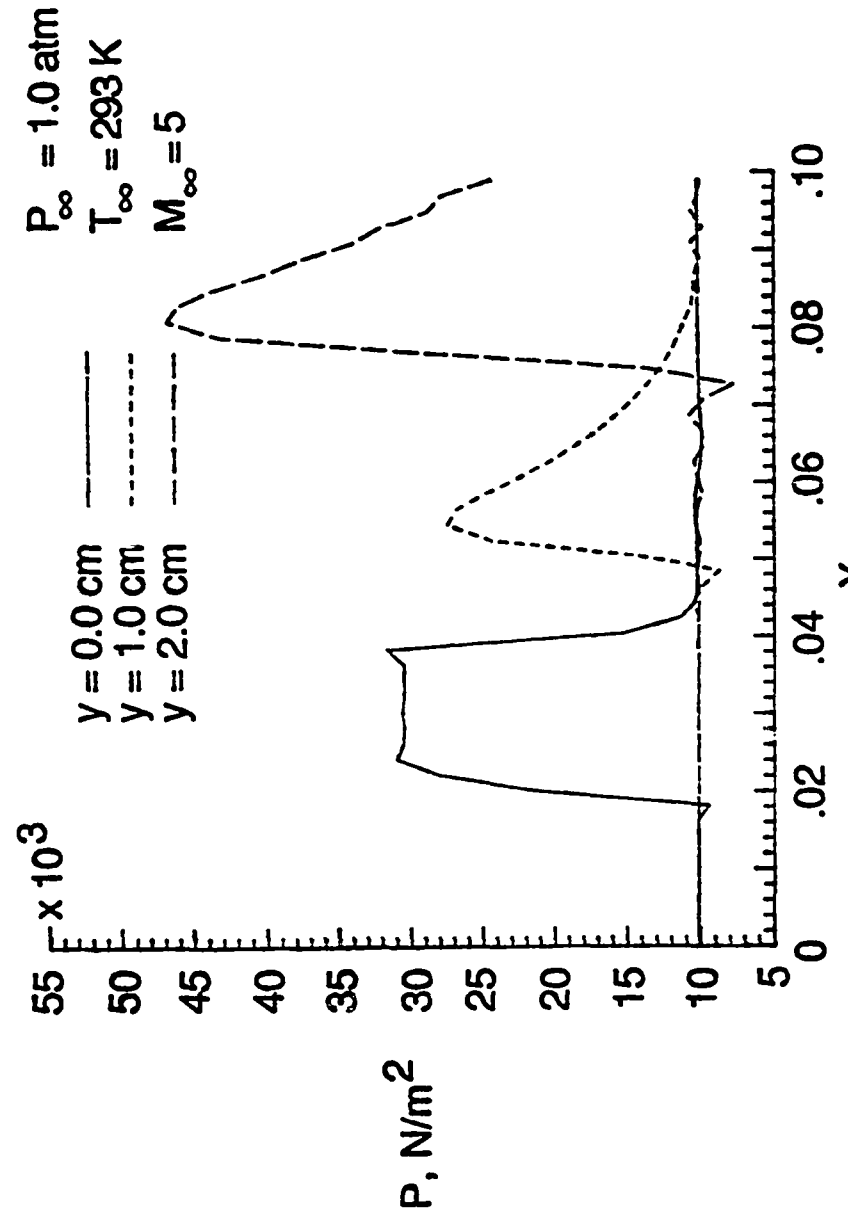

Fig. 5.3 Pressure variation with x for inviscid flow by finite volume scheme.

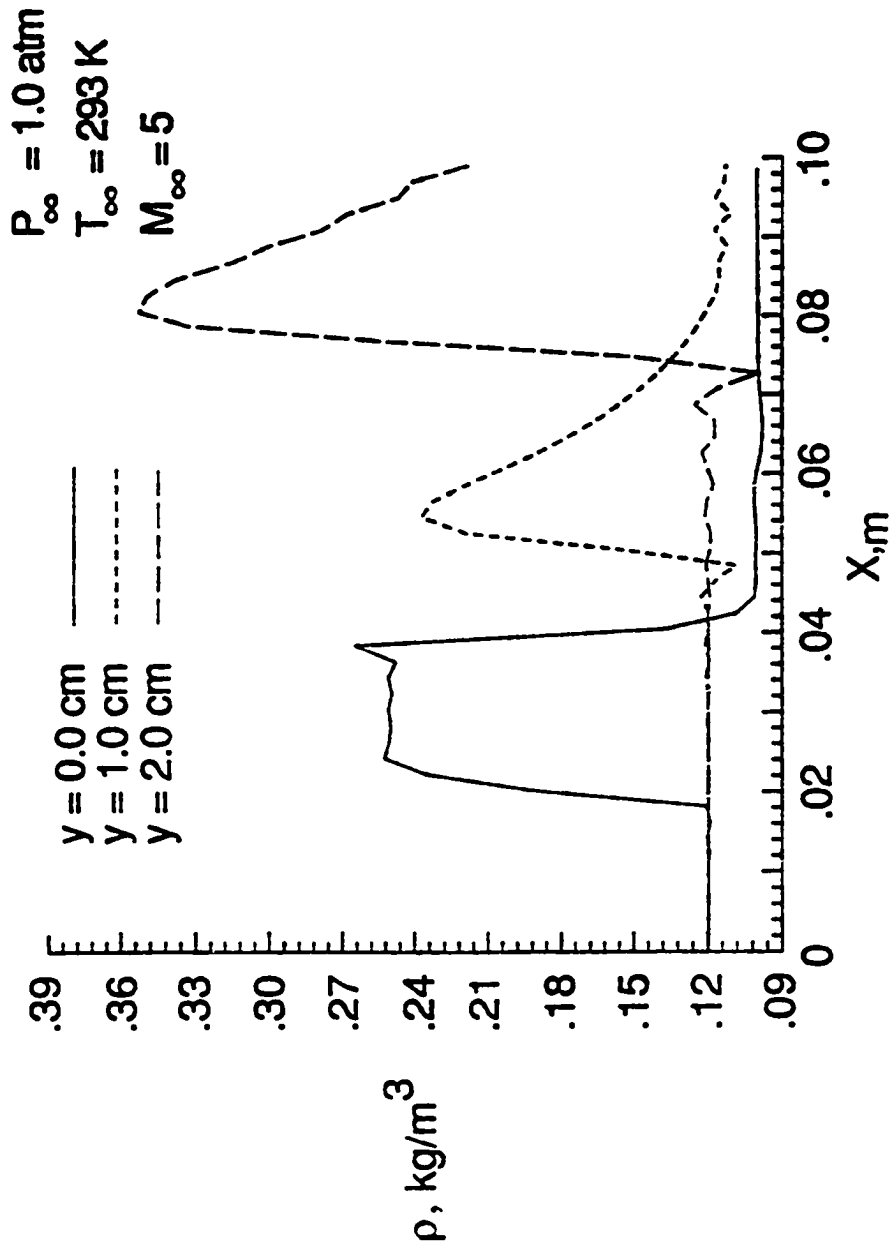

Fig. 5.4 Density variation with x for inviscid flow by finite volume scheme.

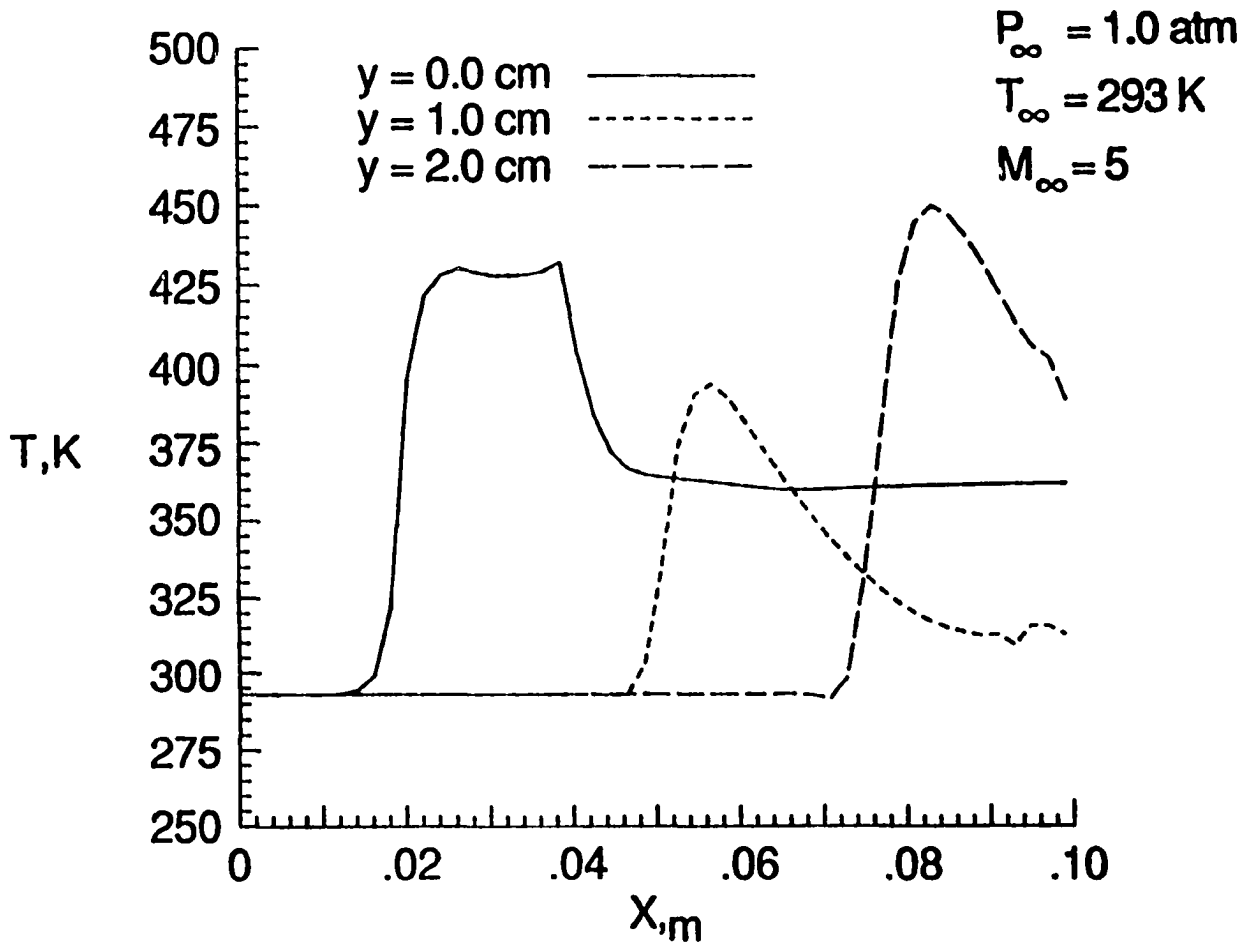

Fig. 5.5 Temperature variation with x for inviscid flow by finite volume TVD scheme.

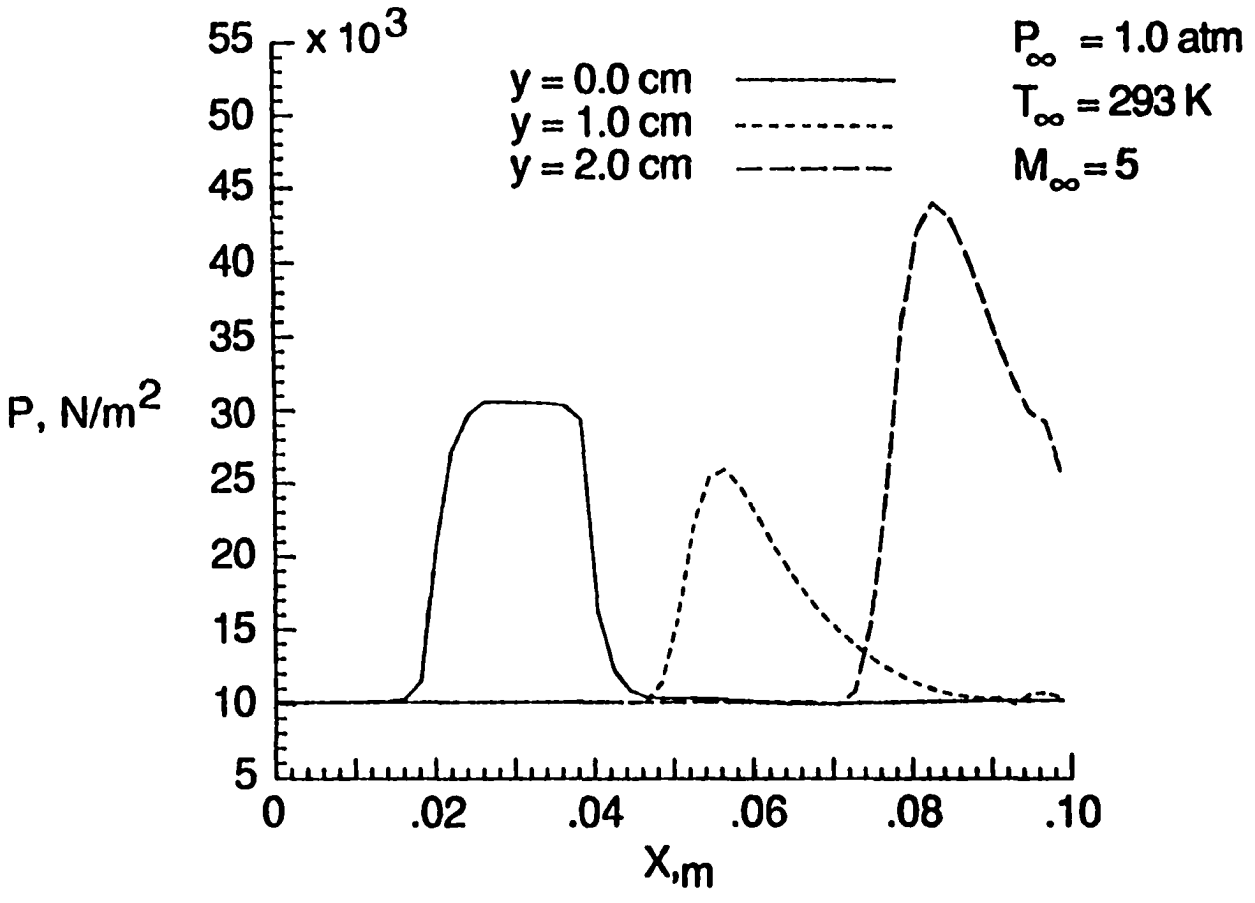

Fig. 5.6 Pressure variation with x for inviscid flow by finite volume TVD scheme.

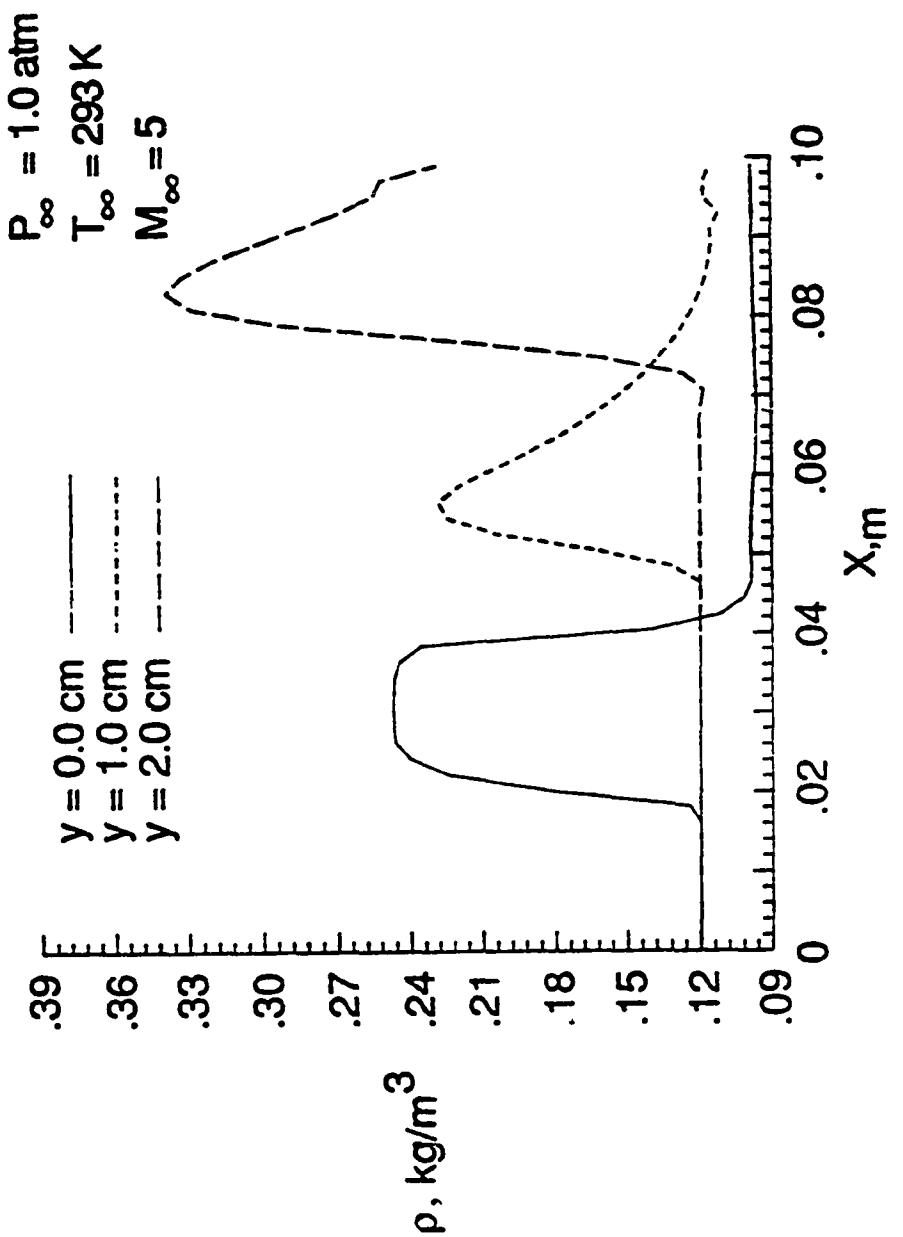

Fig. 5.7 Density variation with x for inviscid flow by finite volume TVD scheme.

the coefficient $\varepsilon^{(2)}$ is set equal to 1/2 in the neighborhood of a shock wave. The temperature, pressure, and density evaluated by the finite difference scheme are plotted at the lower wall, center of the channel, and the upper wall in Figs. 5.8-5.10, respectively. The density at the lower wall is slightly overpredicted in comparison to ideal gas flowing through a ten degree shock; consequently, the temperature is slighly underpredicted.

For the solution of the viscous flow, two test cases were selected. The first case considered in that of a supersonic flow over a flat plate and the second case is of a supersonic flow in a channel. The simplest way to test the behavior of a Navier-Stokes solver is to solve for the flow with a low Reynolds number over a flat plate. In this case, a temperature equal to the stagnation temperature was specified at the wall. Using the fluid properties specified in Table 5.1 and a uniform grid distribution, variations in the temperature and the two velocity components were calculated at the exit plane and these are plotted in Figs. 5.11-5.13. The profiles show very good agreement with the calulations performed by Carter [53]. The oscillation observed in Figs. 5.11 and 5.12 are due to the bow shock from the plate leading edge.

In the second case, the solutions are obtained for the supersonic flow in the channel with a compression-expansion ramp. The free stream properties considered are $M_\infty = 5$, $T_\infty = 293K$, and $P_\infty = 0.1$ atm. The corresponding freestream Reynolds number at the exit plane is about 1.1×10^6. This is a significantly more difficult case compared to the first case. To capture the boundary layer, the grids are compressed near the boundaries; consequently, the grid aspect ratio becomes very large. The non-uniformity of the grid creates significant problems for some schemes. For example, the finite volume scheme with Dampl

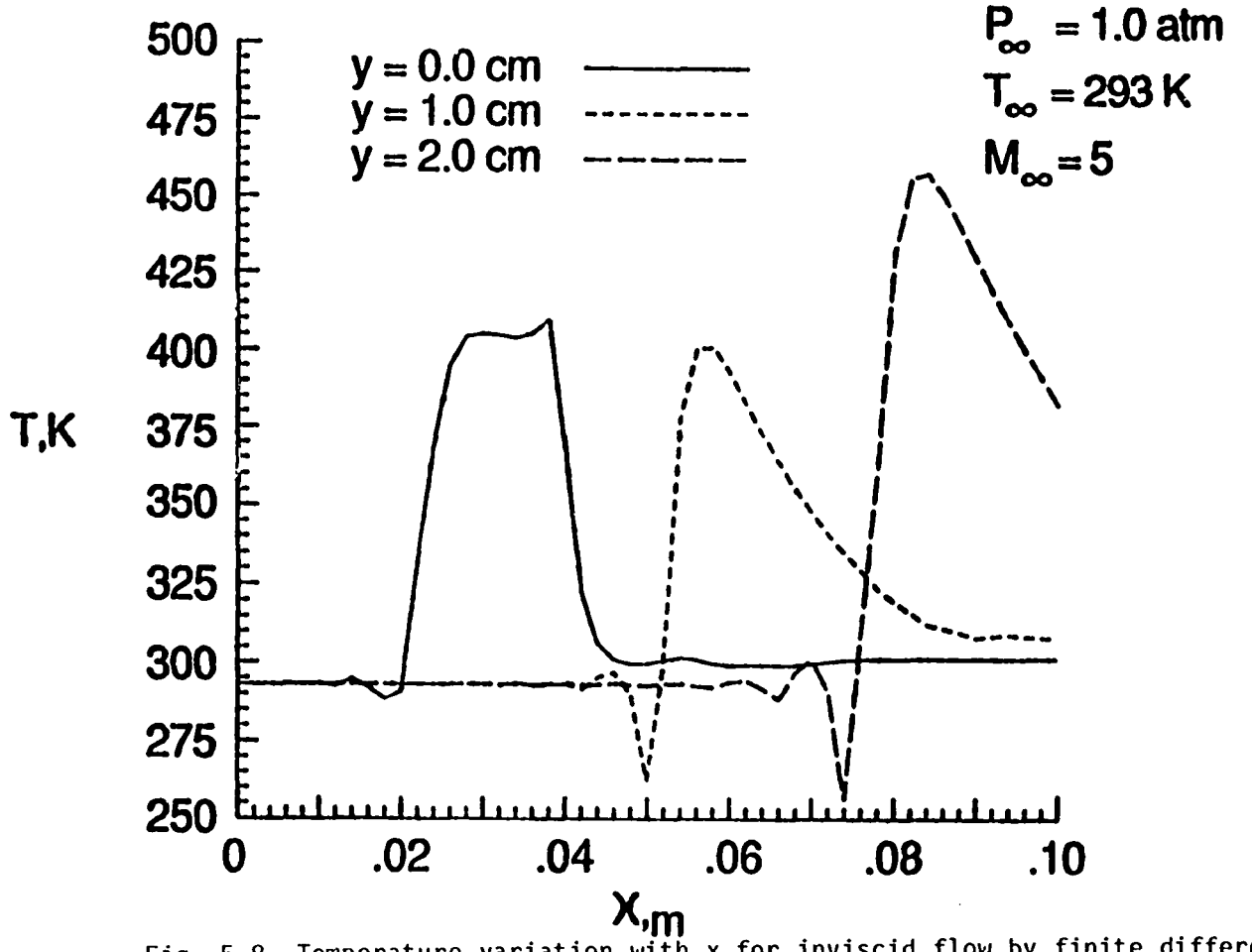

Fig. 5.8 Temperature variation with x for inviscid flow by finite difference scheme.

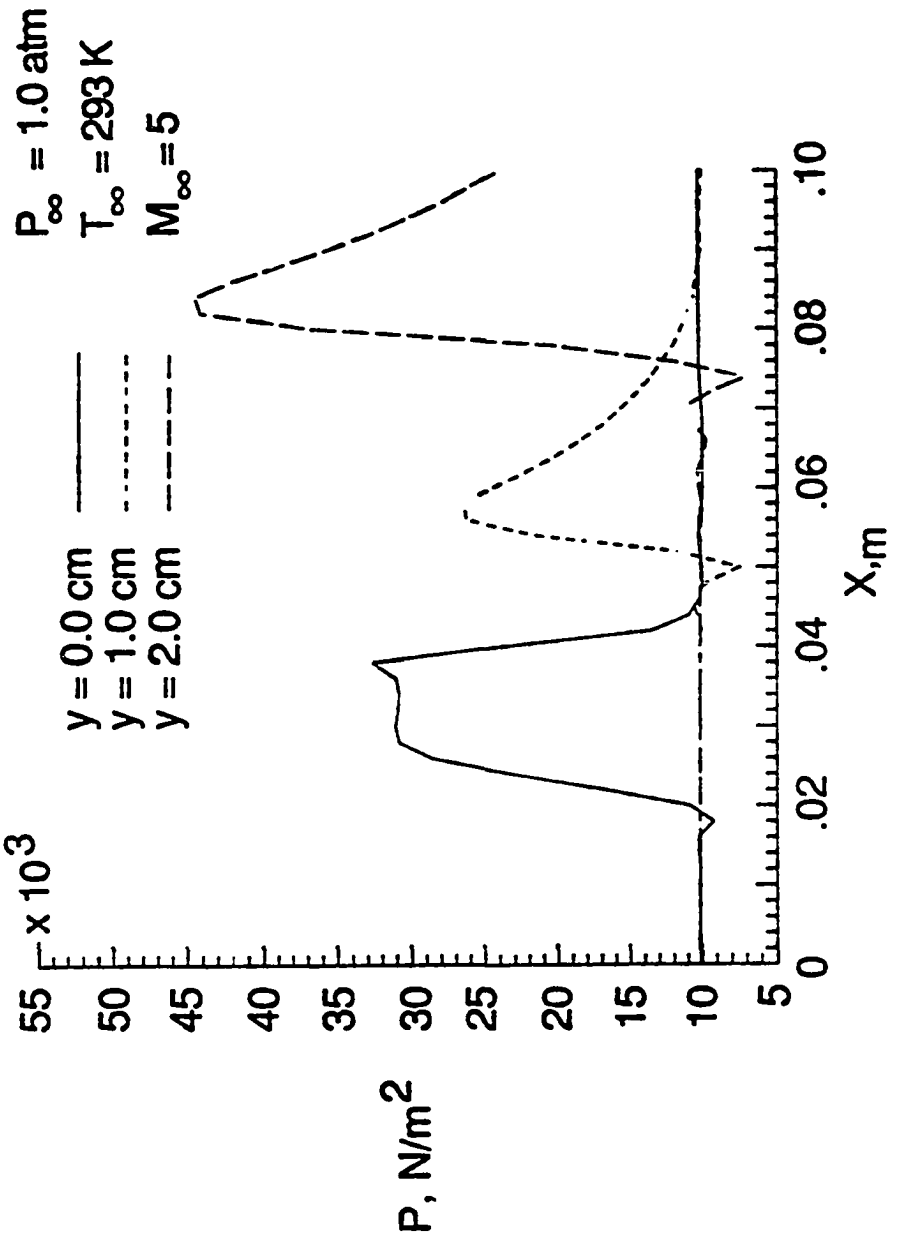

Fig. 5.9 Pressure variation with x for inviscid flow by finite difference scheme.

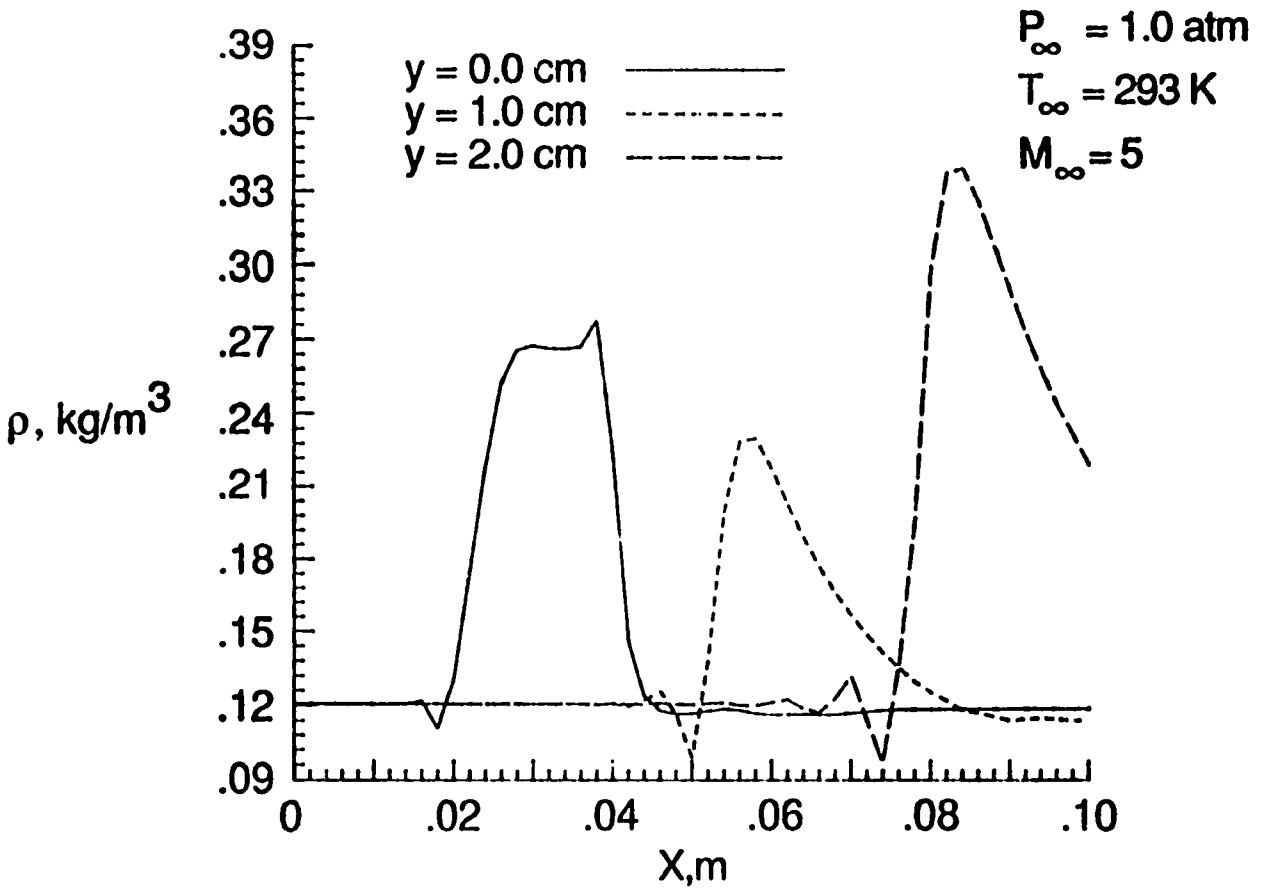

Fig. 5.10 Density variation with x for inviscid flow by finite difference scheme.

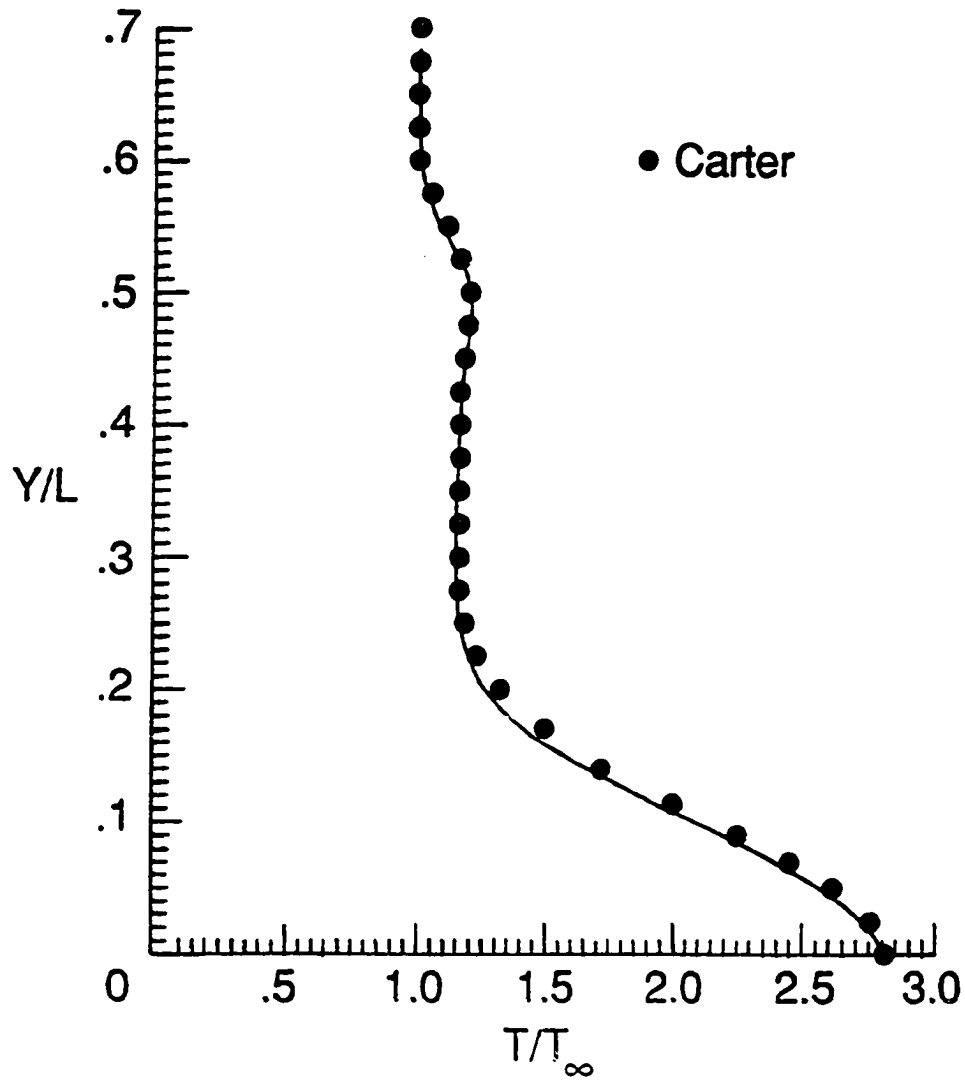

Fig. 5.11 Temperature vs. y at exit plane for flat plate.

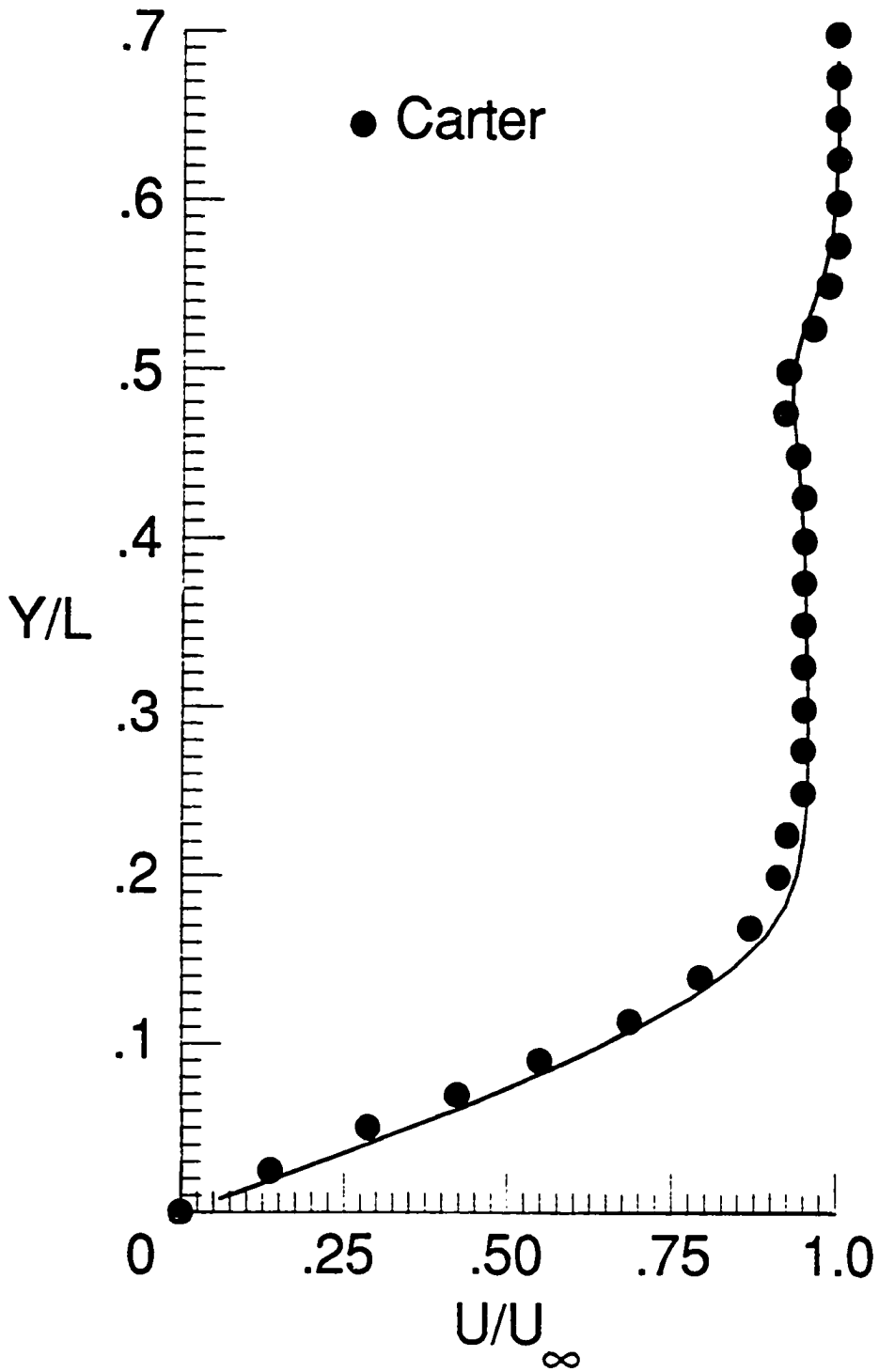

Fig. 5.12 Streamwise velocity vs. y at exit plane for flat plate.

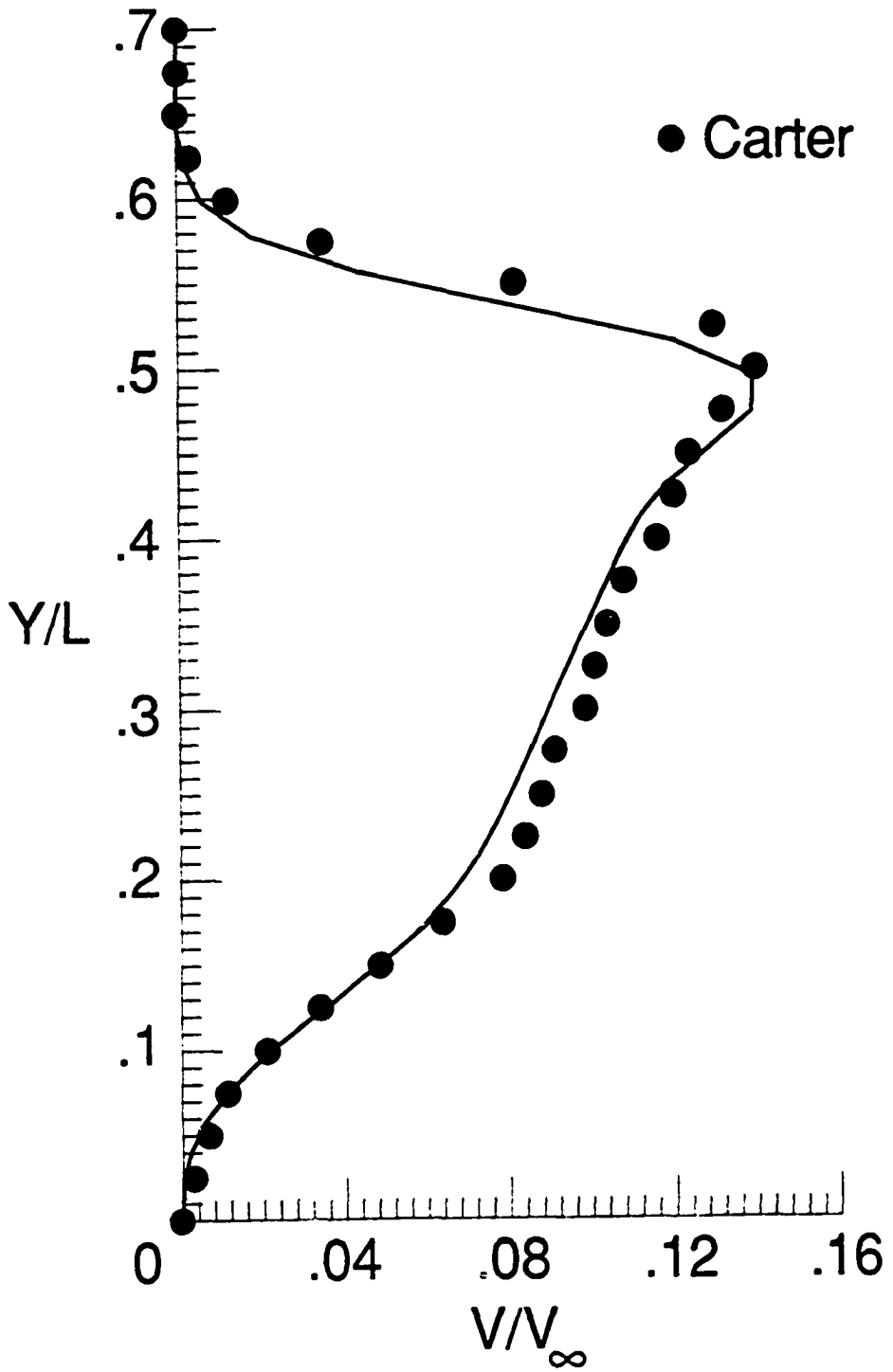

Fig. 5.13 Normal velocity vs. y at exit plane for flat plate.

Table 5.1 Flat Plate Test Data

Properties	Values	Dimensions
P_∞	7.0	N/m^2
T_∞	216	^0K
u velocity	882	m/s
v velocity	0.0	m/s
R_{eL}	1000.0	
Pr	0.72	
C_p	1000.0	J/kg K
C_v	714.0	J/kg K
L	0.15	m
Grid	51x51	

could accurately predict the pressure profiles through the channel, but it is not capable of predicting the temperature or velocity profiles. It was found that the Jameson scheme with Damp1 is capable of solving the viscous flow for a Reynolds number of up to ten thousand. For flows with Reynolds numbers on the order of a million and above, the viscous properties could not be predicted accurately. Damp1 was originally developed for the solution of inviscid flows on a grid with an aspect ratio of order one. For the solution of viscous flows, it is not unusual to have a grid with an aspect ratio on the order of two to three. This non-uniformity creates an excessive amount of damping in the flow direction and insufficient damping in the normal direction. Various investigators [36, 54] have suggested different techniques to make the damping uniform in both directions. It was found that by substituting Δt_x and Δt_y instead of Δt in Eq. (4.23), that the damping became more uniform; this could also be achieved by substituting ρ instead of P in Eq. (4.24). Of course, this modification requires the readjustment of coefficients, $K^{(2)}$ and $K^{(4)}$ in Eqs. (4.25). By employing Damp2 instead of Damp1, the scheme became nonoscillatory, robust, and more accurate. The solution was obtained for Reynolds numbers of one million and ten million with two different grids. The results showed the same trend as the results of finite difference scheme.

Figures 5.14-5.19 illustrate the pressure and temperture profiles for 51x51 and 101x51 grids and for freestream properties of P_∞ = .1 atm, T_∞ = 293K, and M_∞ = 5. Figures 5.14 and 5.15 illustrate the pressure profiles at the lower wall and the center of the channel, and Fig. 5.16 represents the pressure at the upper wall. The temperature profiles at

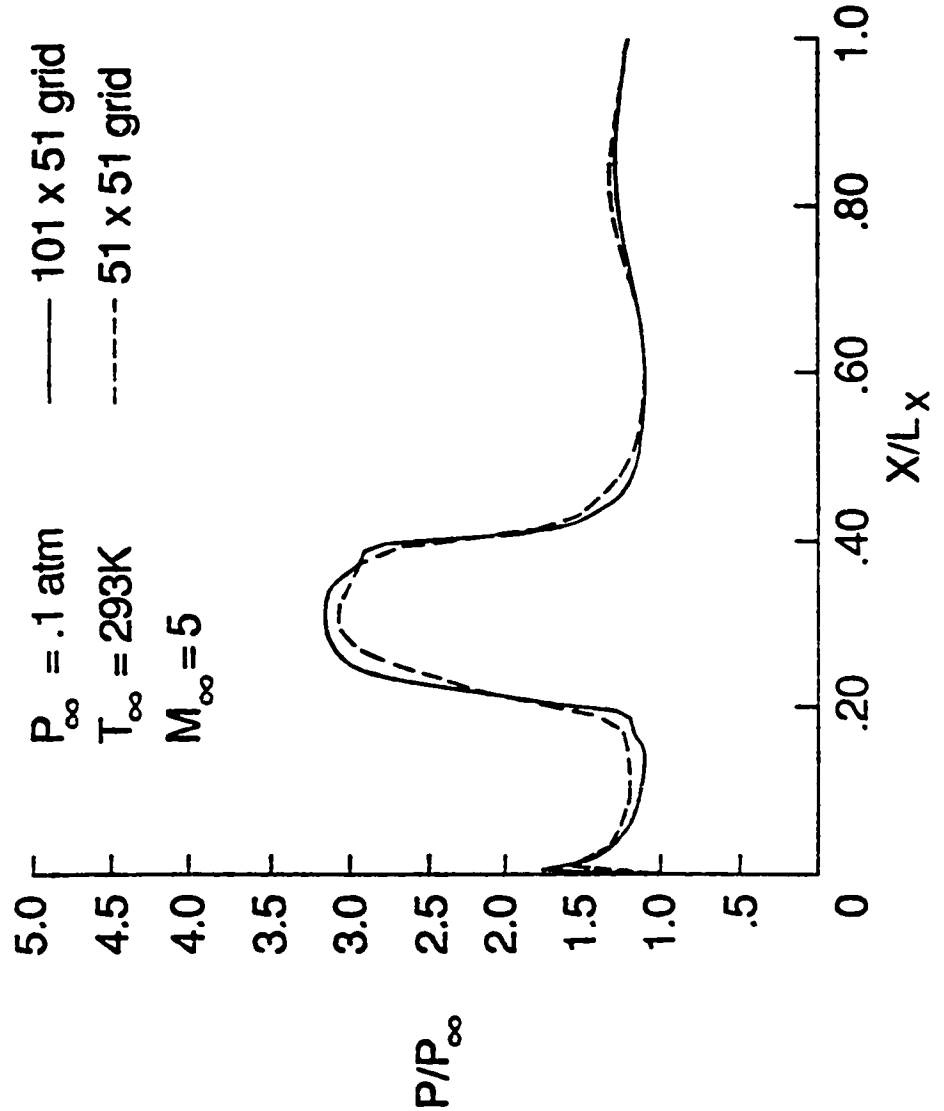

Fig. 5.14 Pressure variation with x for viscous flow with two different grids (J = 2).

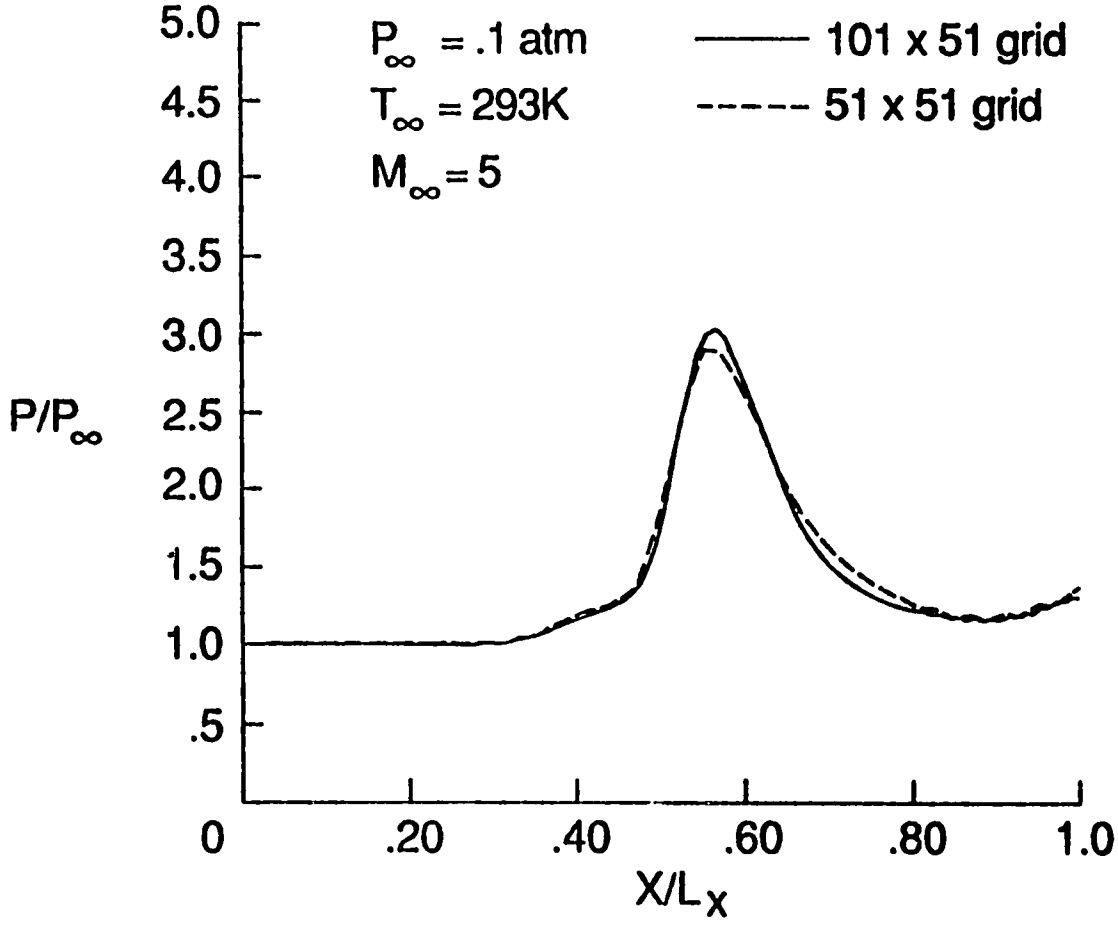

Fig. 5.15 Centerline pressure variation with x for viscous flow with two different grids (J = 25).

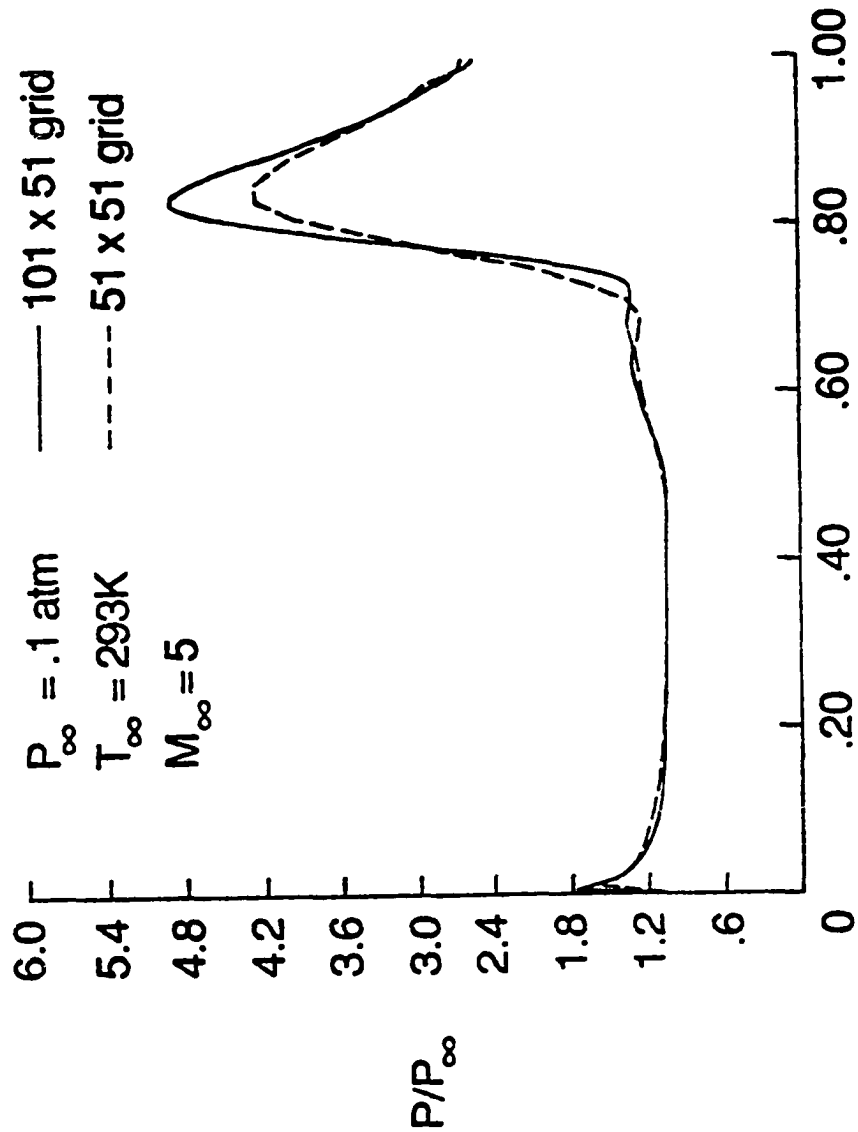

Fig. 5.16 Pressure variation with x for viscous flow with two different grids (J = 50).

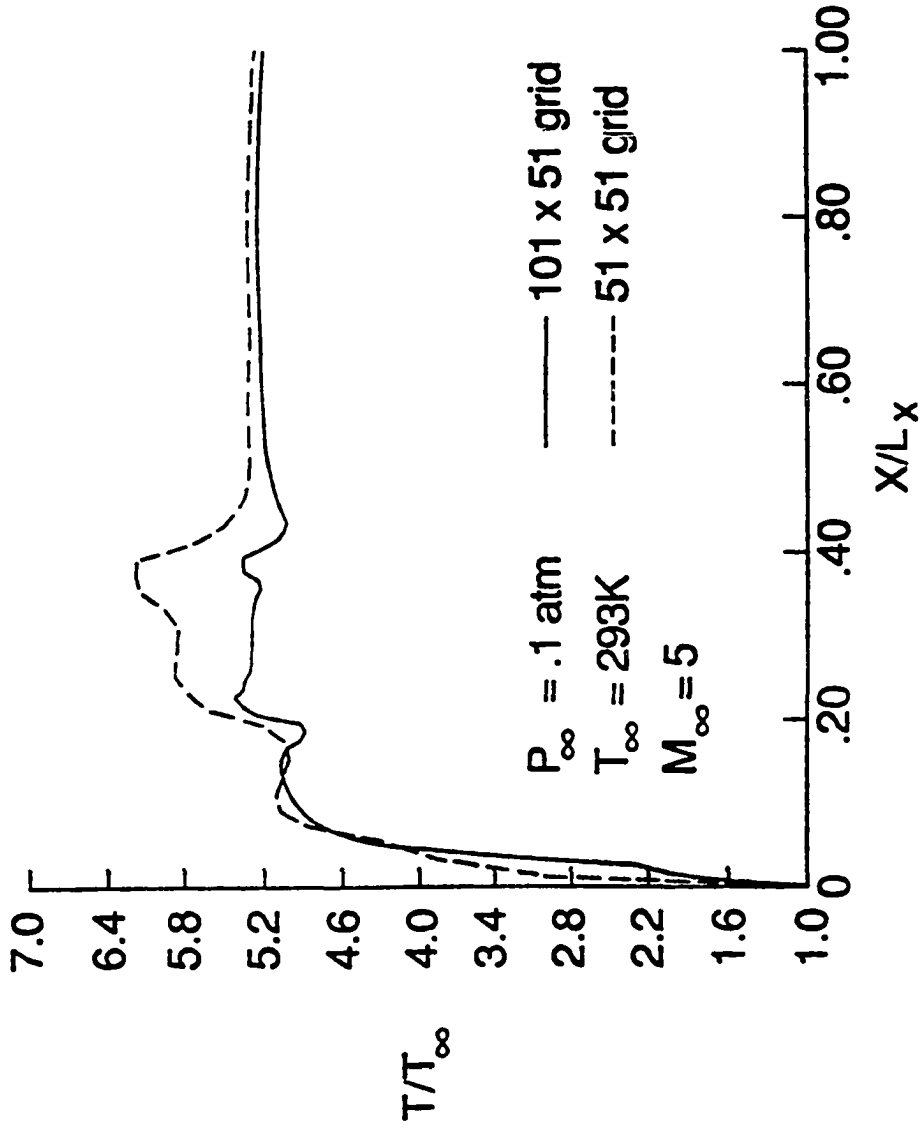

Fig. 5.17 Temperature variation with x for viscous flow with two different grids (J = 2).

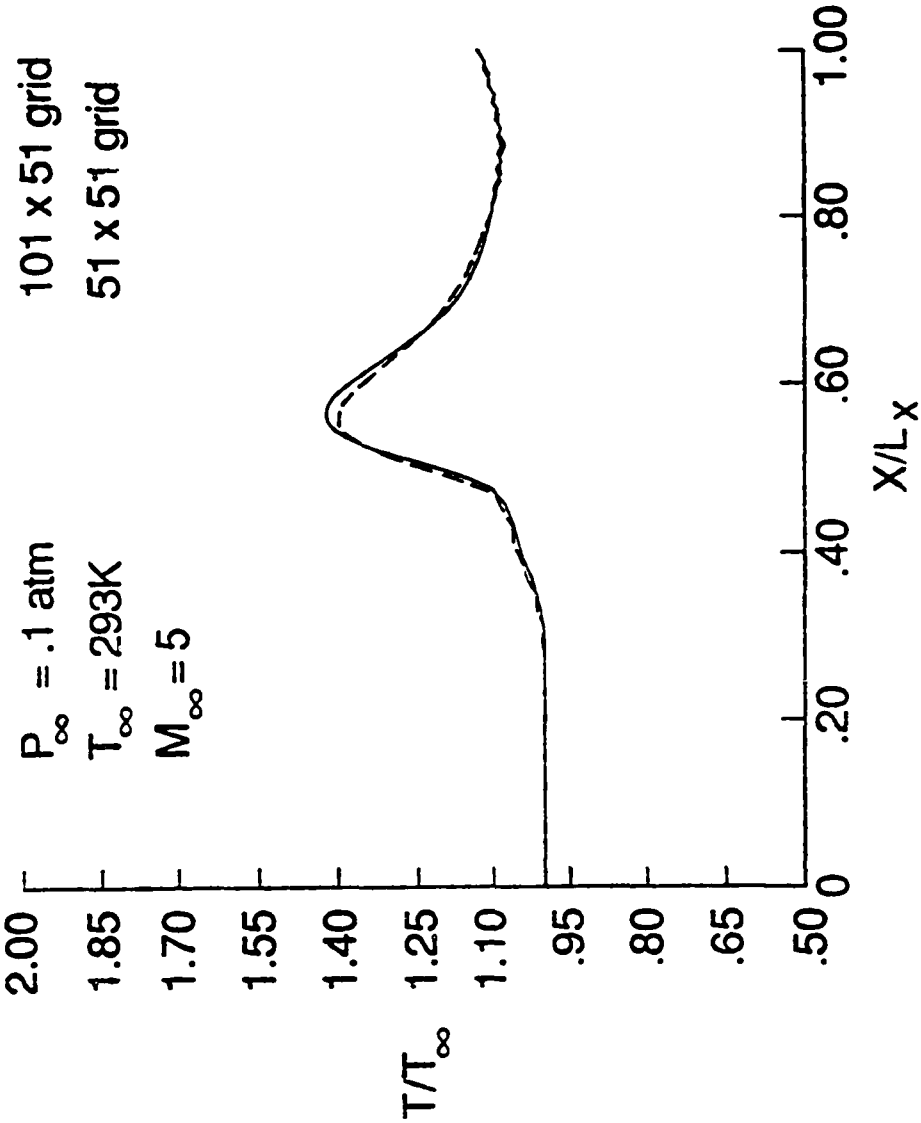

Fig. 5.18 Centerline temperature variation with x for viscous flow with two different grids (J = 25).

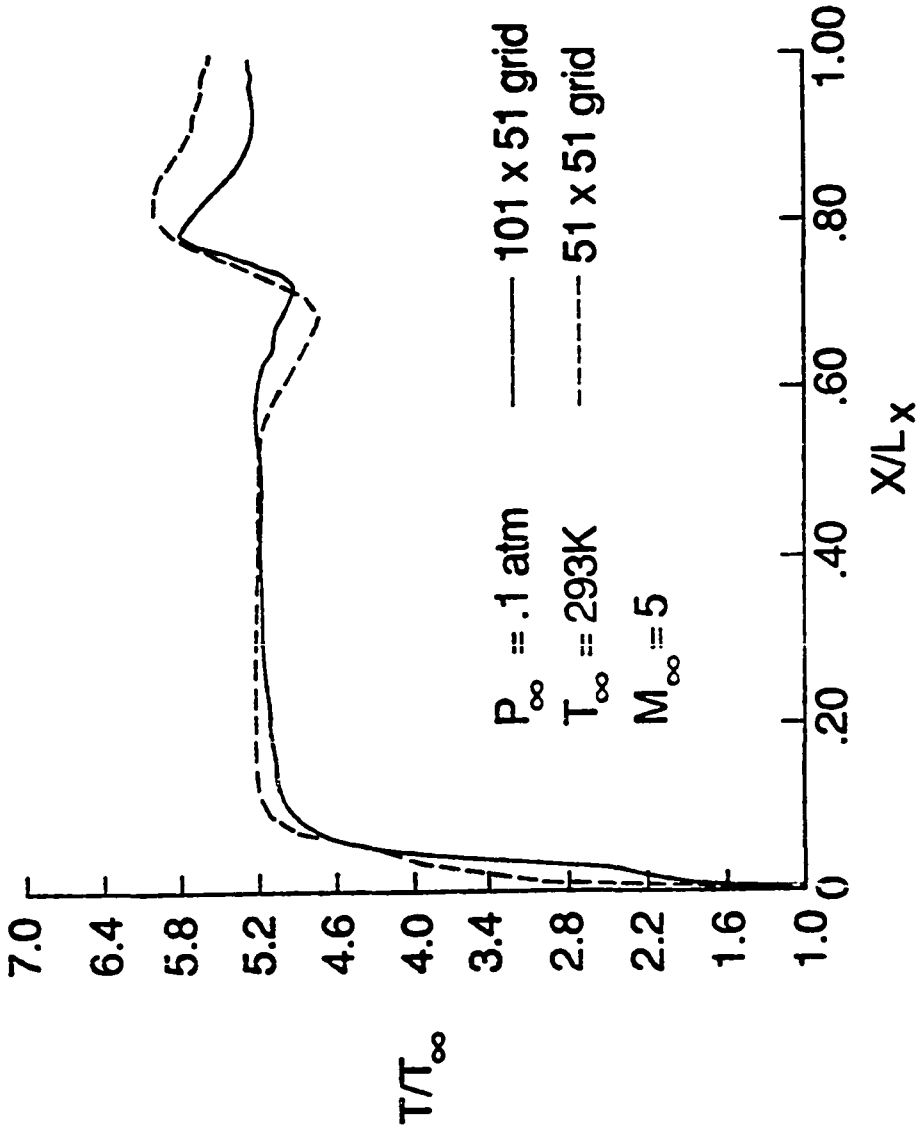

Fig. 5.19 Temperature variation with x for viscous flow with two different grids (J = 50).

these locations are plotted in Figs. 5.17-5.19. Reducing the number of grid points in the flow direction resulted in higher temperatures and lower pressure through the shock within the boundary layer. This is due to the excessive amount of artificial viscosity in the streamwise direction. For optimum results, grid must be compressed in the streamwise direction for the high gradient regions to reduce the grid aspect ratio.

The viscous flow properties were calculated by the finite difference and finite volume schemes; the results are compared with the calculations performed by Chakravarthy [55] using the Roe scheme. The pressure profiles are illustrated in Figs. 5.20-5.22 for the same three locations across the channel as in Figs. 5.14-5.19. The calculated results predict a pressure jump at the inlet, which is caused by the presence of a shock from the leading edge of the channel. Downstream of the channel on the lower wall there is an increase in the pressure. A close examination of the results showed that due to the interaction of leading edge shock with the shock and expansion fans from the compression-expansion corners, the velocity vector in that region has an angle less than one degree with the boundaries. The interaction of the flow with the lower wall creates a series of Mach waves which causes a small increase in the pressure. On the upper wall in the shock boundary layer interaction region, the pressure predicted by the finite difference scheme shows an oscillation. The calculated results compare very well with the Roe scheme. Figures 5.23-5.25 illustrate the streamwise velocity for the same locations as pressure. At the compression corner, the MacCormack scheme shows the flow to be separated, while the other two schemes predicted the same trend but the

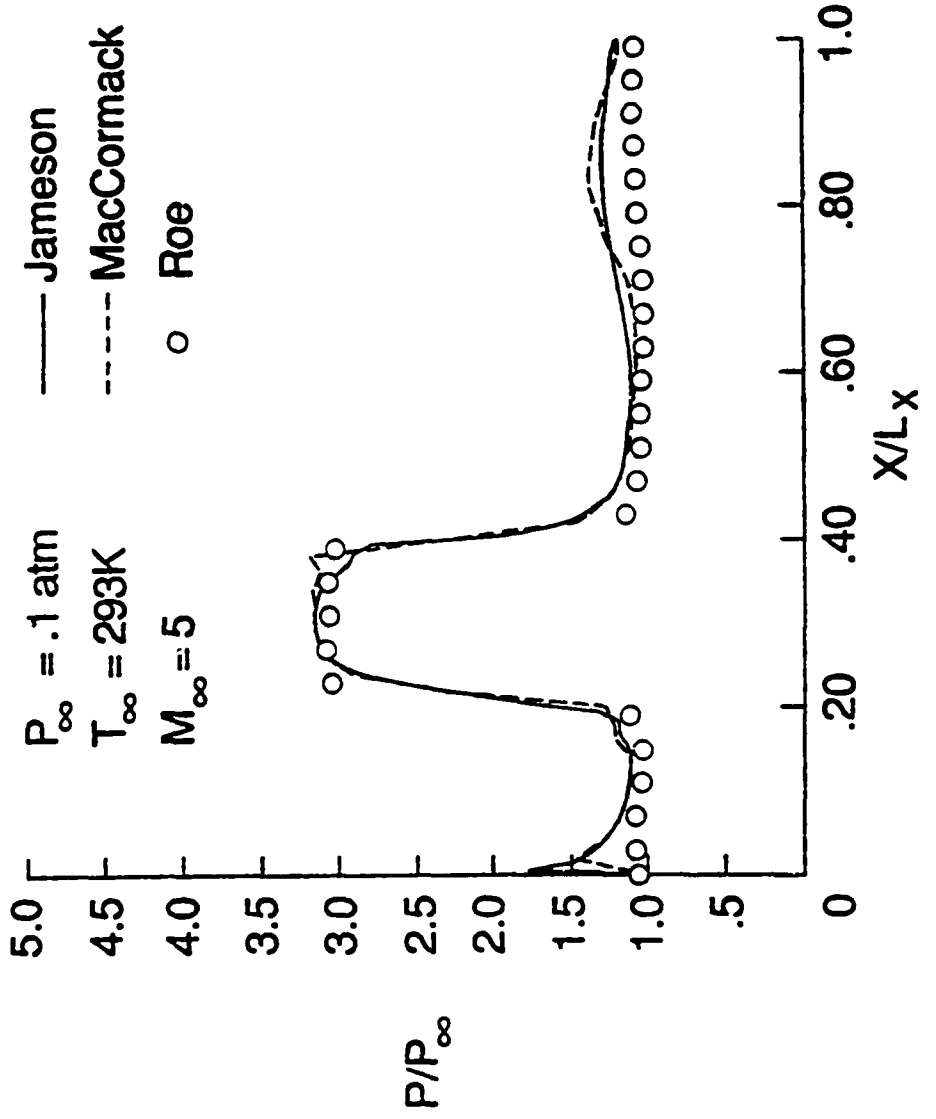

Fig. 5.20 Pressure variation with x for viscous flow (J = 2).

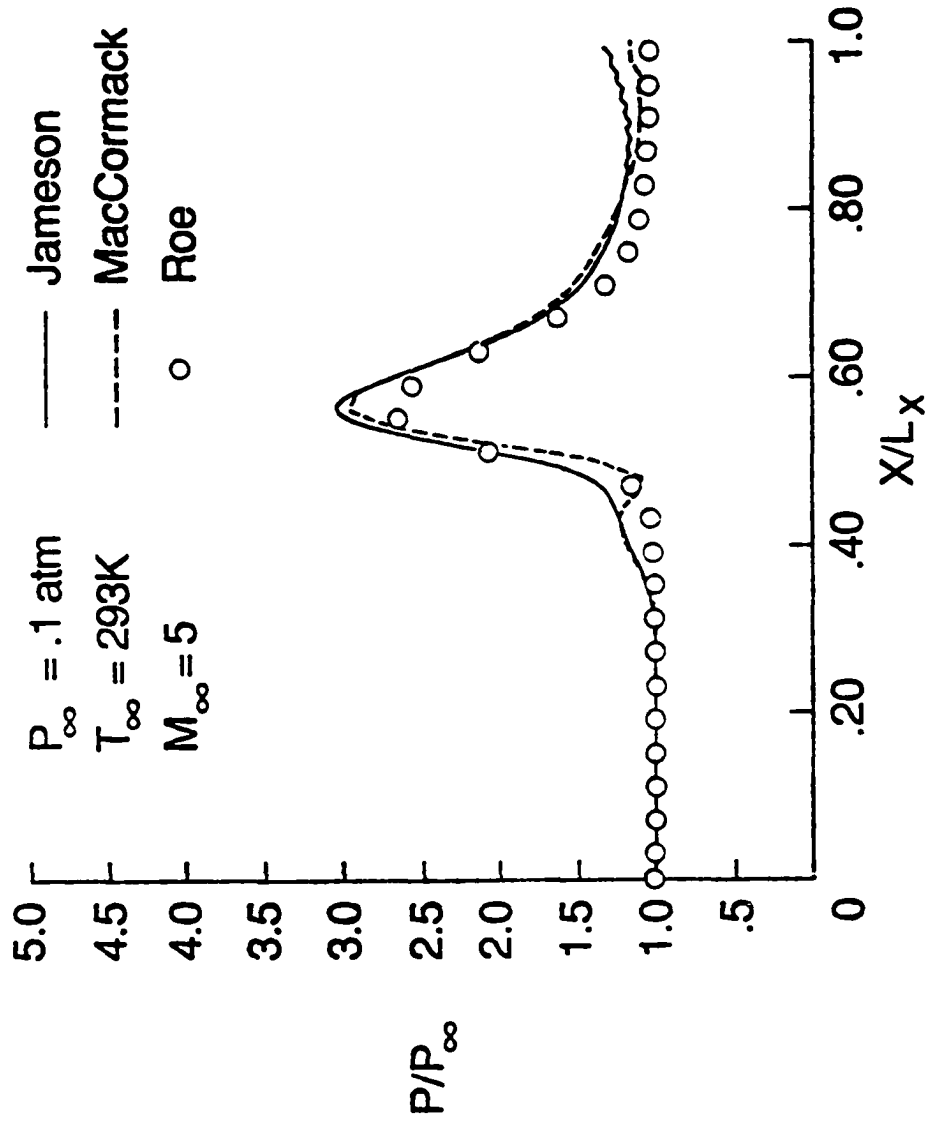

Fig. 5.21 Centerline pressure variation with x for viscous flow (J = 25).

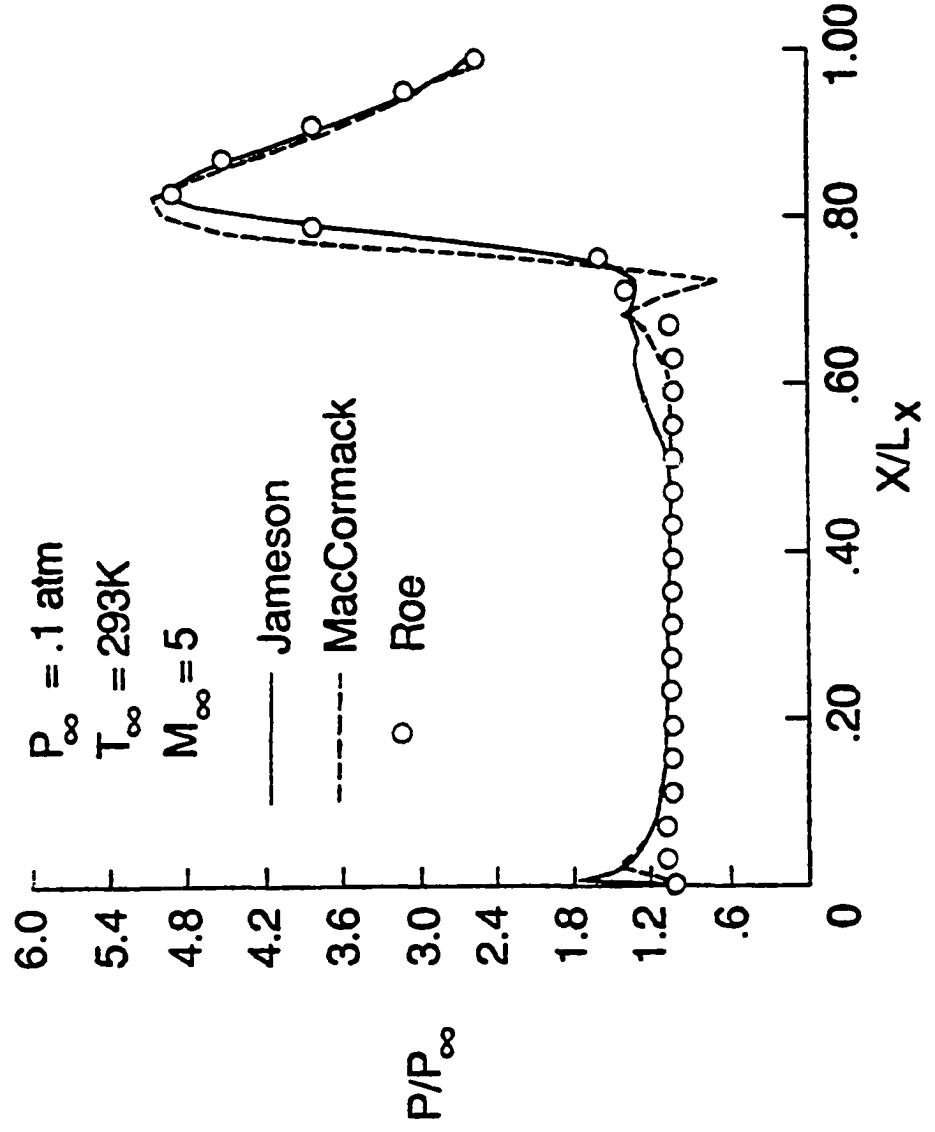

Fig. 5.22 Pressure variation with x for viscous flow (J = 50).

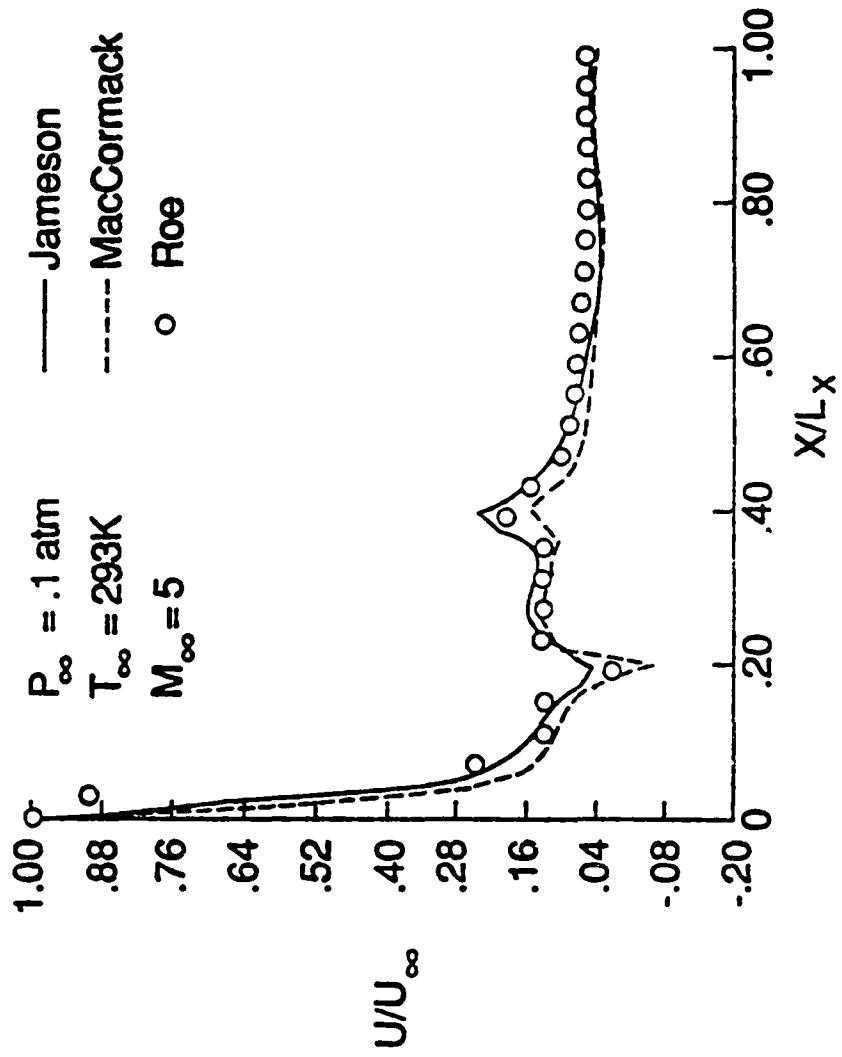

Fig. 5.23 Streamwise velocity variation with x for viscous flow (J = 2).

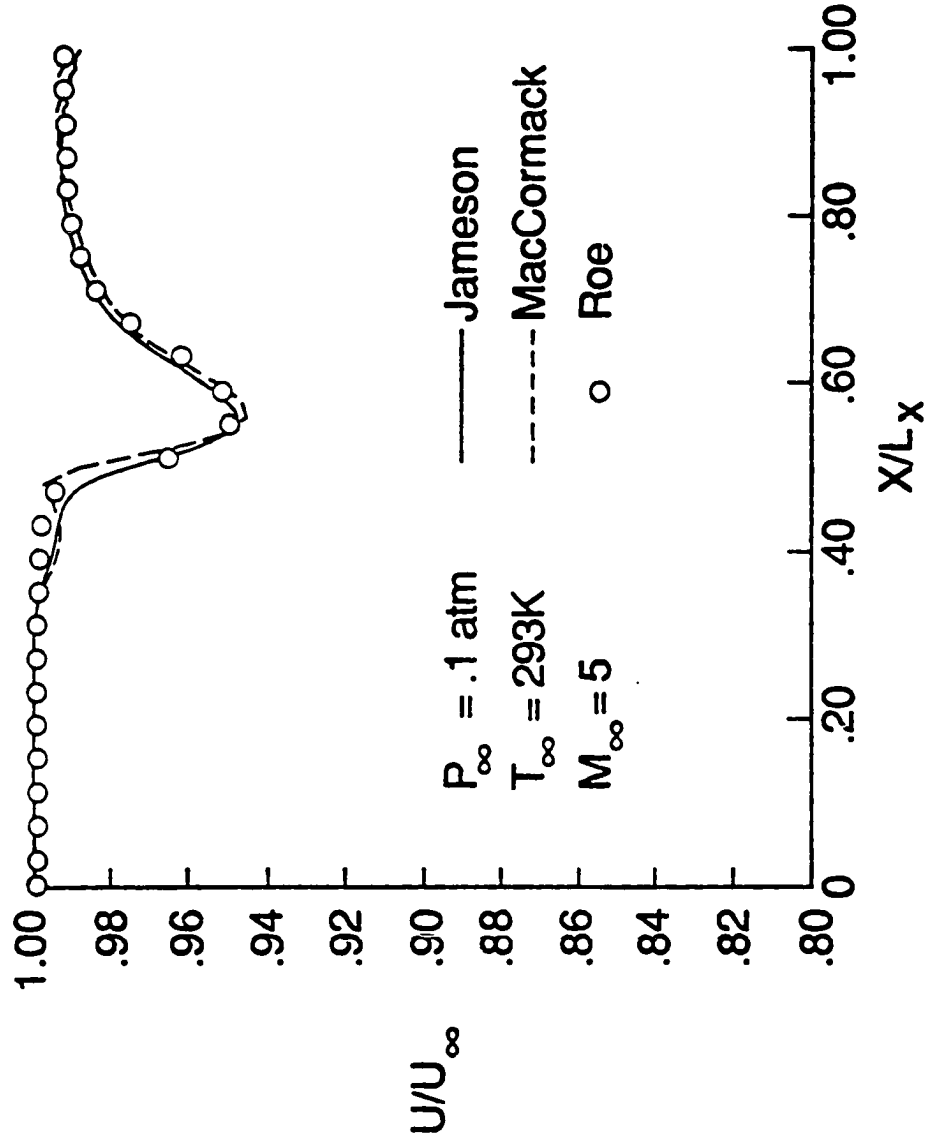

Fig. 5.24 Centerline velocity variation with x for viscous flow (J = 25).

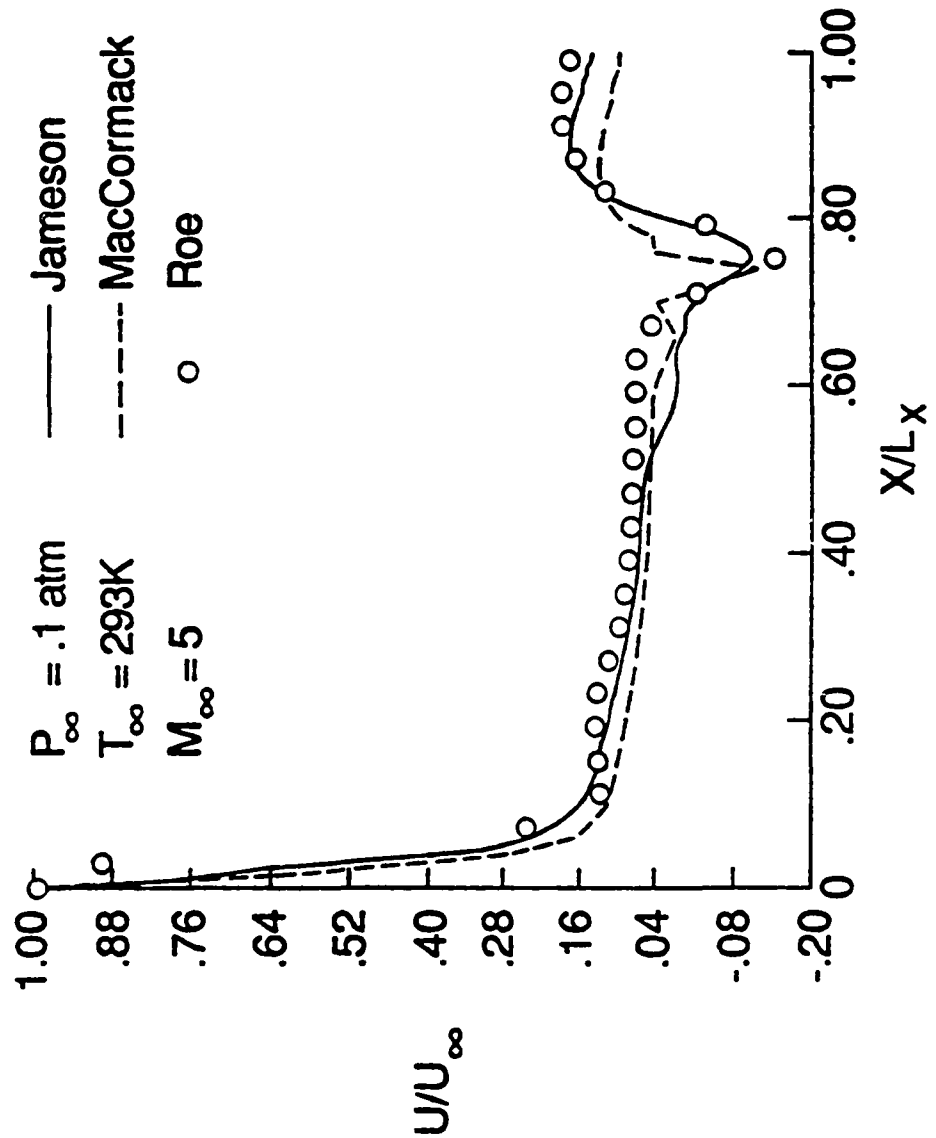

Fig. 5.25 Streamwise velocity variation with x for viscous flow (J = 50).

flow was not quite separated. The shock interaction with the upper boundary creates a small separation bubble. The flow is fully separated at $X/L_x = 0.7$; this is predicted by all three schemes. The streamwise velocity illustrated in Figs. 5.24 and 5.25 indicate that the Jameson scheme predicts a decrease in velocity before the shock and the separation region. This is due to the excessive amounts of artificial viscosity in the neighborhood of shocks when the grid spacing is large in streamwise direction. To reduce the excessive amount of streamwise dissipation in the shock vicinity, the scaling factor (Eq. (4.23)) must be reduced. This can be achieved in two ways, one by reducing the grid cell area and the other by increasing the time step in the flow direction. Reducing the grid cell area in the shock vicinity requires more grid points. However, if there are enough points in the flow direction, this can be achieved by compressing the grid in the flow direction. For the highly stretched grid, it is recommended that R be scaled (Eq. (4.23)), with respect to local Δt_x for the flow direction and local Δt_y in the normal direction as opposed to Δt_{CFL} which was used in this study. Also, the results calculated using the finite volume scheme predict a faster drop in the velocity near the leading edge than the Roe's scheme.

Temperature profiles are shown in Figs. 5.26-5.28. Temperature is the most sensitive and difficult property to predict accurately. In the finite difference calculations, temperature is strongly dependent on the implication of the boundary conditions. In this work, it is assumed that the walls are adiabatic. This could be enforced by either $\partial T/\partial y \Big|_{y=0} = 0$ or $\partial H/\partial y \Big|_{y=0} = 0$ (Appendix E). The above results were obtained by enforcing the zero temperature gradient. The same trends are predicted by all three schemes. The approximate temperature

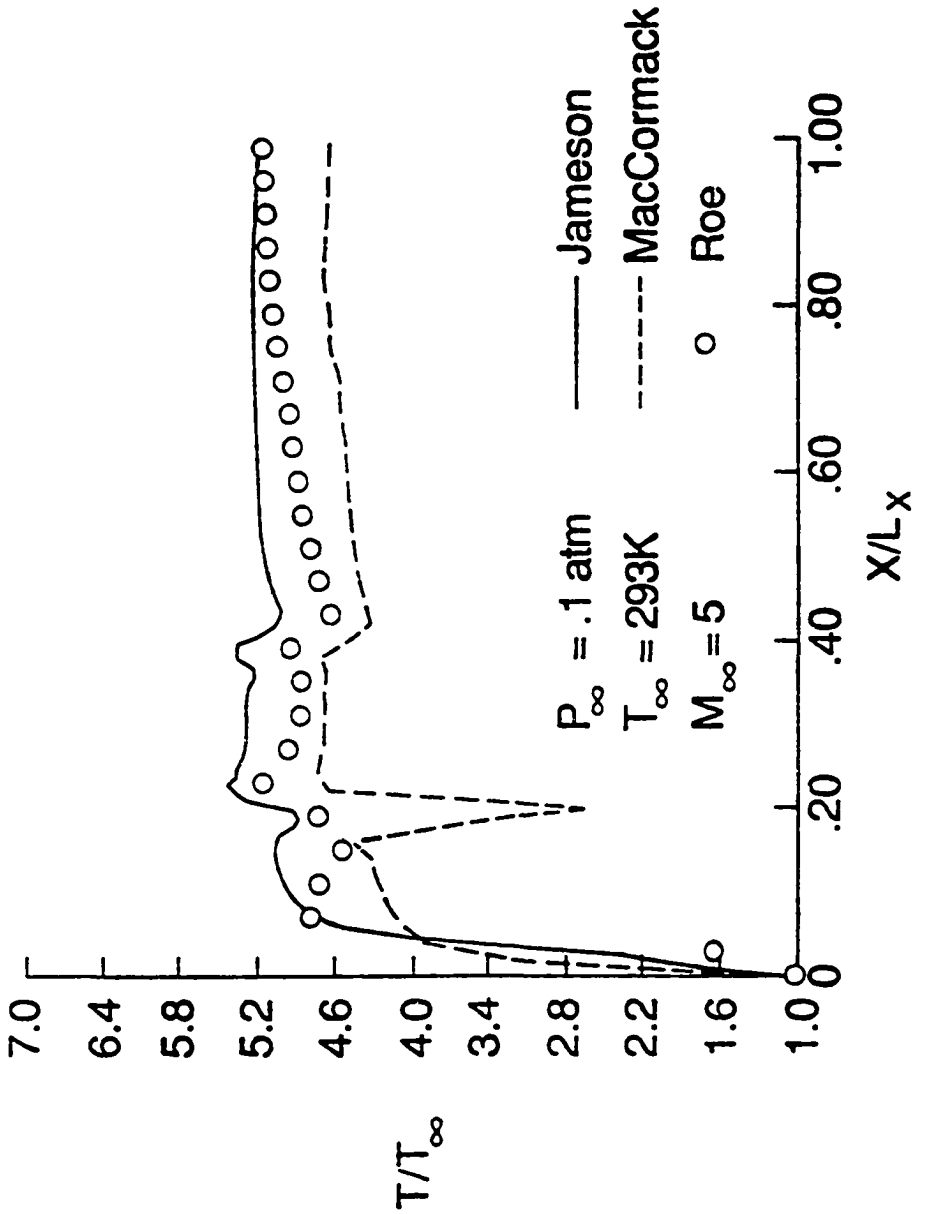

Fig. 5.26 Temperature variation with x for viscous flow ($T_w = T_1$, J = 2).

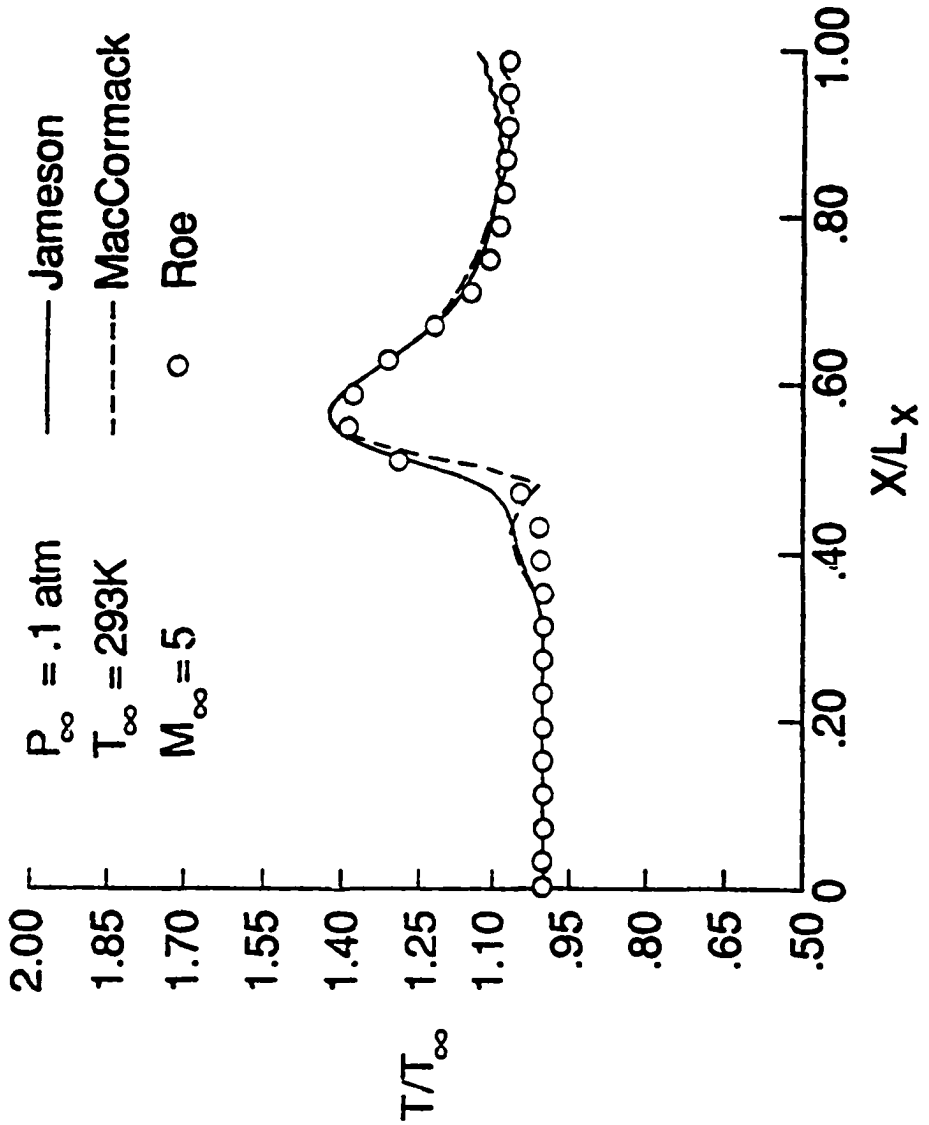

Fig. 5.27 Centerline temperature variation with x for viscous flow ($T_w = T_1$, J = 25).

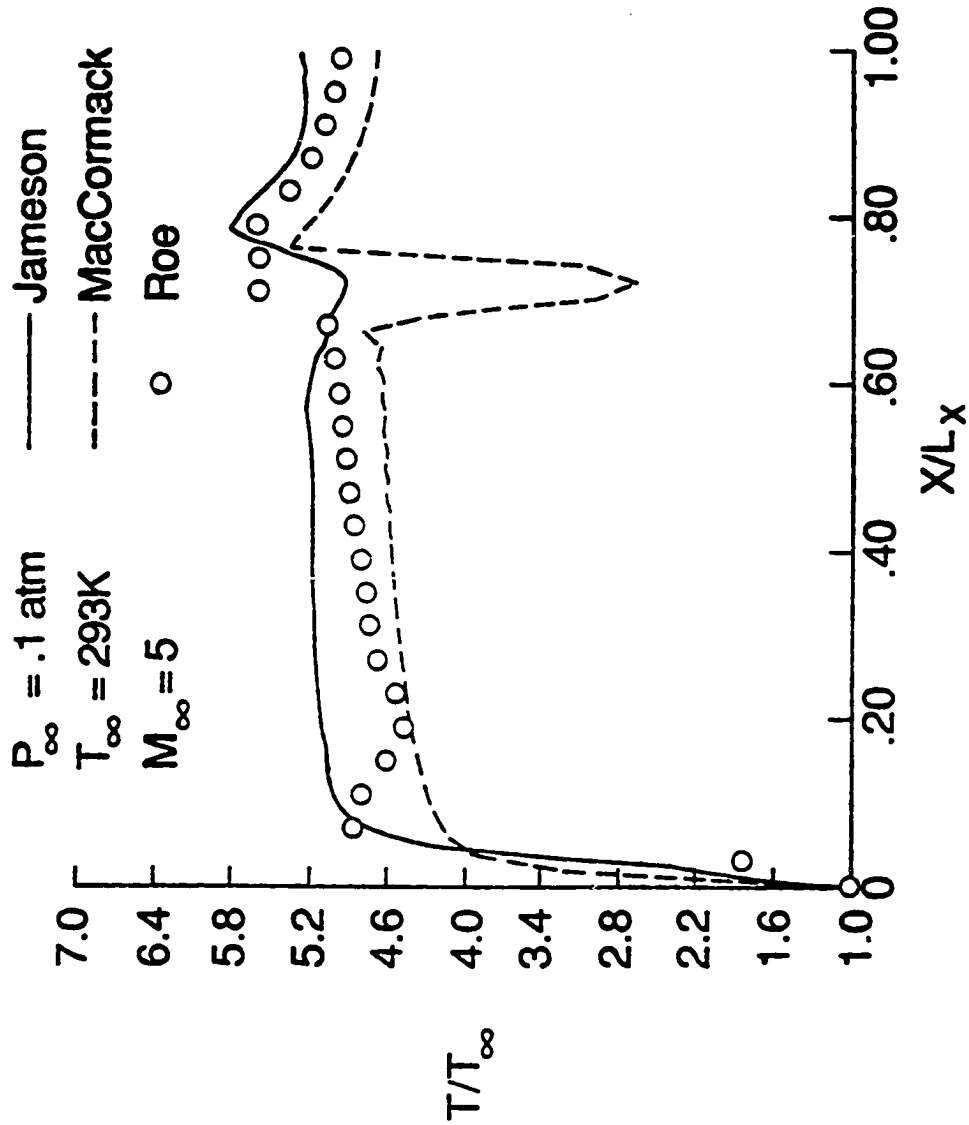

Fig. 5.28 Temperature variation with x for viscous flow ($T_w = T_1$, J = 50).

recovery factor for compressible laminar flow with $M_\infty = 5$ and $Pr = 0.72$ is 5.25 [56]. This value is predicted by the Jameson and Roe schemes towards the channel outlet. The above recovery factor can be predicted with the finite difference scheme by enforcing the zero enthalpy gradient at the boundary. Figures 5.29-5.31 illustrate the temperature profiles when zero enthalpy gradient was enforced for the finite difference scheme. Temperature increases very rapidly at the leading edge due to the flow stagnating from the free stream within one grid spacing.

5.2 Reacting and Radiating Flows

Before proceeding into the evaluation of the radiative heat transfer, the performance of the finite volume and difference schemes is compared for chemically reacting flows. Premixed hydrogen-air with an equivalence ratio of unity flows through a channel (Fig. 5.32) with a ten degree compression corner, and freestream conditions, $P_\infty = 1$ atm, $T_\infty = 900^0K$, $M_\infty = 4$. A switch is built into the code to prevent chemical reaction for temperatures below 1000°K. The results for O_2 and H_2O are plotted for two different locations across the channel in Figs. 5.33 and 5.34. Due to the high temperature in the boundary layer, the flow is ignited before the shock, but outside the boundary layer there is no chemical reaction in the flow before the shock wave. The finite difference scheme shows oscillatory behavior near the shock. The results predicted by both schemes are seen to be in a good agreement.

Radiative flux is a strong function of temperature and pressure gradients. The temperature gradient over a grid spacing is greater in the normal direction than the streamwise direction. Therefore, it is

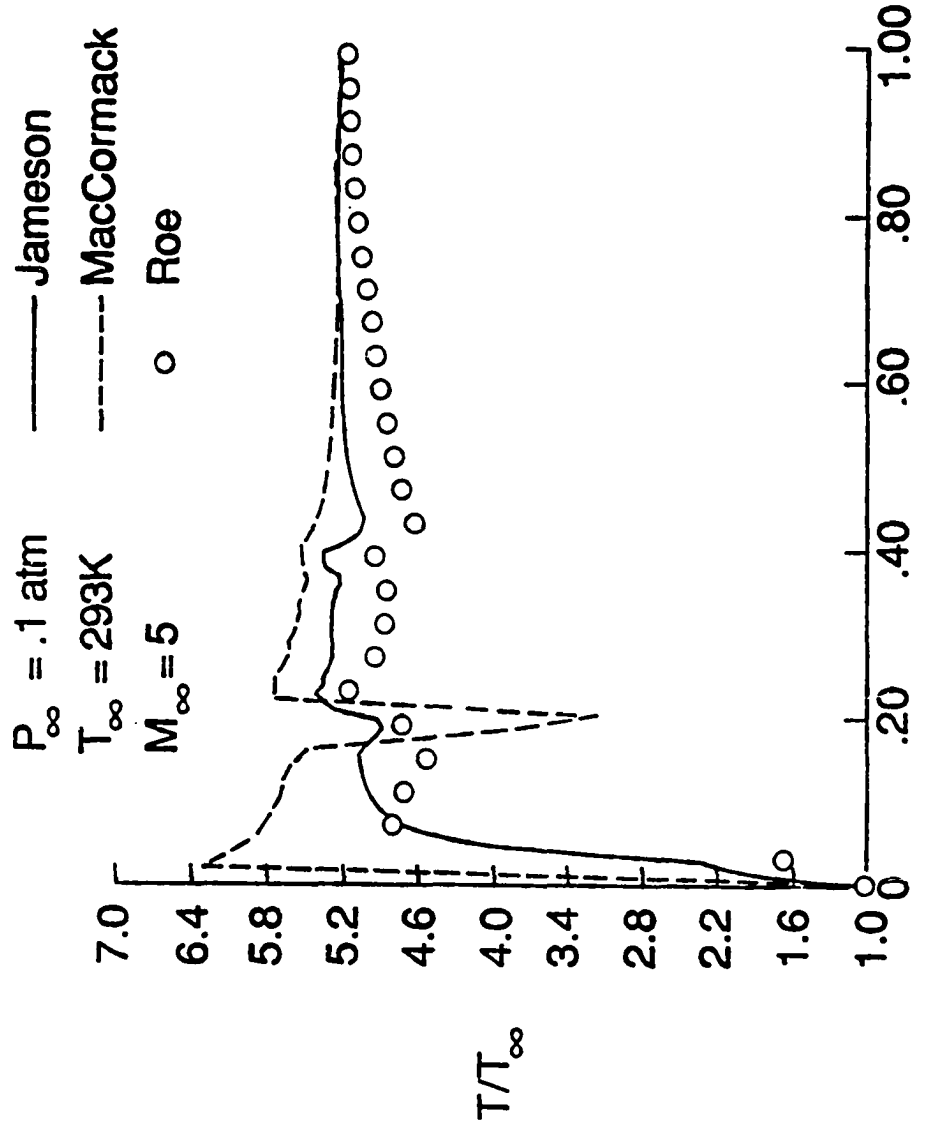

Fig. 5.29 Temperature variation with x for viscous flow ($H_w = H_1$, J = 2).

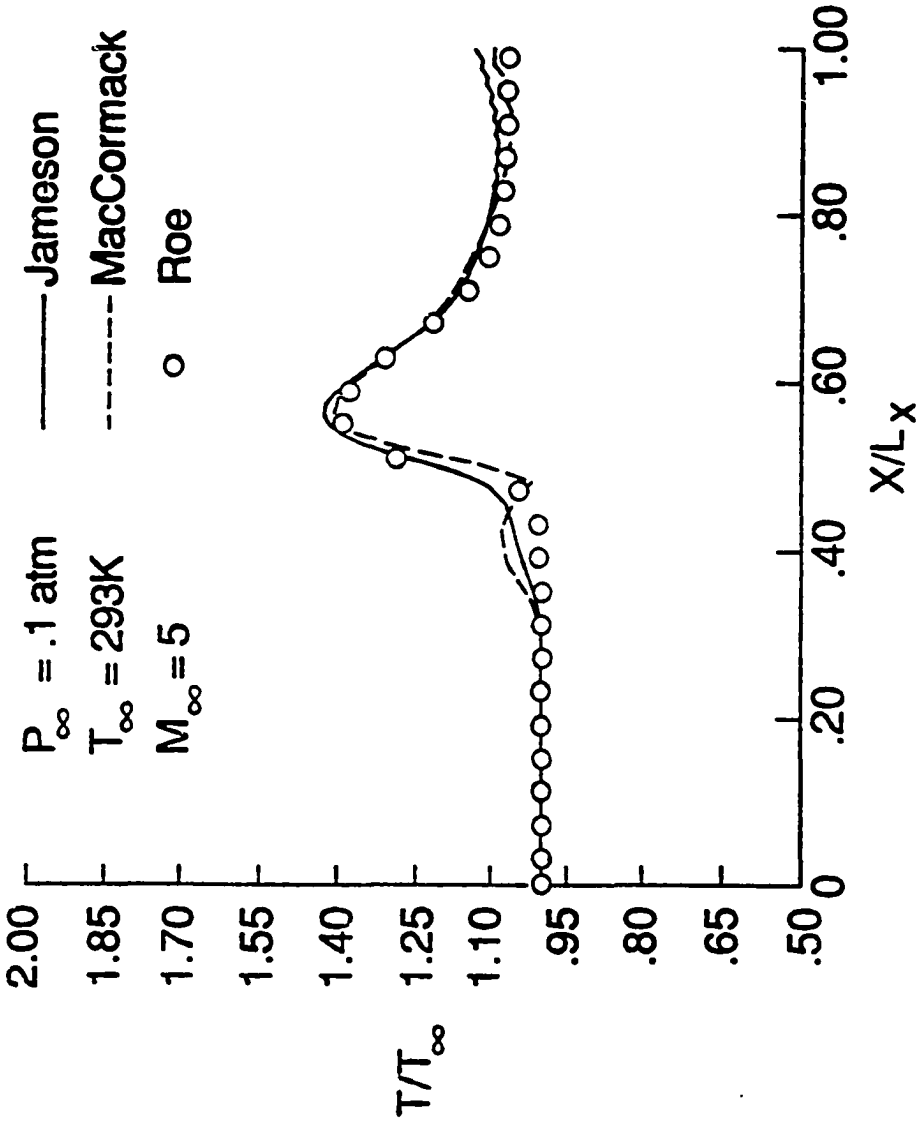

Fig. 5.30 Centerline temperature variation with x for viscous flow ($H_w = H_1$, J = 25).

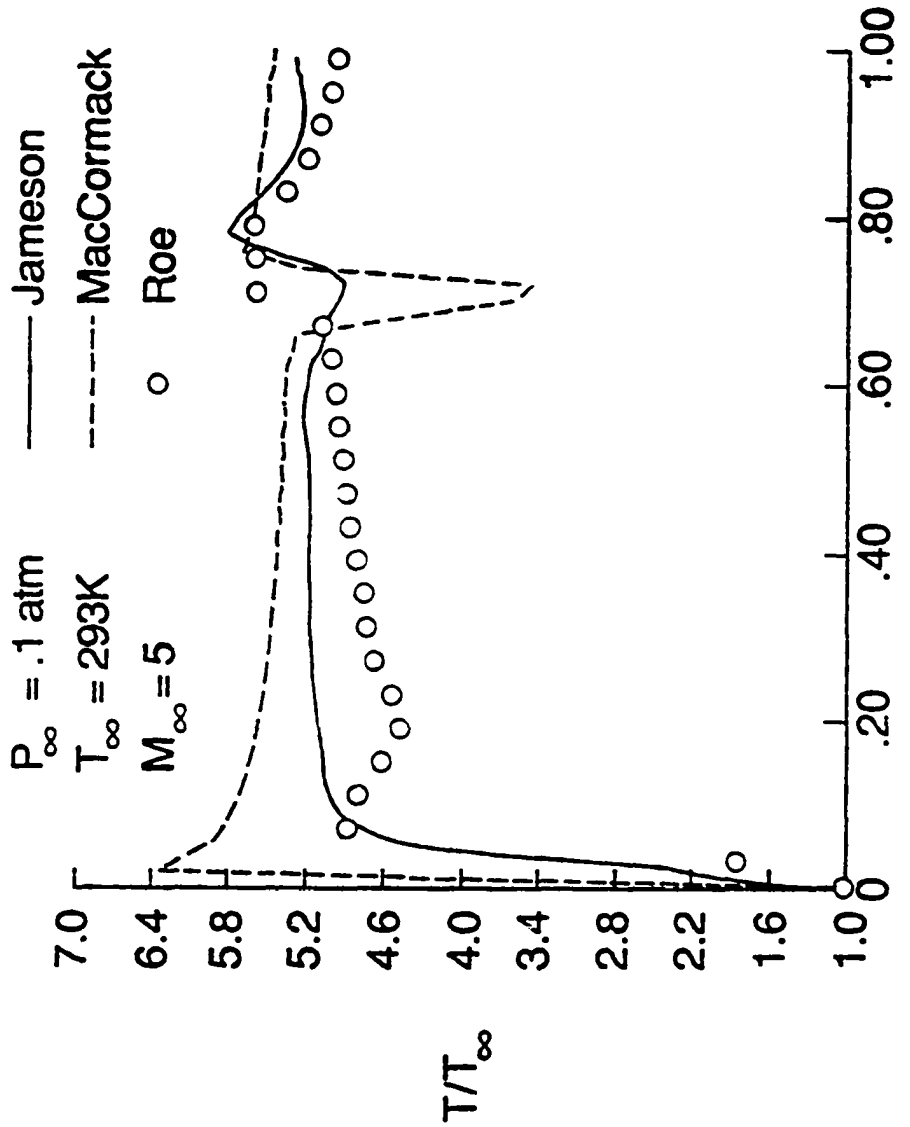

Fig. 5.31 Temperature variation with x for viscous flow ($H_w = H_\infty$, J = 50).

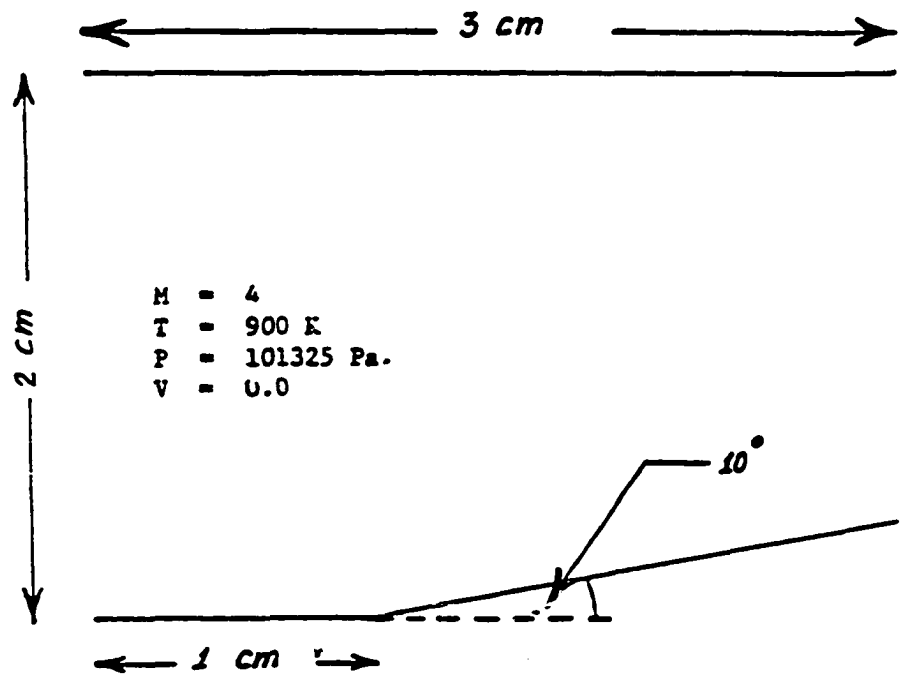

Fig. 5.32 Geometry and flow conditions for chemically reacting and radiating flow case.

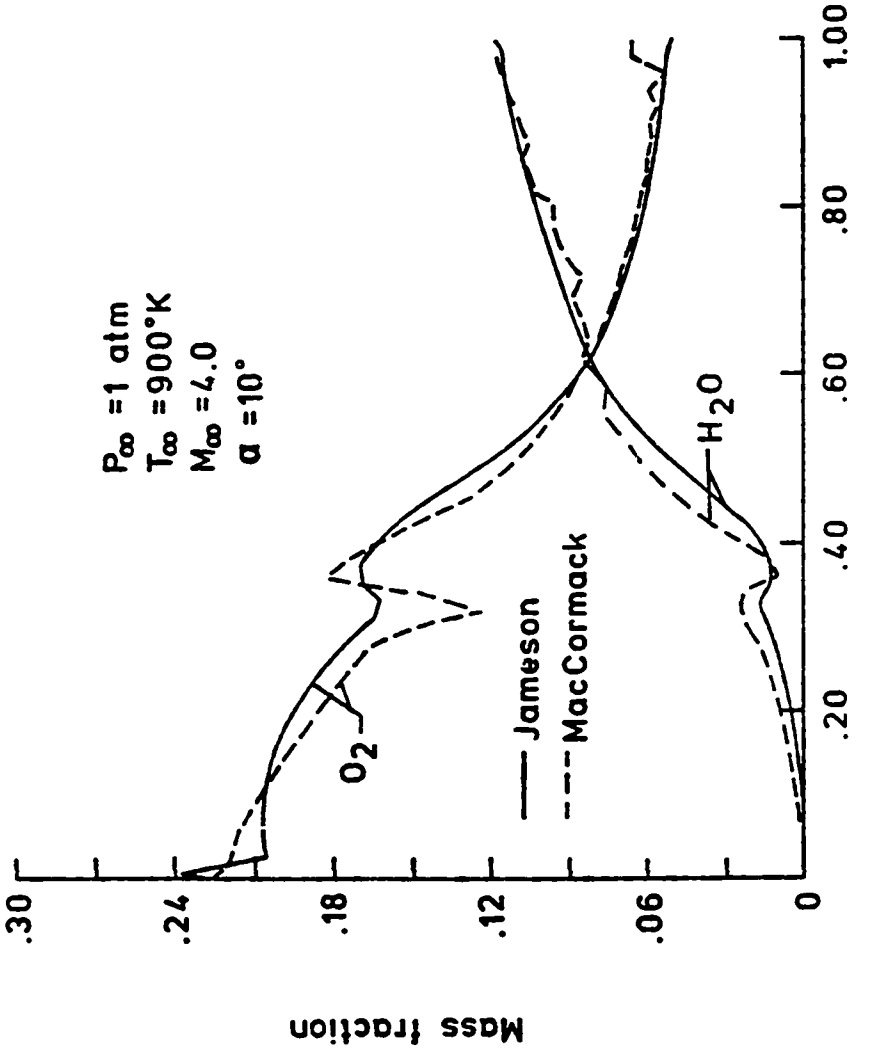

Fig. 5.33 Distribution of H_2O and O_2 mass fraction along the channel (J = 5).

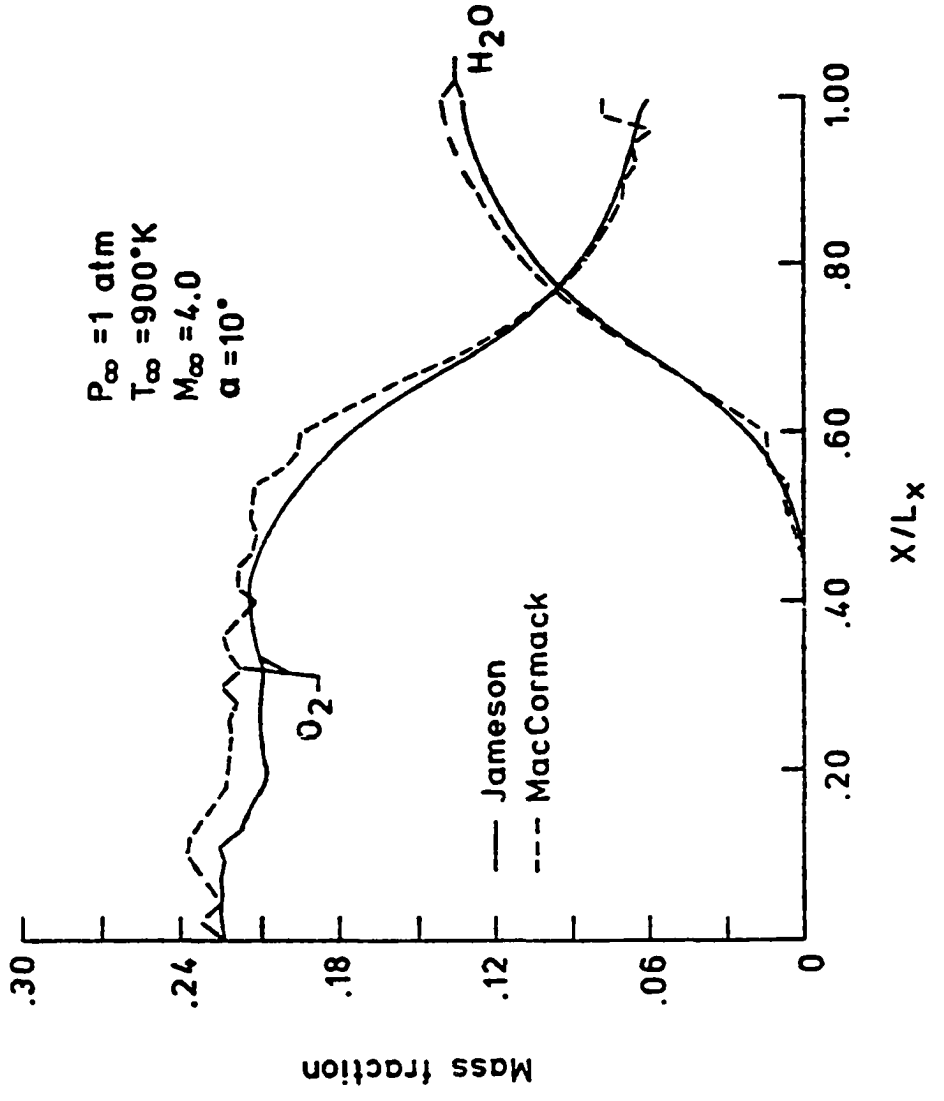

Fig. 5.34 Distribution of H_2O and O_2 mass fraction along the channel (J = 10).

reasonable to assume that radiative heat transfer is negligable in flow direction. However, in general, this is not the case because the global gradient of the temperature has a significant effect on the radiative flux. Three different geometries are employed for various parametric studies. One is a channel with two parallel plates a distance L apart (Fig. 3.2); the other is a channel with a ten degree compression-expansion ramp at the lower boundary (Fig. 5.1). The third geometry is a channel with a compression corner at the lower boundary (Fig. 5.32). For the temperature range expected in the scramjet combustor, the important radiating species are OH and H_2O. The spectral information and correlation quantities needed for these species are obtained from Ref. 20. Both reacting and nonreacting flows are considered. Results for the nonreacting, one-dimensional radiative transfer are presented in Figs. 5.35-5.38. Completed information on one-dimensional radiative transfer with chemical reaction is provided in Ref. 43. Selected results of the one-dimensional radiative transfer analysis are discussed here briefly.

For the parallel plate case (3 cm x10 cm), the inflow conditions are P_∞ = 1 atm, T_∞ = 1700K, M_∞ = 3.0, and f_{H_2O} = 0.5, f_{O_2} = .1 and f_{N_2} = 0.4. Results for the radiative flux, as a function of the nondimensional location along the flow, are illustrated in Fig. 5.35 for various distances from the lower plate. It is noted that the radiation flux is approximately zero in the center of the channel (y = 1.5 cm) and is significantly higher towards the top and bottom of the plates. This, however, would be expected because of the symmetry of the problem and the relatively higher temperature near the boundaries. The variations in the radiative flux are due to the leading edge shock interaction with the boundaries.

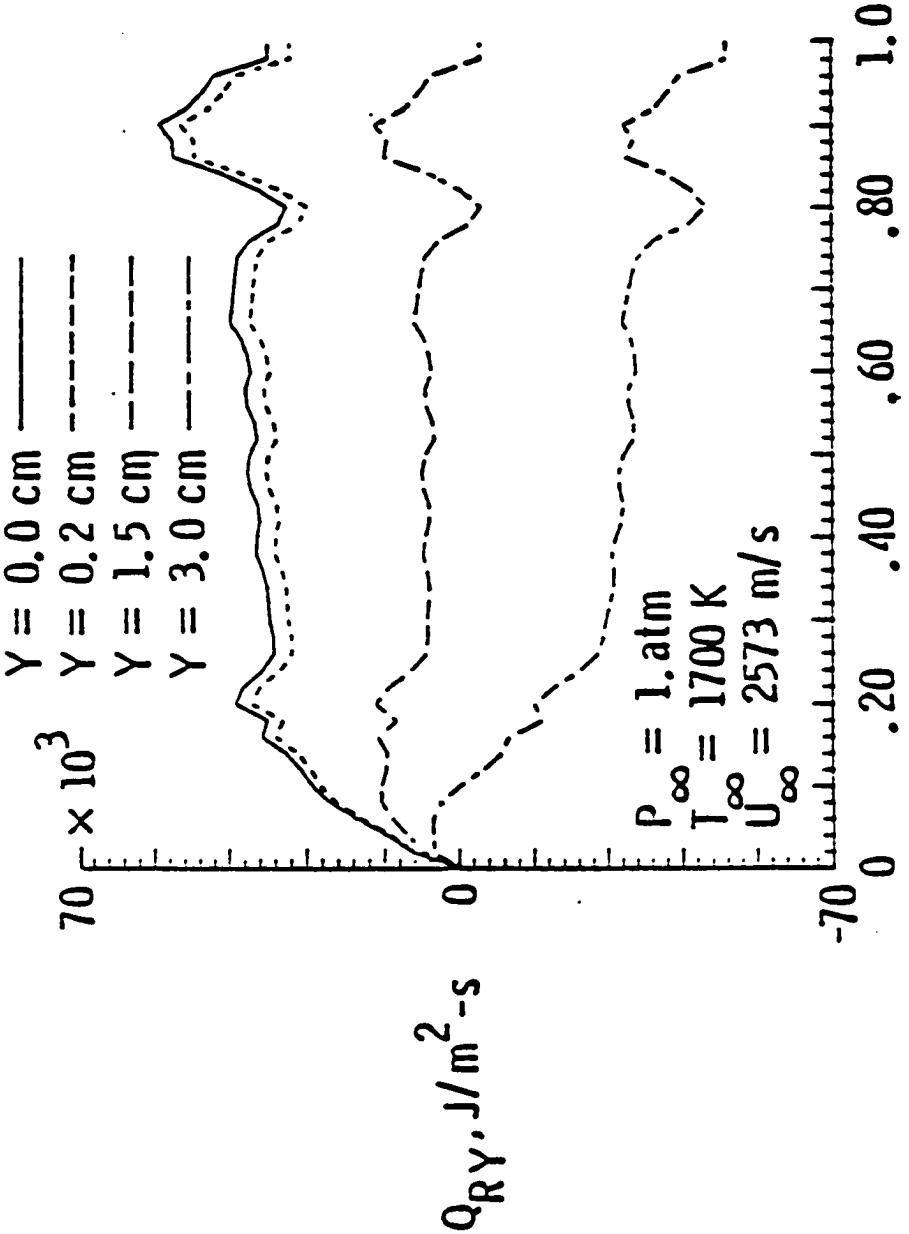

Fig. 5.35 Radiative flux along the channel for 50% H_2O.

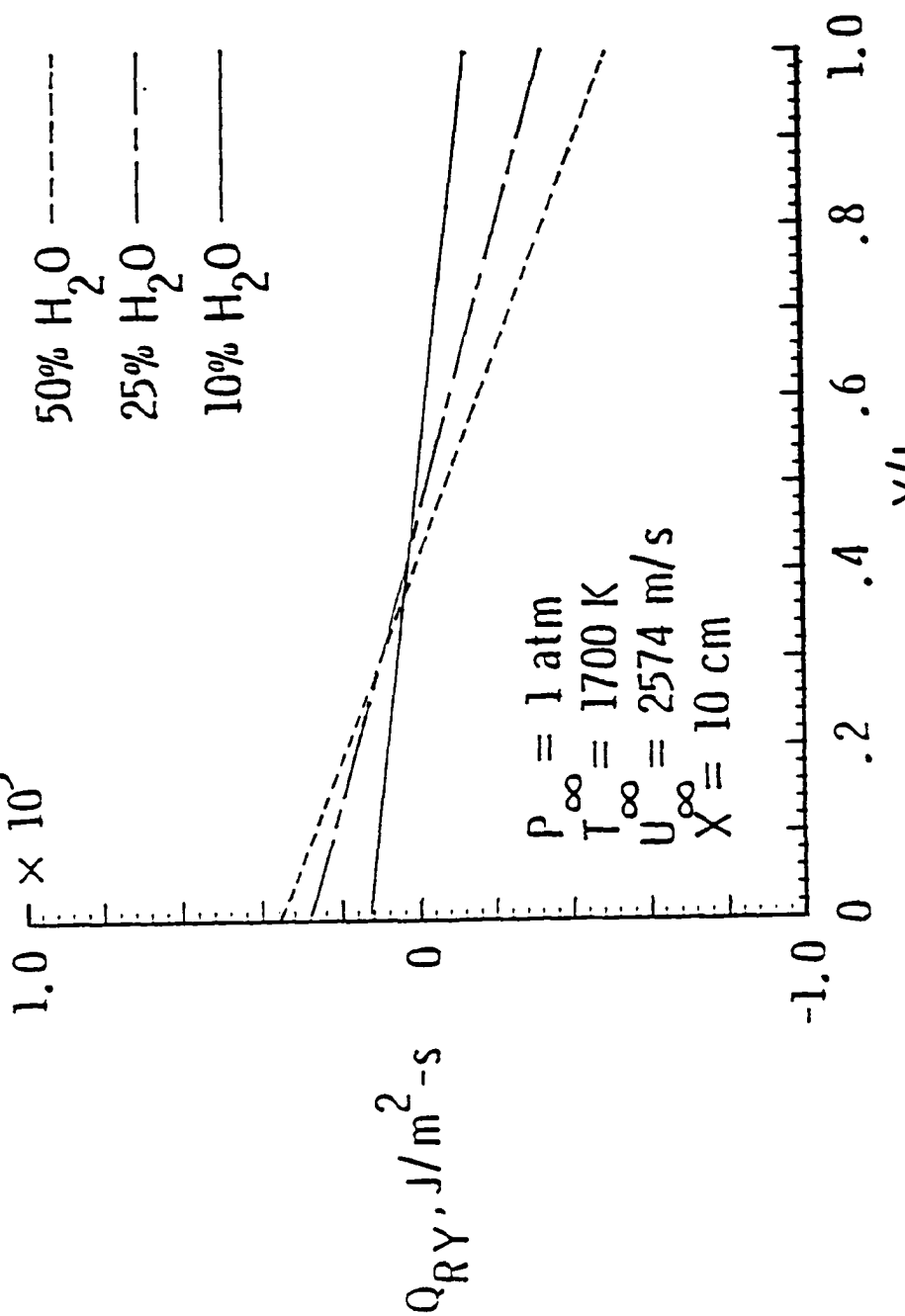

Fig. 5.36 Radiative flux vs. y at the channel exit.

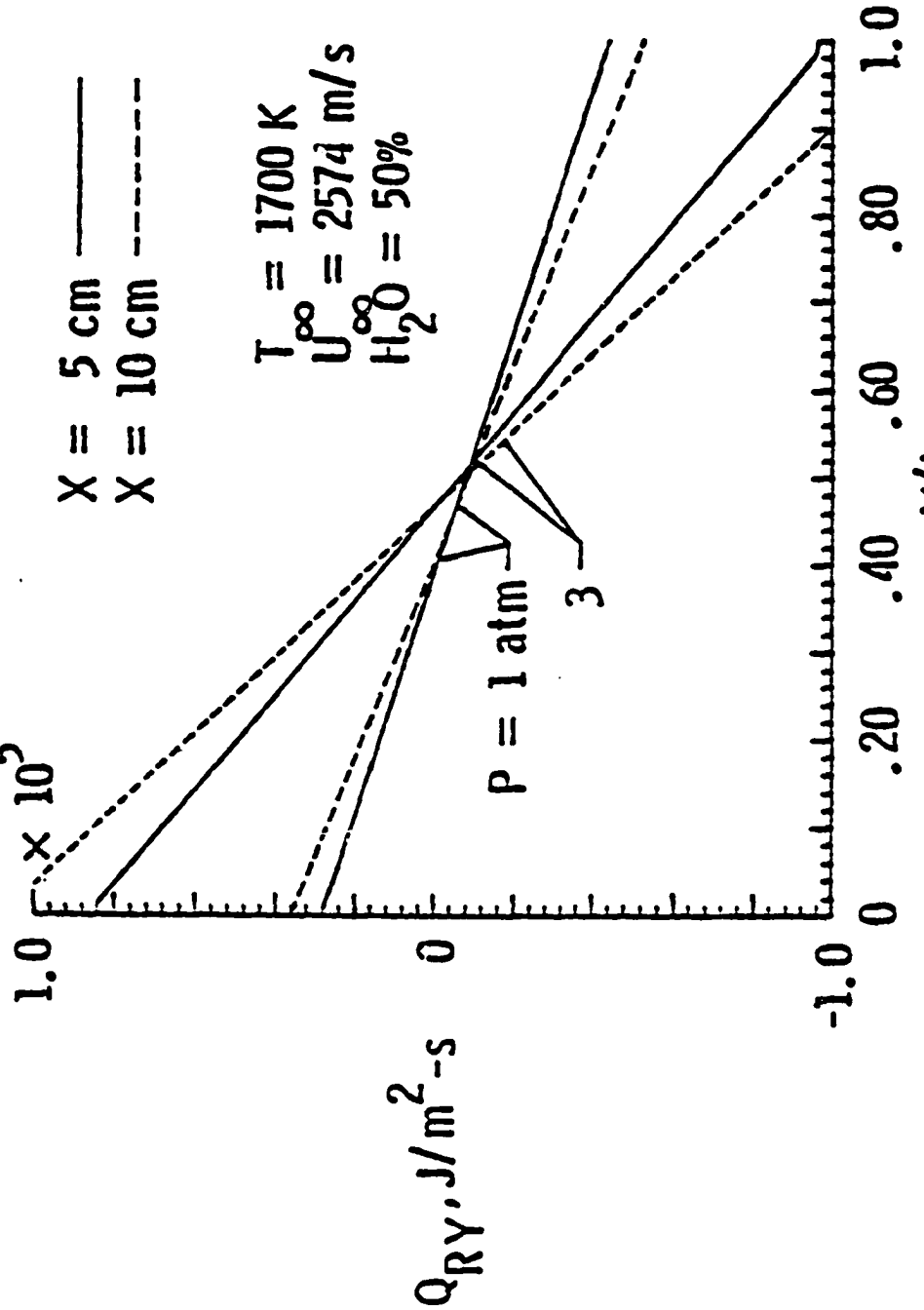

Fig. 5.37 Radiative flux vs. y at x = 5 and 10 cm.

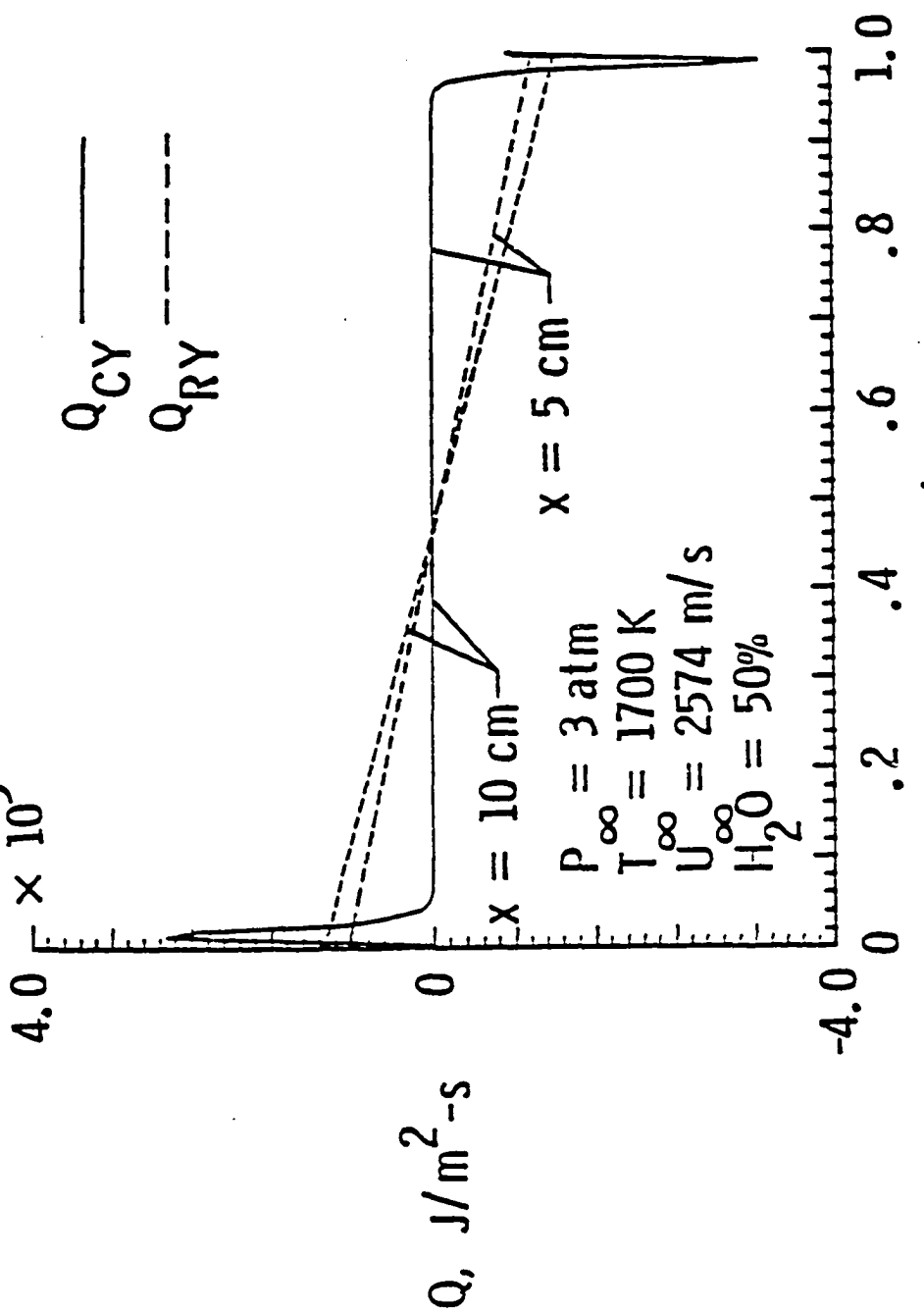

Fig. 5.38 Radiative conductive flux vs. y at x = 5 and 10 cm.

The results for radiative flux are illustrated in Figs. 5.36 and 5.37 as a function of the nondimensional y-coordinate. For P = 1 atm, the results presented in Fig. 5.36 for different water vapor concentrations indicate that the radiative interaction increases slowly with an increase in the amount of the gas. The results for 50% H_2O are illustrated in Fig. 5.37 for two different pressures (P_∞ = 1 and 3 atm) and x-locations (x = 5 and 10 cm). It is noted that the increase in pressure has dramatic effects on the radiative interaction. The conduction and radiation heat transfer results are compared in Fig. 5.38 for P = 3 atm and for two different x-locations (x = 5 and 10 cm). The results demonstrate that the conduction heat transfer is restricted to the region near the boundaries and does not change significantly from one x-location to another. The radiative interaction, however, is seen to be important everywhere in the channel, and this can have an influence on the entire flowfield. The results presented in Figs. 5.36-5.38 should be physically symmetric, but due to the predictor-corrector procedure used in the MacCormack's scheme, they exhibit some unsymmetrical behavior.

For the parallel plate geometry, a comparison of the divergence of radiatve flux for general (nongray), gray and their optically thin limit models is presented in Fig. 5.39 for two different y-locations (y = 0.2 and 1.5 cm). The inflow conditions are P_∞ = 1 atm, T_∞ = 1700K, M_∞ = 4.3. The gray gas formulation is based on the planck mean absorption coefficient which accounts for the detailed information on different molecular bands. As such, this approach is referred to as the "pseudo-gray formulation." The magnitude of optical thickness calculated for this case ($0.003 < \tau < 0.4$) shows that the radiation

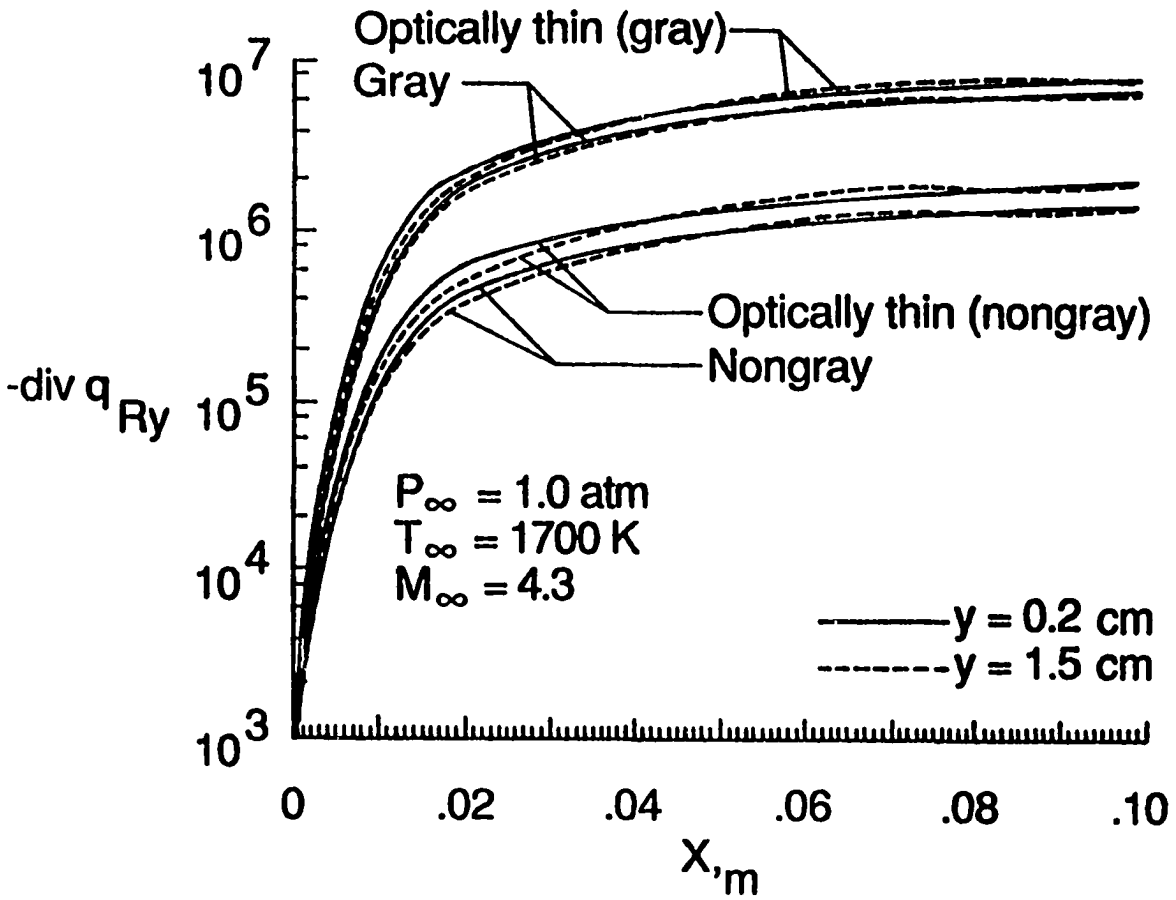

Fig. 5.39 Divergence of radiative flux along the channel for gray and nongray models.

regime is in the optically thin limit. The gray, nongray, and optically thin limit formulation are employed, and results confirm that the radiation regime is in the optically thin limit. For the physical conditions of the problem, no significant difference in results is observed for the two y-locations. The solution of the gray formulation in ODE form proves to be about ten times more efficient than the solution of the general formulation on the vector processing computer (the gray formulation uses 0.056 CRU's per iteration, while the general formulation uses 0.57 CRU's per iteration). The optically thin formulation is slightly more efficient than the gray formulation. All other results presented in this study have been obtained by using the pseudo gray gas formulation.

To investigate the effects of radiative energy tranfer in chemically reacting flows, premixed hydrogen and air with an equivalence ratio of unity was selected. Specific results are obtained for one- and two-dimensional radiative transfer with the physical geometry of Figs. 5.1 and 5.32, respectively. For the one-dimensional radiative transfer, the inlet conditions considered are P_∞ = 1 atm, T_∞ = 1700, M_∞ = 4.5. For the physical conditions of the problem, the radiation participating species produced due to the chemical reaction essentially are OH and H_2O. The radiative interaction is started at about X/L_X = 0.20 to make sure that there are significant amounts of OH and H_2O produced by the reaction for active participation. This restriction was removed later and radiative interactions start at the inlet for the remaining results. The pressure contours for the flow without and with chemical reaction are shown in Figs. 5.40 and 5.41. A comparison of the pressure contours shows that the shock angle has increased in the case of the

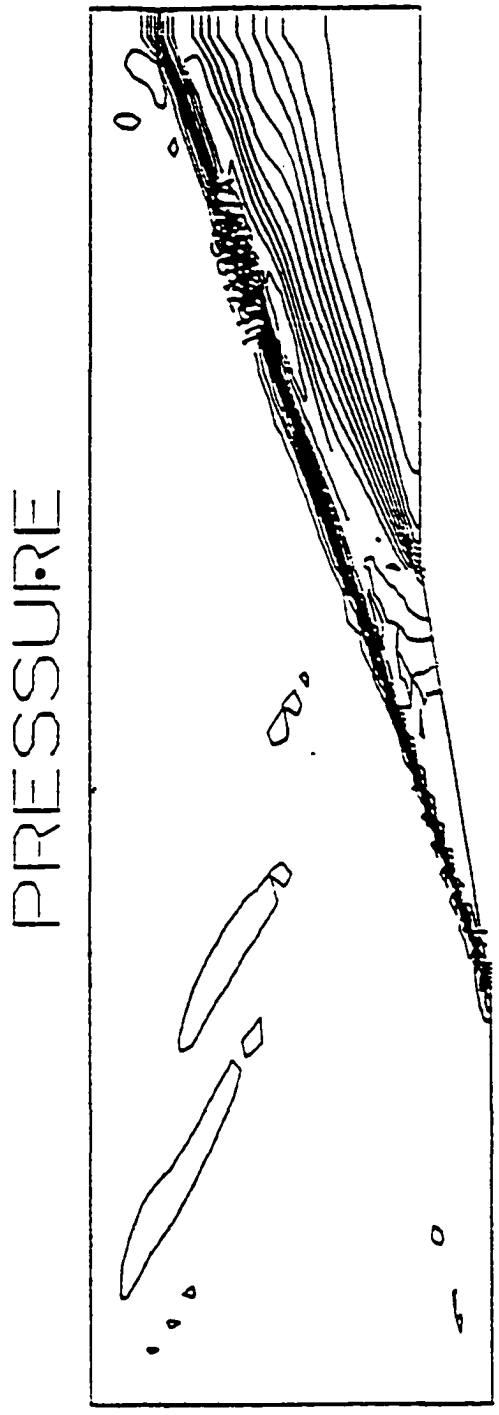

Fig. 5.40 Pressure contours for nonreacting flow in a channel with a ramp.

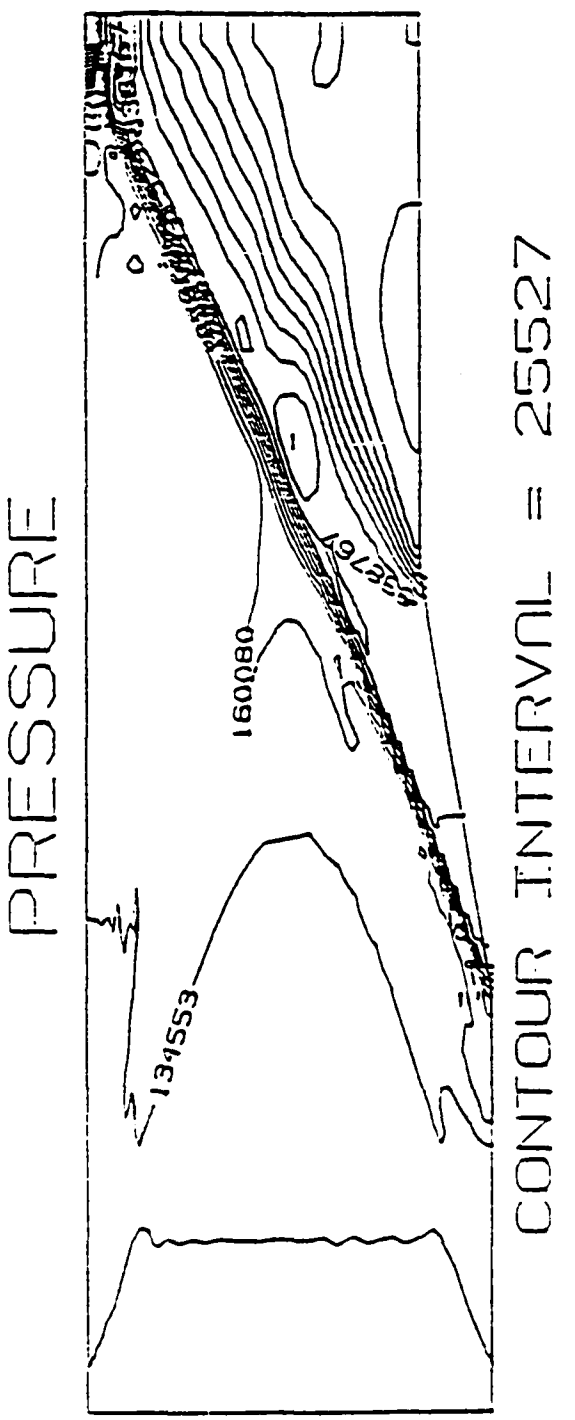

Fig. 5.41 Pressure contours for reacting flow in a channel with a ramp.

reacting flow. This is due to a relatively thicker boundary layer and changes in the thermophysical properties of the mixture.

The variations in species concentration along the channel are illustrated in Fig. 5.42 for chemically reacting, and chemically and radiating flows. It is found that due to the radiative interaction, the concentration of OH increases by about five percent and the concentration of H_2O decreases by the same amount. It should be noted that the radiative interaction has no significant effect on O_2 and H_2. The effect of radiatve heat transfer on the temperature is almost negligible.

The effects of two-dimensional radiative transfer in chemically reacting flows was investigated for the physical problem of Fig. 5.32. Premixed hydrogen and air with an equivalence ratio of unity, and inlet conditions of $P_\infty = 1$ atm, $T_\infty = 900$ K, $M_\infty = 4.0$ were selected. Figures 5.43-5.46 are the contour plots of the reactants and products. As expected, the destruction and production of the species occurred only in the boundary layers and after the shock, where the temperature is greater than 1000 °K. Figures 5.47 and 5.48 are contour plots of the pressure without and with chemical reaction. It should be observed that the compression shock is curved when chemical reaction takes place. A series of shock waves is created due to the pressure increase caused by a sudden heat release from chemical reaction. Interaction of these shock waves with compression shocks increases the shock strength, and this causes the shock to curve.

Figure 5.49 illustrates the variation of nondimensional y-radiative flux for several locations across the channel. The radiative flux in

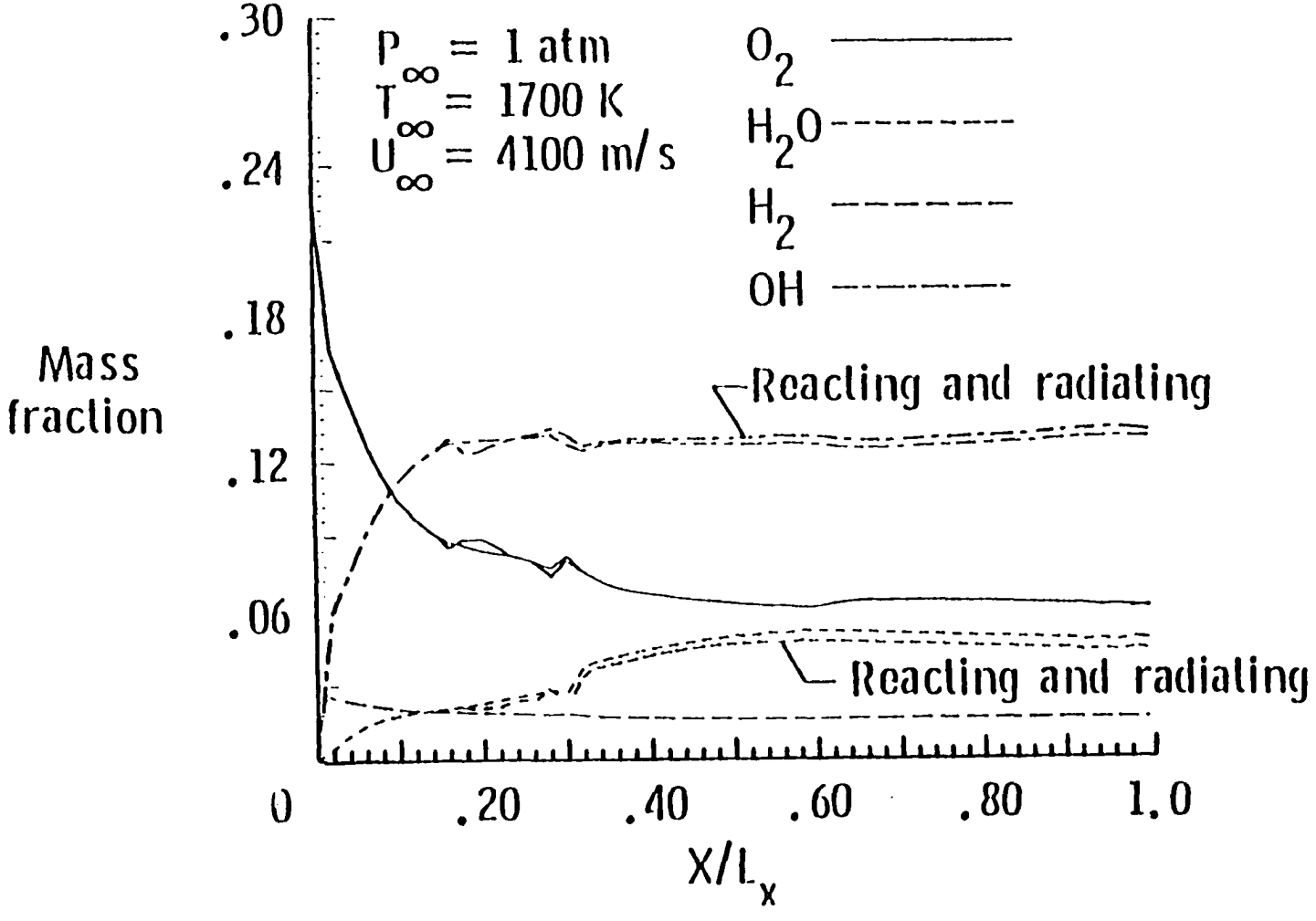

Fig. 5.42 Distribution of species mass fraction along the channel for reacting, and reacting and radiating flows.

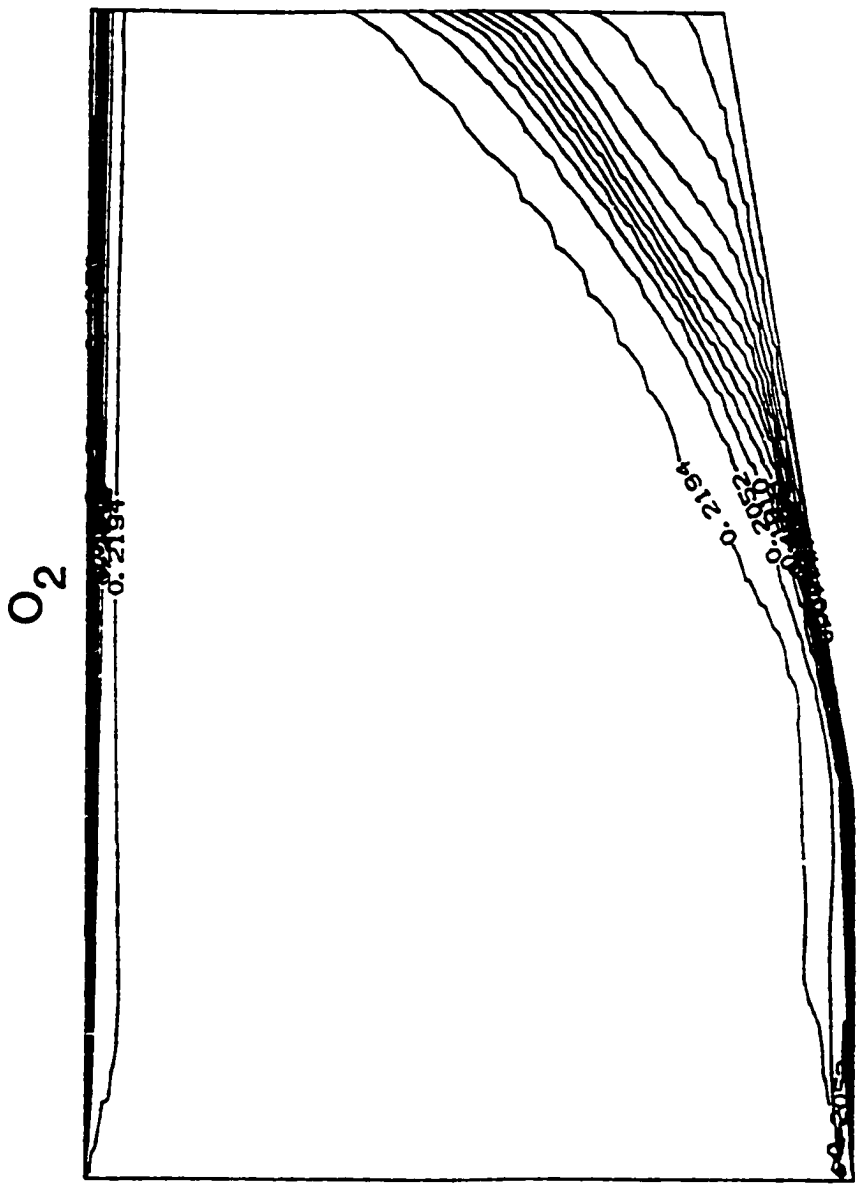

Fig. 5.43 O_2 contours for reacting and radiating flow in a channel with a compression corner.

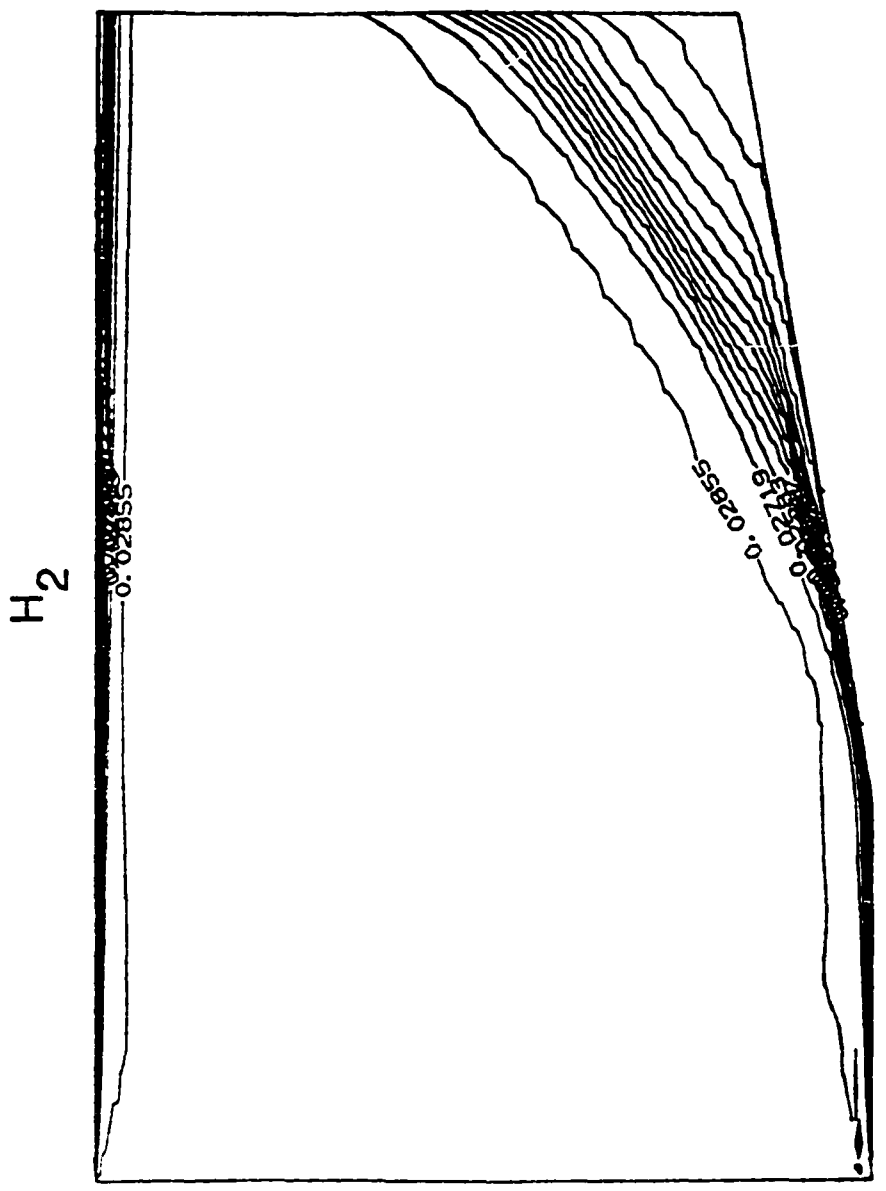

Fig. 5.44 H_2 contours for reacting and radiating flow in a channel with a compression corner.

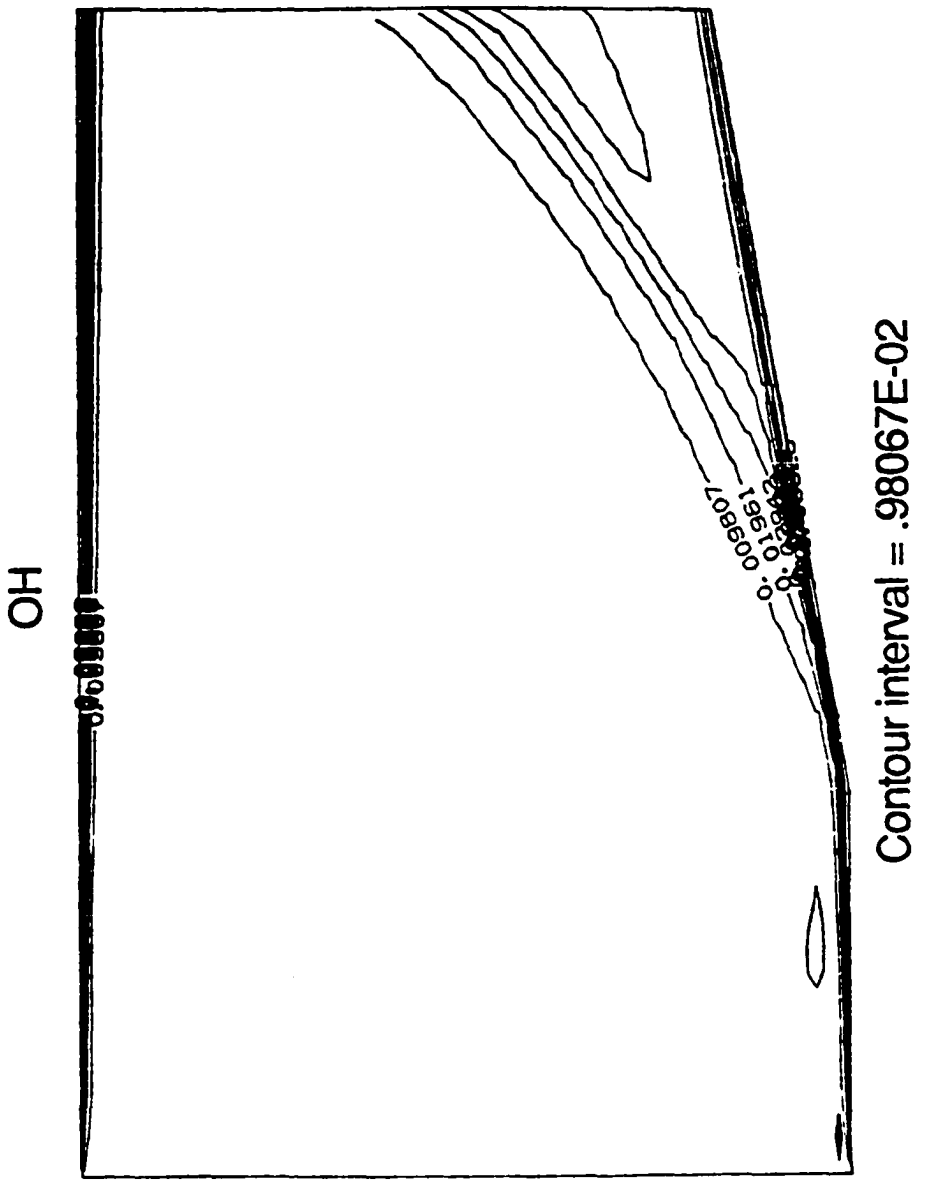

Fig. 5.45 OH contours for reacting and radiating flow in a channel with a compression corner.

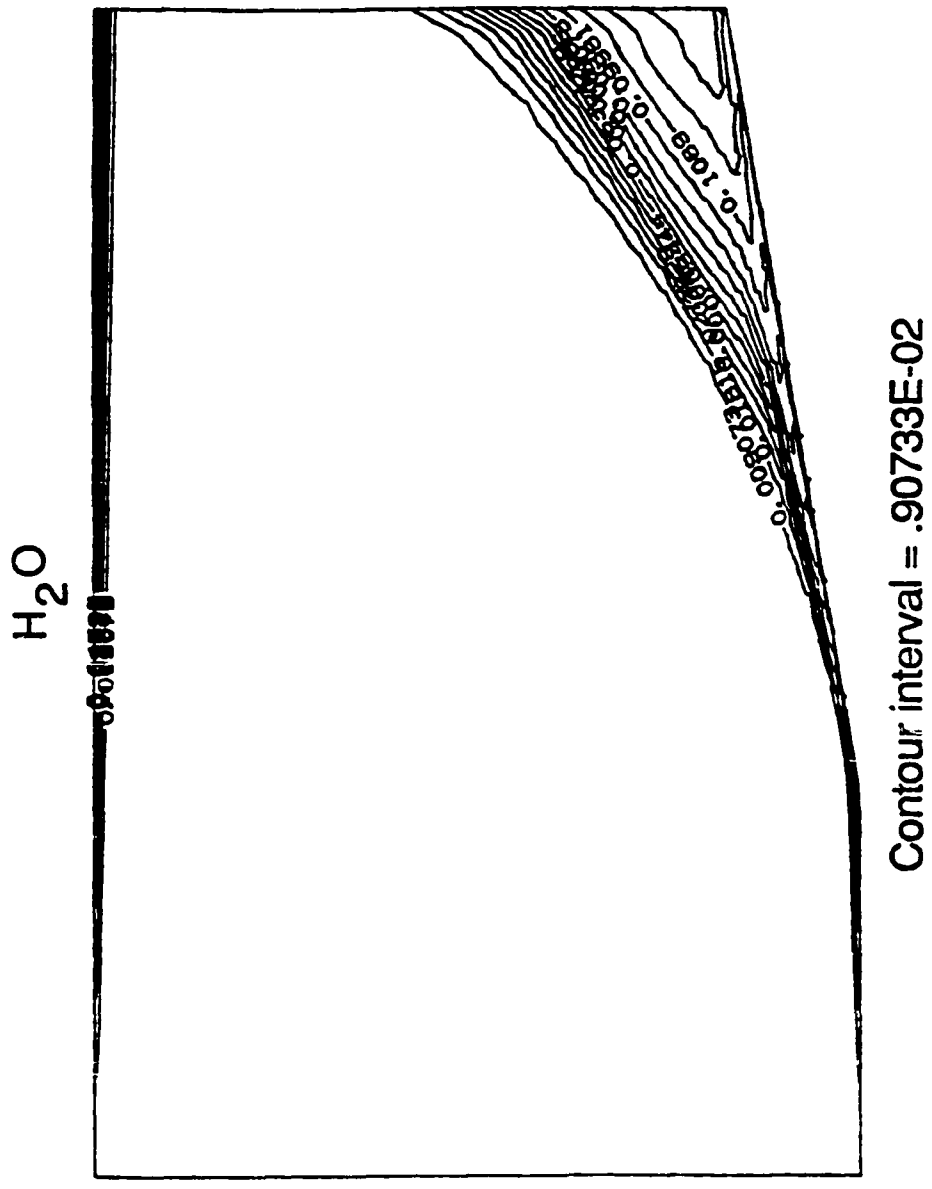

Fig. 5.46 H_2O contours for reacting and radiating flow in a channel with a compression corner.

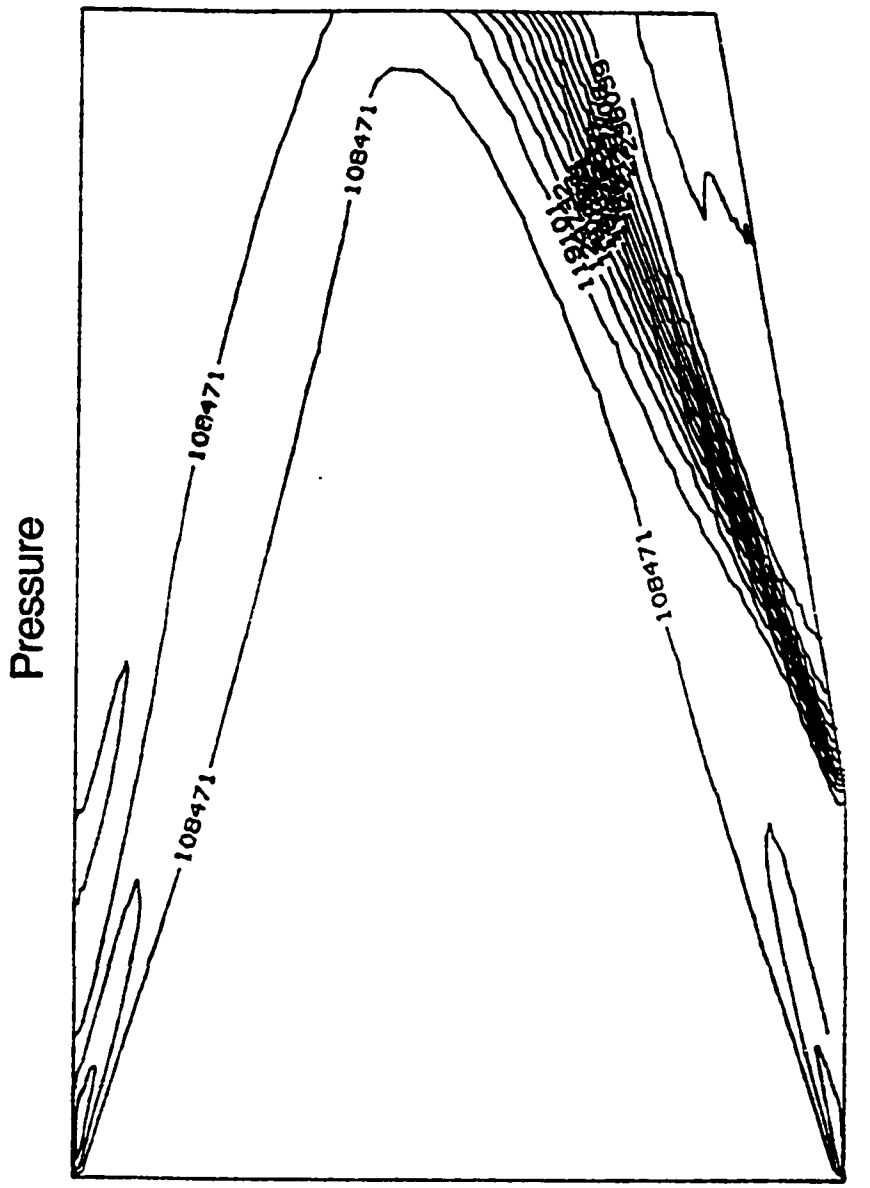

Fig. 5.47 Pressure contours for nonreacting and nonradiating flow in a channel with a compression corner.

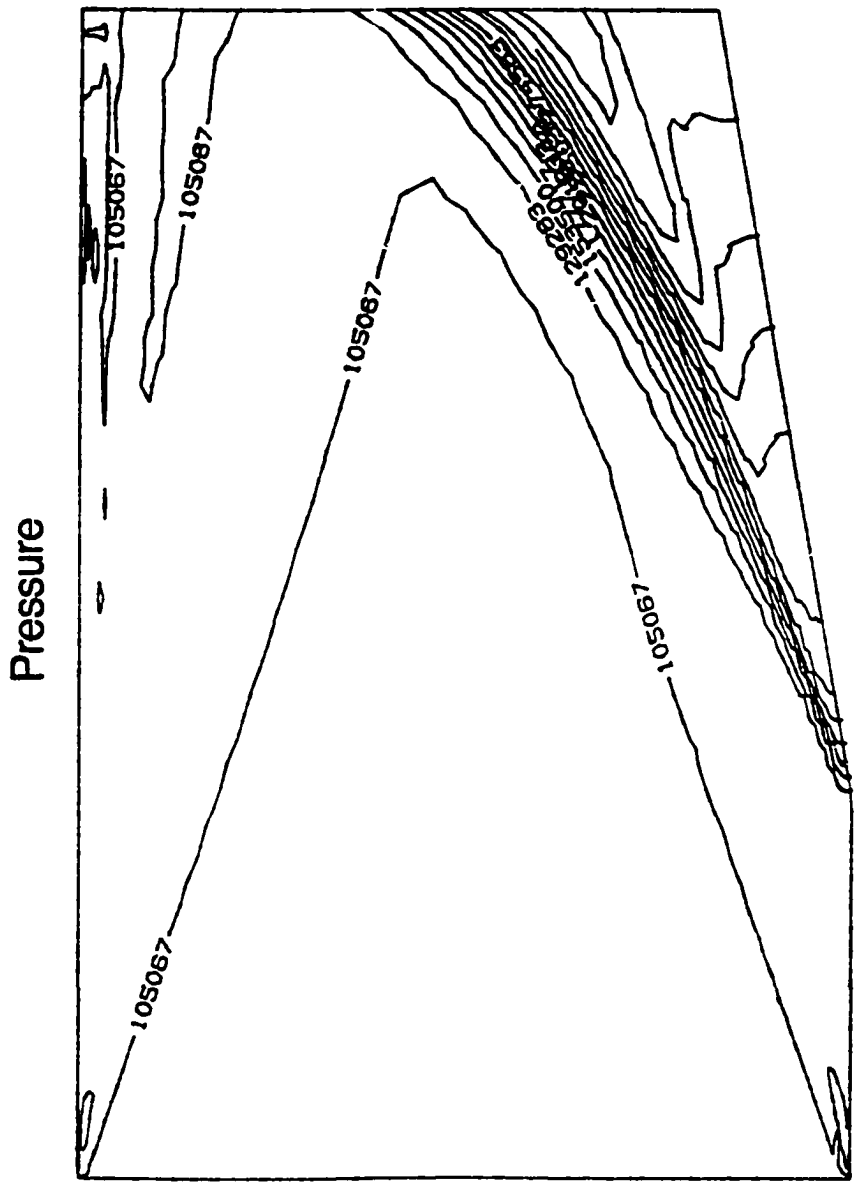

Fig. 5.48 Pressure contours for reacting and radiating flow in a channel with a compression corner.

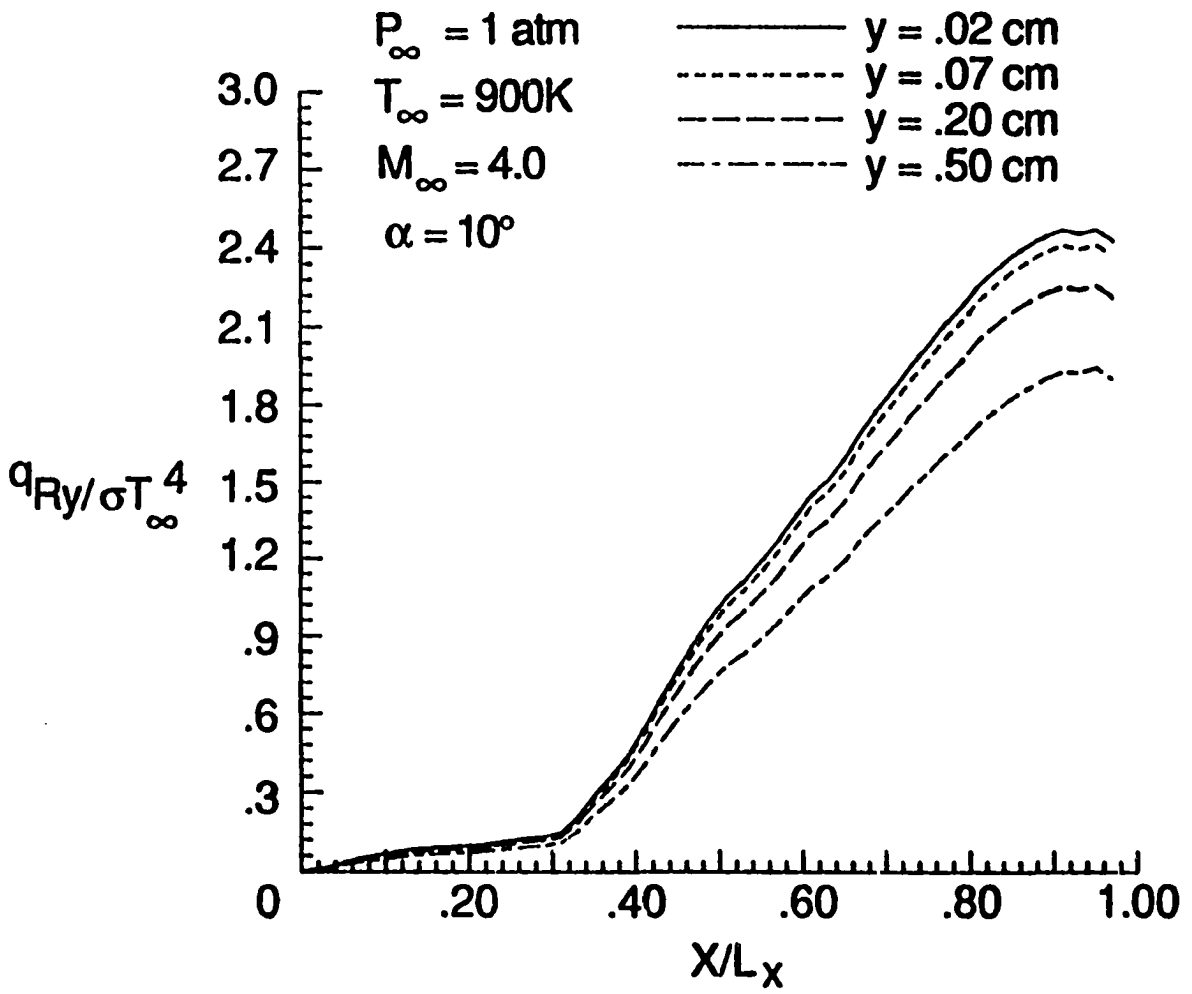

Fig. 5.49 Variation of normal radiative flux with x for a channel with 10° compression corner (M = 4).

the y-direction is neglegible before the shock; this is due to the almost symmetrical condition and lower pressure and temperature. The radiative flux substantially increases after the shock due to the increase in participating species, pressure, and temperature. Radiative flux decreases away from the lower boundary due to the reduction in temperature. The radiative flux in a streamwise direction is illustrated in Fig. 5.50. It peaks at a short distance from the boundary and then gradually decreases toward the center of the channel. The peak is due to the pressure gradient caused by the leading edge bow-shock. The radiative flux (q_{Rx}) remains constant in the region with no chemical reaction, and gradually decreases in the region with chemical reaction. The reduction in q_{Rx} is caused by cancellation of fluxes in positive and negative directions.

Figures 5.51 and 5.52 illustrate the radiative flux for the same inlet conditions as in Fig. 5.32 but for the 15^0 compression corner. Comparing the results of Figs. 5.49 and 5.51, it is noted that, due to the increase of shock strength, the radiative flux in y-direction has a steep gradient through the shock. After the shock, it gradually decreases as some of the radiative flux from lower boundary gets canceled from the radiative flux of the upper boundary layer. Figure 5.52 is the illustration of the streamwise flux along the channel for several locations across the channel. Comparing the results with the results of Fig. 5.50, it is noted that the radiative flux increases considerably with increasing the shock angle.

Figures. 5.53 and 5.54 illustrate similar results as presented in Figs. 5.49 and 5.50 for the same freestream conditions but for $M_\infty = 6$. By increasing the Mach number the shock angle decreases. As a result,

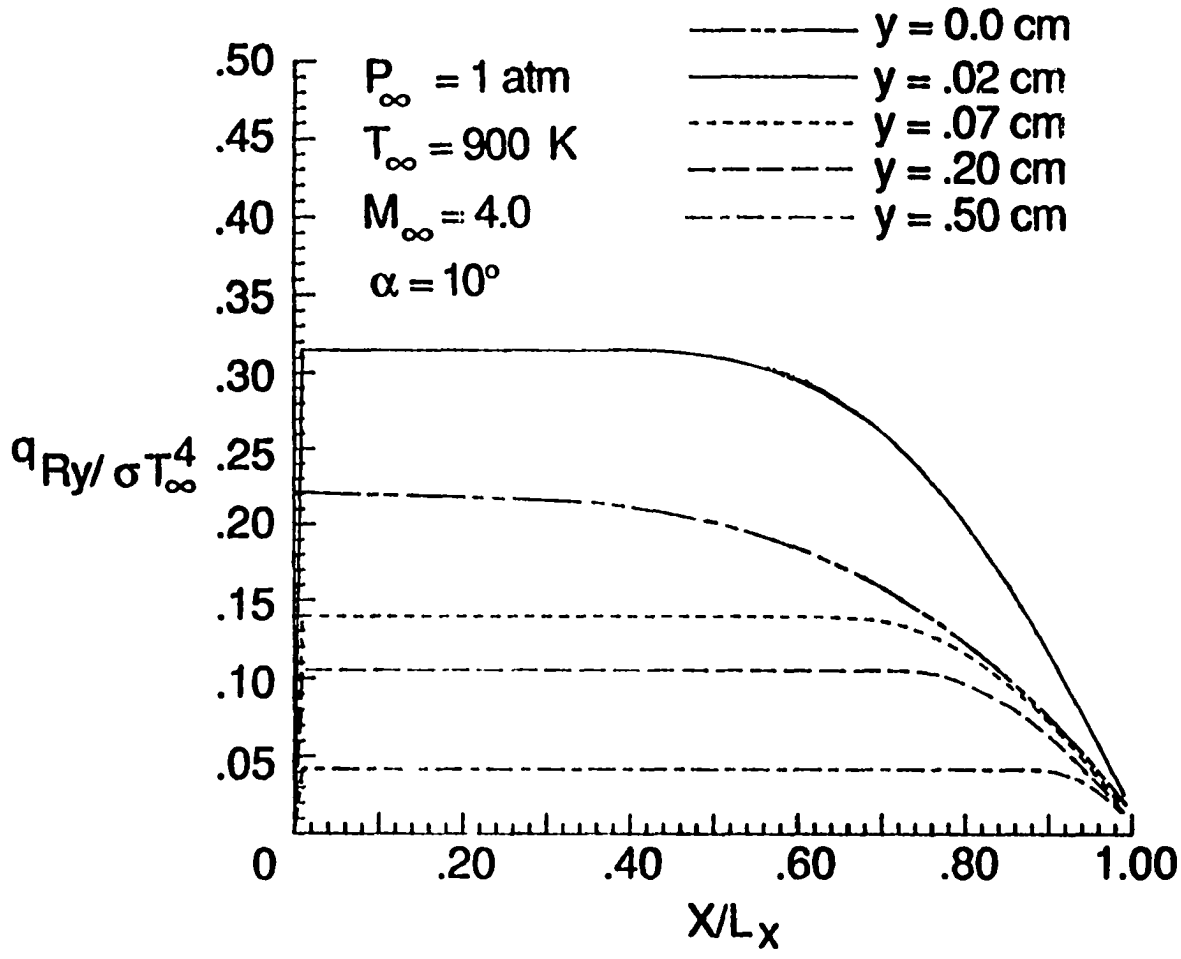

Fig. 5.50 Variation of streamwise radiative flux with x channel with 10° compression corner (M = 4).

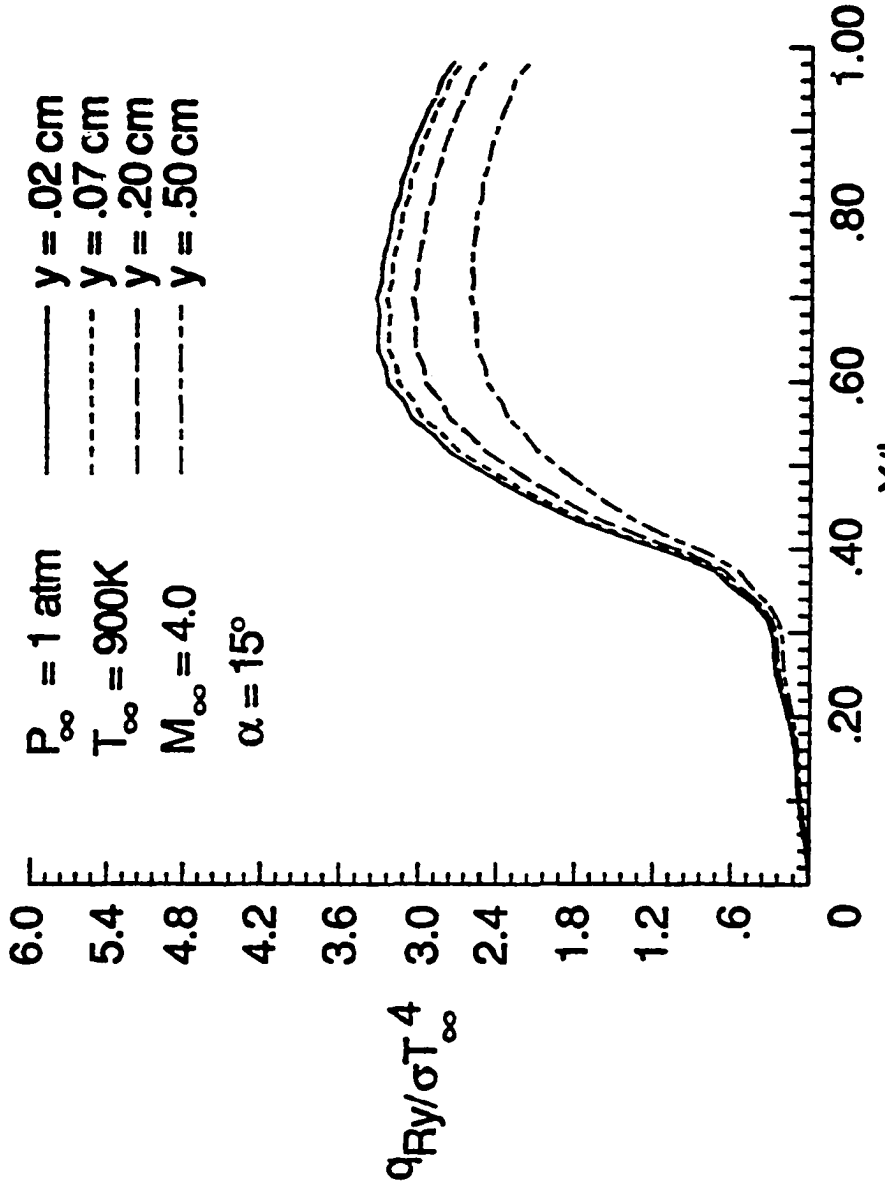

Fig. 5.51 Variation of normal radiative flux with x in a channel with 15° compression corner (M = 4).

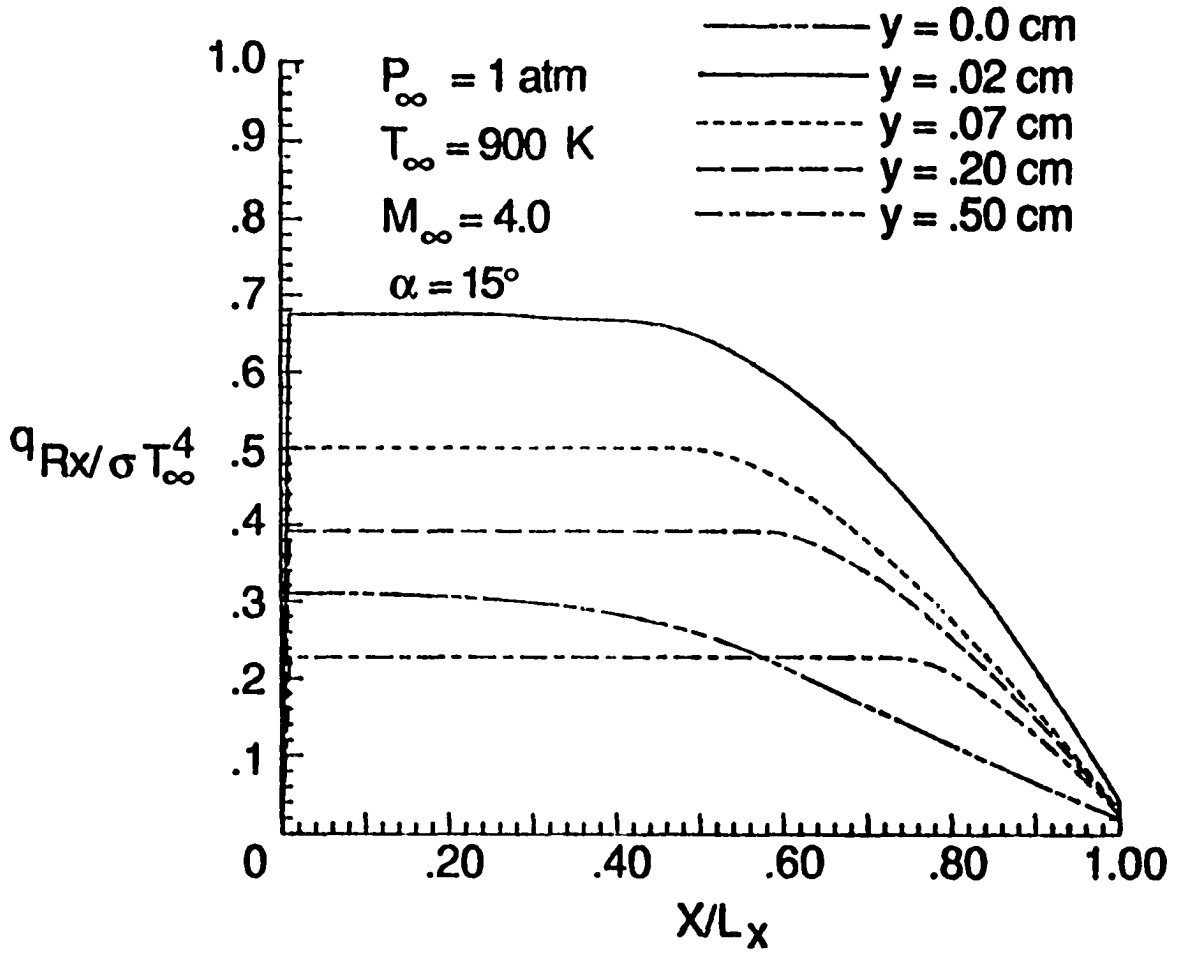

Fig. 5.52 Variation of streamwise radiative flux with x in a channel with 15° compression corner (M = 4)

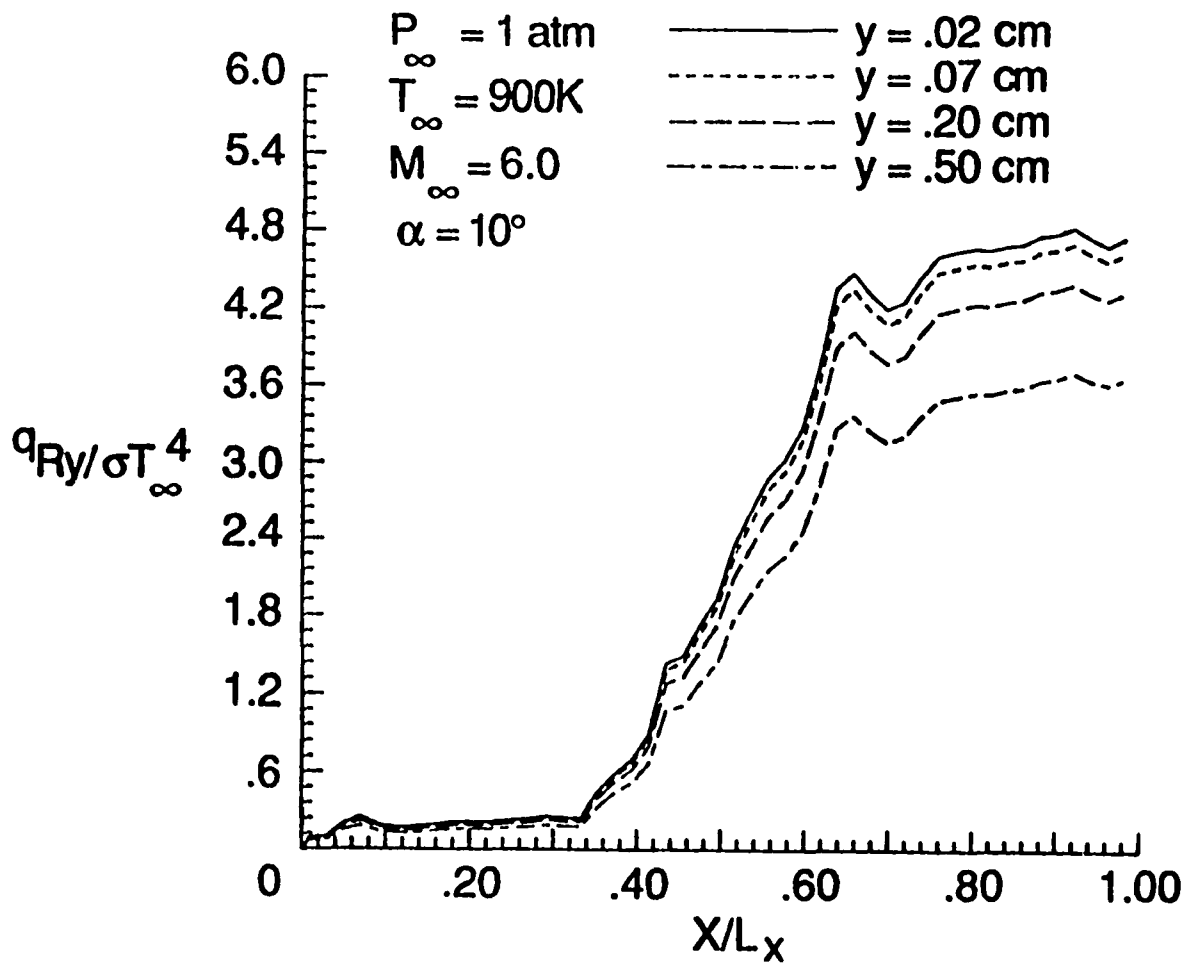

Fig. 5.53 Variation of normal radiative flux with x in a channel with 10° compression corner (M = 6).

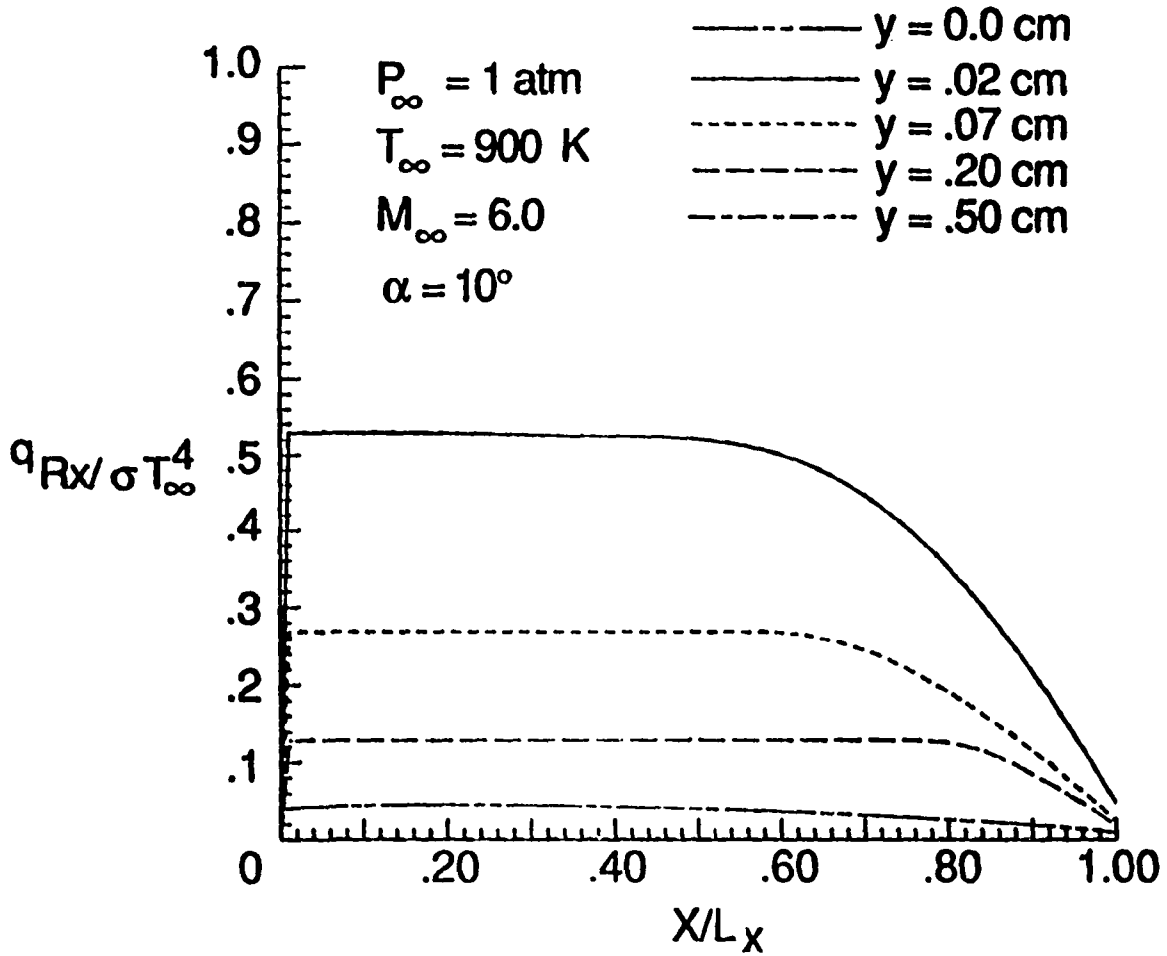

Fig. 5.54 Variation of streamwise radiative flux with x in a channel with 10° compression corner (M = 6).

there is no chemical reaction at y = 0.5 cm. Therefore, streamwise radiative flux at this location reduces to zero. It is noted that the radiative flux increases substantially by increasing the Mach number.

Figure 5.55 illustrates the variations in species mass fraction for two locations (y = 0.02 and 0.2 cm) across the channel. At y = 0.02 cm, where the value of total energy is reduced by the q_{Rx} (q_{Rx} direction is from outlet to inlet), less H_2O is produced. After the shock, more H_2O has been produced, for both locations because the total energy is increased by q_{Ry}. It should also be noted that at locations where the total energy is reduced less of the reactant (O_2) is used (Fig. 5.56). The temperature variation for chemically reacting, and reacting and radiating flows along the channel are illustrated for two locations (y = 0.02 and 0.2 cm) in Fig. 5.57. At location y = 0.02, where the value of q_{Rx} is greatest in comparison to the other locations, the temperature has been reduced. At y = 0.2, there is no change in the temperature before the shock because there are no paticipating species. After the shock, temperature has slightly increased over the nonradiating case; this is due to the contribution from q_{Ry}.

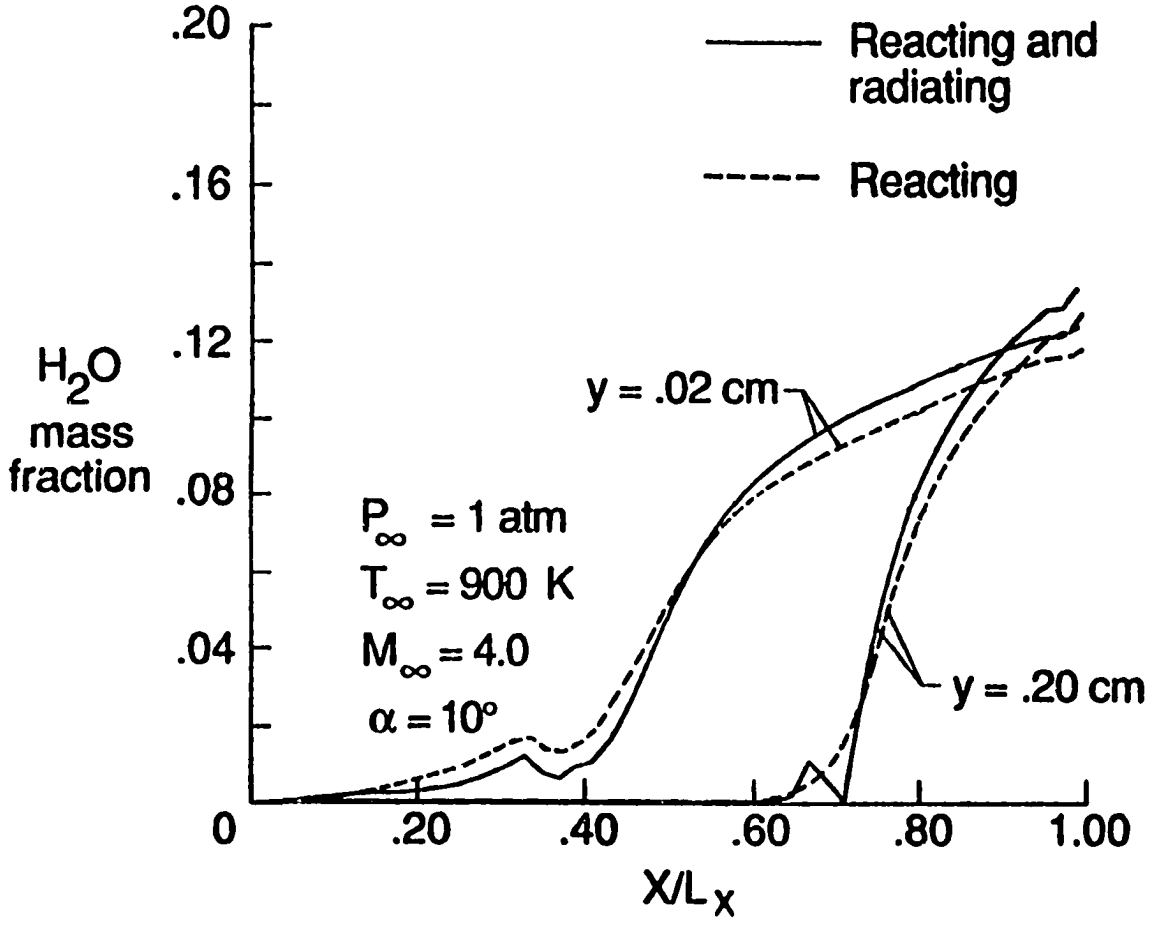

Fig. 5.55 Distribution of H_2O mass fraction along the channel for reacting and radiating, and reacting flow.

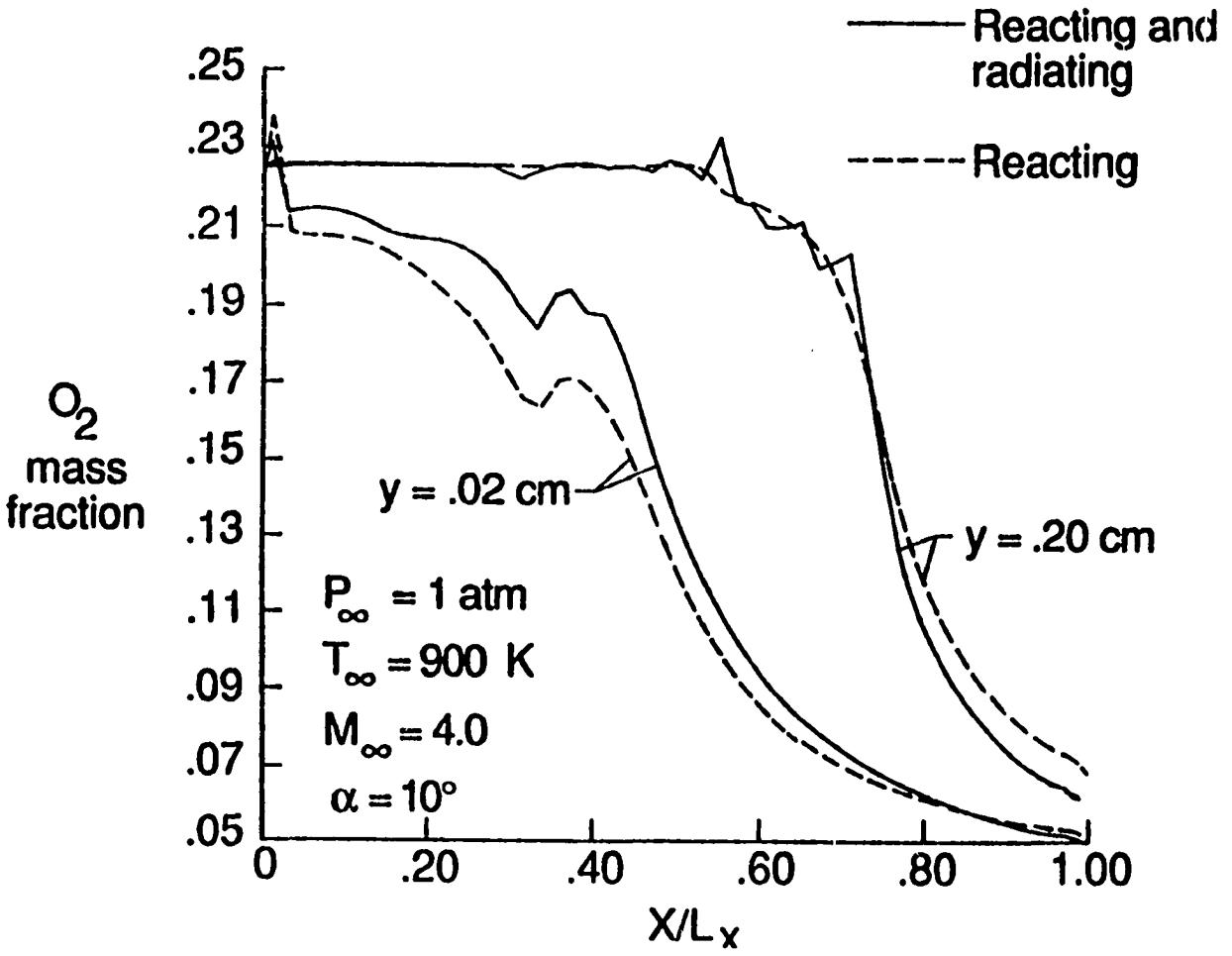

Fig. 5.56 Distribution of O_2 mass fraction along the channel for reacting and radiating, and reacting flow.

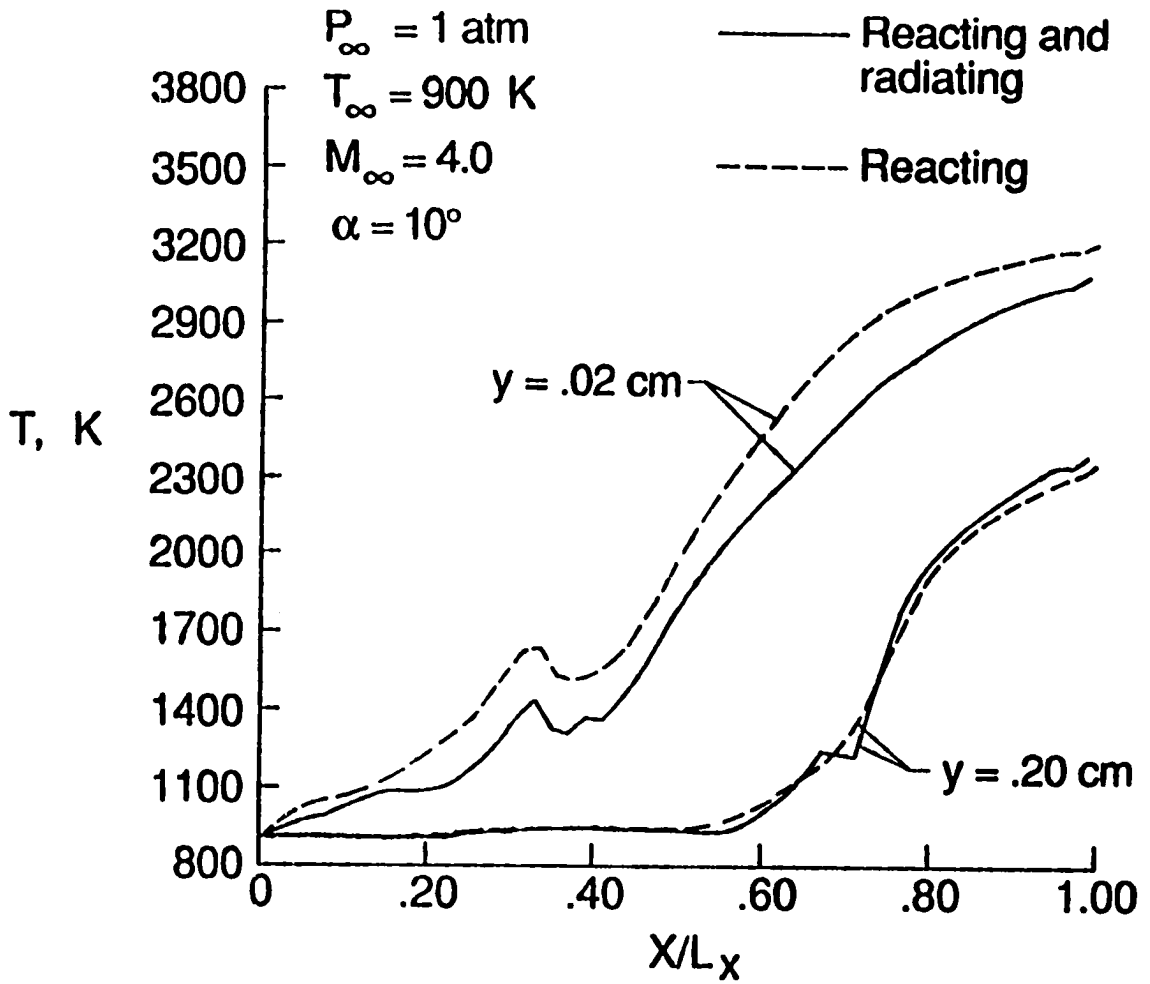

Fig. 5.57 Temperature variation with x for reacting and radiating, and reacting flow.

Chapter 6

CONCLUSIONS

Based on the theory and computational procedure that have been described, two algorithms were developed to solve the continuity, momentum, energy, and species continuity equations for nonreacting, reacting, radiating and reacting supersonic channel flows. The finite volume algorithm with the appropriate damping scheme proved to be accurate, non-oscillatory and robust for reacting and nonreacting, viscous and invsicid flows. The supersonic viscous and inviscid flows in a channel with ten degree compression-expansion ramps at the lower wall were solved by both the finite-volume and finite-difference schemes. The results of viscous flow were compared with the results of the upwind scheme of Roe. The finite-volume scheme required more grid points in the boundary layer and shocks than did the finite difference scheme. There is an excessive amount of artificial viscosity due to the highly stretched grid in the boundary layer, near high gradient regions (like compression or expansion corners). However, this problem can be alleviated by increasing the grid points in the high gradient regions in the flow directions.

The supersonic pre-mixed hydrogen-air flow with equivalence ratio of unity was solved by both finite difference and finite volume schemes in a channel with a ten degree compression corner. The flow was ignited by the shock wave from the compression corner. The results of finite

volume scheme compared very well with the results of the finite difference scheme. Finite volume scheme did not show the oscillation which was observed in the finite difference solution.

In the hypersonic propulsion system, the temperature ranges from one to five thousand degrees Kelvin. In this range, various nonsymmetric molecules become highly radiative participating. One-dimensional radiative flux was included in the energy equation for the solution of nonreacting supersonic flows between parallel plates. It was concluded that the radiative flux increases with the increase of pressure, temperature, and participating species. In the case of flow without chemical reaction, most of the energy transferred was by convection in the direction of flow. As a result, the radiative interaction did not affect the flow field significantly.

Finally, two-dimensional radiative interaction was investigated for supersonic chemically reacting flow in a channel with a compression corner. Some important results were obtained by considering the radiative flux in both directions. The results revealed that radiation can have a significant influence on the entire flow field; however, the influence is stronger in the boundary layers. It was found that due to the temperature increase by chemical reaction, radiatve transfer in the streamwise direction can have a significant effect on the flow field. Radiative heat transfer is a strong function of the pressure pathlength. By increasing the dimensions from the model geometry to physical geometry, pathlength and, therefore, radiative heat transfer will increase. It is concluded that radiative heat transfer in the hypersonic propulsion can have a significant effect on the entire flow field. It was also found that the numerical scheme based on the pseudo-

gray gas formulation for the radiative flux is highly efficient as compared to the scheme based on the nongray formulation, especially for the vector processing computers (over ten times). It is concluded that for the supersonic chemically reacting flows the radiation is in optically thin limit for the physical conditions considered in this study.

It is suggested that future study include grid adaption to the finite volume scheme for better shock resolution. For steady state solution, it is suggested that the multi grid and residual smoothing be used to speed up the convergence. The effect of radiative heat transfer in non-premixed chemically reacting flow should also be investigated.

REFERENCES

1. Kumar, A., "Numerical Analysis of a Scramjet Inlet Flow Field Using the Three-Dimensional Navier-Stokes Equations," presented at the 1983 JANAF Propulation Meeting, February 1983; also "Numerical Simulation of Scramjet Inlet Flow Field," NASA TP-2517, May 1986.

2. Drummond, J. P., Hussaini, M. Y. and Zang, T. A., "Spectral Methods for Modeling Supersonic Chemically Reacting Flow Fields," AIAA Journal, Vol. 24, No. 9, 1986, pp. 1461-1467.

3. Drummond, J. P., Rogers, R. C. and Hussaini, M. Y., "A Detailed Numerical Model of a Supersonic Reacting Mixing Layer," AIAA Paper No. 86-1427, June 1986.

4. Chitsomboon, T., Kumar, A., Drummond, J. P. and Tiwari, S. N., "Numerical Study of Supersnic Combustion Using a Finite-Rate Chemistry Model," AIAA Paper No. 86-0309, January 1986; also, Chitsomboon, T. and Tiwari, S. N., "Numerical Study of Hydrogen-Air Supersonic Combustion By Using Elliptic and Parabolized Equations," Progress Report NAG-1-423, Dept. of Mechanical Engineering and Mechanics, Old Dominion University, Norfolk, VA, August 1986.

5. Drummond, J. P., "Numerical Simulation of a Supersonic Chemically Reacting Mixing Layers," Ph.D. Dissertation, George Washington University, May 1987.

6. Sparrow, E. M. and Cess, R. D., Radiation Heat Transfer, Brooks/Cole, Belmont, Calif., 1966 and 1970. New Augmented Edition, Hemisphere Publishing Corp. Washington, D.C., 1978.

7. Cess, R. D. and Tiwari, S. N., "Infrared Radiative Energy Transfer in Gases," Advances in Heat Transfer, Vol. 8, Academic Press, New York, 1972.

8. Edwards, D. K., "Molecular Gas Band Radiation," Advances in Heat Transfer, Vol. 12, Academic Press, New York, 1976; also, Radiation Heat Transfer Notes, Hemisphere Publishing Corporation, Washington, D.C., 1981.

9. Tiwari, S. N., "Radiative Interactions in Transient Energy Transfer in Gaseous Systems," Progress Report NAG-1-423, Dept. of Mechanical Engineering and Mechanics, Old Dominion University, Norfolk, VA, December 1985.

10. Latko, R. J. and Pomraning, G. C., "Two-Dimensional Radiative Transfer by Synthesis Methods," Journal of Quant. Spectrosc. Radiant Transfer, Vol. 12, pp. 1-24, 1972.

11. Berg, W. F. and Crosbie, A. L., "Two-Dimensional Radiative Equilibrium," Journal of Mathematical Analysis and Application, No. 46, pp. 104-125, 1974.

12. Tsai, S. S. and Chan, S. H., "Multi-Dimensional Radiative Transfer in Nongray Gases-General Formulation and the Bulk Radiative Exchange Approximation," Journal of Heat Transfer, Vol. 100, pp. 486-491, August 1978.

13. Modest, M. F., "Evaluation of Spectrally-Integrated Radiative Fluxes of Molecular Gases in Multi-Dimensional Media," Journal of Heat and Mass Transfer, Vol. 26, No. 10, pp. 1533-1546, 1983.

14. Yuen, W. W. and Wong, L. W., "Analysis of Radiative Equilbrium in a Rectangular Enclosure with Gray Medium," Journal of Heat Transfer, Vol. 106, pp. 433-440, May 1984.

15. Hottel, H. C. and Cohen, E. S., "Radiant Heat Exchange in a Gas-Filled Enclosure: Allowance for Non-Uniformity of Gas Temperature," AICHE Journal, Vol. 4, No. 1, 1958, pp. 3-14.

16. Martin, J. K. and Hwuang, C. C., "Combined Radiant and Convective Heat Transfer to Laminar Steam Flow Between Gray Parallel Plates with Uniform Heat Flux," Journal of Quant. Spectrosc. Radiant Transfer, Vol. 15, pp. 1071-1081, 1975.

17. Viskanta, Appl. Scientific Res. A13,291 (1964).

18. Kobiyama, M., Taniguchi, H. and Saito, T., "The Numerical Analysis of Heat Tranfer Combined with Radiation and Convection," JSME, Vol. 22, No. 167, pp. 707-714, May 1979.

19. Im, K. H. and Ahluwalia, R. K., "Combined Convection and Radiation in Rectangular Ducts," Int. Journal of Heat and Mass Transfer, Vol. 27, No. 2, pp. 221-231, 1984.

20. Chung, T. J. and Kim, J. Y., "Two-Dimensional, Combined-Mode Heat Transfer by Conduction, Convection, and Radiation in Emitting, Absorbing and Scattering Media-Solution by Finite Elements," Journal of Heat Transfer, Vol. 106, pp. 448-452, May 1984.

21. Tiwari, S. N. and Singh, D. J., "Interaction of Transient Radiation in Nongray Gaseous Systems," Progress Report NAG-1-423, Dept. of Mechanical Engineering and Mechanics, Old Dominion University, Norfolk, VA, January 1987.

22. Tiwari, S. N. and Singh, D. J., "Interaction of Transient Radiation in Fully Developed Laminar Flows," AIAA Paper No. 87-1521, June 1987.

23. Soufiani, A. and Taine, J., "Application of Statistical Narrow-Band Model to Coupled Radiation and Convection at High Temperature," Int. Journal of Heat and Mass Transfer, Vol. 30, No. 3, pp, 437-447, 1987.

24. James, R. K. and Edward, D. K., "Effect of Molecular Gas Radiation on a Planar, Two-Dimensional, Turbulent-Jet-Diffusion Flame," Journal of Heat Transfer, Vol. 99, May 1977.

25. Rogers, R. C. and Schexnayder, C. J., Jr., "Chemical Kinetic Analysis of Hydrogen-Air Ignition and Reaction Time," NASA TP 1856, 1981.

26. Evans, J. S. and Schexnayder, C. J., Jr., "Influence of Chemical Kientic and Unmixedness on Burning in Supesonic Hydrogen Flames," AIAA Journal, Vol. 18, No. 2, pp. 188-193, February 1980.

27. Rogers, R. C. and Chinitz, W., "Using a Global Hydrogen-Air Combustion Model in Turbulent Reacting Flow Calculation," AIAA Journal, Vol. 21, No. 4, April 1983.

28. Bussing, T. R. A. and Murman, E. M., "A Finite Volume Method for the Calculation of Compressible Chemically Reacting Flows," AIAA Paper No. 85-0331, January 1985.

29. Seinfeld, J. H., Lapidus, L. and Hwang, M., "Review of Numerical Integration Techniques for Stiff Ordinary Differential Equations," Ind. Eng. Chem. Fundam., Vol. 9, No. 2, pp. 266-275, 1970.

30. Bui, T. D., Oppenheim, A. K. and Pratt, D. T., "Recent Advances in Methods for Numerical Solution of ODE Initial Value Problems," Lawrence Berkeley Laboratory Report No. LBL-16943, December 1983.

31. Smoot, L. D., Hecker, W. C. and Williams, G. A, "Prediction of Propagating Methane-Air Flames," Combustion and Flame, Vol. 26, 1976.

32. Stalnaker, J. F., Robinson, M. A., Spradley, L. W., Kurzius, S. C. and Theoeres D., "Development of the Genral Interpolants Methods for the Cyber 200 Series of Computers," Report TR 0867354, Lockhead-Huntsville Research and Engineering Center, Huntsville, AL, October 1983.

33. Jameson, A., Schmidt, W. and Turkel, E., "Numerical Solution of the Euler Equations by Finite Volume Methods Using Runge-Kutter Time-Stepping Scheme," AIAA Paper No. 81-1259, June 1981.

34. Turkel, E., "Accleration to a Steady State for the Euler Equations," ICASE Report No. 84-32.

35. Swanson, R. C. and Turkel, E., "A Multistage Time-Stepping Scheme for the Navier-Stokes Equations," AIAA Paper No. 85-0035, January 1985.

36. Swanson, R. C. and Turkel, E., "Artificial Dissipation and Central Difference Schemes for the Euler and Navier-Stokes Equations," AIAA Paper No. 87-1107-CP, June 1987.

37. Jones, R. A., Huber, P. W., "Toward Scramjet Aircraft," NASA CP-2065-Pt. 1, 1978, pp. 30-48.

38. Beach, H. L., "Hypersonic Propulsion," NASA CP-2092, 1979, pp. 387-407.

39. Williams, F. A., Combustion Theory, Second Edition, Benjamin/Cummings Publishing Company, Inc., Menlo Park, California, 1985.

40. McBride, B. J., Heimel, S., Ehlens, J. G. and Gorden, S., "Thermodynamic Properties to 6000K for 210 Substances Involving the First 18 Elements," NASA SP-3001, 1963.

41. Tiwari, S. N., "Moels for Infrared Atmospheric Radiation," Advances in Geophysics, Vol. 20, Academic Press, New york, 1978, pp. 1-85.

42. Tien, C. L. and Lowder, J. G., "A Correlation for Total Band Absorptance of Radiating Gases," International Journal of Heat and Mass Transfer, Vol. 9, July 1966, pp. 698-701.

43. Edward, D. K. and Menard, W. A., "Comparison of Models for Correlation of Total Band Absorptance," App. Optics, 3, 621, 1964.

44. Mani, M. and Tiwari, S. N., "Investigation of Chemically Reacting and Radiating Supersonic Internal Flows," Dept. of Mechanical Engineering and Mechanics, Old Dominion University, Norfolk, VA, Progress Report NAG-1-423, December 1986.

45. Mani, M. and Tiwari, S. N., "Numerical Solution of Chemically Reacting and Radiating Flows," AIAA Paper No. 87-0324, January 1987.

46. MacCormack, R. W., "The Effect of Viscosity in Hypersonic Impact Cratering," AIAA Paper No. 69-354, May 1969.

47. Smith, R. E. and Weigel, B. L., "Analytical and Approximate Boundary Fitted Coordinate System for Fluid Flow Simulation, AIAA Paper No. 80-0192.

48. Wilkin, J. H., The Algebraic Eigenvalue Problem, Oxford University Press, Oxford, England, 1965, pp. 233-236.

49. Householder, A. S., The Theory of Matrices in Numerical Solution Analysis, Dover Publication, New York, 1964, pp. 122-140.

50. Jameson, A. and Schmidt, W., "Some Recent Development in Numerical Methods For Transonic Flows," Computer Methods in Applied Mechanics and Engineering, North-Holland, pp. 467-493, 1985.

51. Jameson, A., "A Nonoscillatory Shock Capturing Scheme Using Flux Limited Dissipation," Lectures in Applied Mathematics, Vol. 22, 1985.

52. Chen, H. C., Yu, N. J., Rubbert, P. E. and Jameson, A., "Flow Simulations for General Narelle Configurations Using Euler Equations, AIAA Paper No. 83-0539, 1983.

53. Carter, J. E., "Numerical Solutions of the Navier-Stokes Equations for the Supersonic Laminar Flow Over a Two-Dimensional Compression Corner," NASA TR-R-385, July 1972.

54. Martinelli, L., Jameson, A. and Grasso, F., "A Multigrid Method for the Navier-Stokes Equations," AIAA Paper No. 86-0208 January 1986.

55. Chakravarthy, S. R., "Development of Upwind Schemes for the Euler Equations," NASA Contractor Report 4043 January 1987, Results of Viscous Flow was obtained by D. Ruddy at NASA Langley.

56. White, F. M., Viscous Fluid Flow, McGraw-Hill, Inc., 1974.

57. Eklund, D. R., Hassan, H. A. and Drummond, J. P., "The Efficient Calculation of Chemically Reacting Flow," AIAA Paper No. 86-0563, January 1986.

APPENDICES

APPENDIX A

DERIVATION OF CONDUCTION HEAT FLUX TERMS

To simplify Eqs. (2.3) to Eqs. (2.4), the Lewis number is assumed to be unity. This simplification is carried out in detail for Eq. (2.3b) and the same is applied to Eq. (2.3a). Using the expressions for the thermal diffusivity (α) and Lewis number (L_e), Eq. (2.3b) can be expressed as

$$\alpha = K/\rho\bar{C}_p$$

$$L_e = \alpha/D$$

$$q_{cy} = - \rho D \left(L_e \bar{C}_p \frac{\partial T}{\partial y} + \sum_{i=1}^{m} \frac{\partial f_i}{\partial y} h_i\right) \qquad (A.1)$$

Defining the binary diffusion coefficient D in terms of the Prandtl and Lewis number Eq. (A.1) can be expressed as

$$Pr = \nu/\alpha$$

$$D = \frac{\alpha}{L_e} = \frac{\nu/Pr}{L_e} = \frac{\mu}{\rho Pr\, L_e}$$

$$q_{cy} = - \frac{\mu}{Pr} \left[\bar{C}_p \frac{\partial T}{\partial y} + \sum_{i=1}^{m} \frac{\partial f_i}{\partial y} h_i\right] \qquad (A.2)$$

where

$$\bar{C}_p = \sum_{i=1}^{m} f_i C_{p_i}$$

The static enthalpy of the mixture is given by the relation

$$h = \sum_{i=1}^{m} [h_i^o + \int_o^T C_{p_i} \, d\eta] \, f_i \tag{A.3}$$

It should be noted that η is a dummy variable employed to evaluate the sensible enthalpy. Using the Leibnitz formula, Eq. (A.3) is differentiated to obtain

$$\frac{\partial h}{\partial y} = \sum_{i=1}^{m} [(h_i^o + \int_o^T C_{p_i}(\eta) \, d\eta) \frac{\partial f_i}{\partial y} + f_i \frac{\partial h_i^o}{\partial y}$$

$$+ f_i \int_o^T \frac{\partial C_{p_i}(\eta)}{\partial y} d\eta + f_i \, C_{p_i}(T) \frac{\partial T}{\partial y}] \tag{A.4}$$

The coefficients of the first differential on the right hand side is equal to h_i and the second and third terms are identical to zero, therefore, Eq. (A.4) reduces to

$$\frac{\partial h}{\partial y} = \sum_{i=1}^{m} [h_i \frac{\partial f_i}{\partial y} + f_i \, C_{p_i} \frac{\partial T}{\partial y}]$$

or

$$\frac{\partial h}{\partial y} = \sum_{i=1}^{m} h_i \frac{\partial f_i}{\partial y} + C_p \frac{\partial T}{\partial y} \tag{A.5}$$

Substituting Eq. (A.5) into Eq. (A.2), q_{cy} is expressed as

$$q_{cy} = - \frac{\mu}{Pr} \frac{\partial h}{\partial y}$$

or

$$q_{cy} = - \frac{\gamma \mu}{Pr} \frac{\partial e}{\partial y}$$

APPENDIX B

RADIATIVE FLUX EQUATIONS FOR NONGRAY GASES

In this appendix, Eqs. (3.27) and (3.28) are rearranged and written as they are expressed in [12]. The first integral in Eq. (3.27) can be written as

$$\int_0^y e_{\nu c}(y')A'(y-y')dy' = \int_0^y [e_{\nu c}(y') - e_{\nu c_1}] A'(y-y')dy'$$

$$+ e_{\nu c_1} \int_0^y A'(y-y')\, dy'$$

$$= \int_0^y [e_{\nu c}(y') - e_{\nu c_1}]A'(y-y')dy' - e_{\nu c_1} A(y-y')\Big|_0^y$$

$$= \int_0^y [e_{\nu c}(y') - e_{\nu c_1}]A'(y-y')dy' - e_{\nu c_1} A(0)$$

$$+ e_{\nu c_1} A(y) \qquad \text{(B.1)}$$

The second integral in Eq. (3.27) can be written as

$$\int_y^L e_{\nu c}(y')A'(y'-y)dy' = \int_y^L [e_{\nu c}(y') - e_{\nu c_2}] A'(y'-y)dy'$$

$$+ \int_y^L e_{\nu c_2} A'(y'-y)dy'$$

$$= \int_y^L [e_{\nu c}(y') - e_{\nu c_2}]A'(y'-y)\, dy' + e_{\nu c_2} A(y'-y)\Big|_y^L$$

$$= \int_y^L [e_{\nu c}(y') - e_{\nu c_2}]A'(y'-y')dy' + e_{\nu c_2} A(L-y)$$

$$- e_{\nu c_2} A \qquad (B.2)$$

Upon substituting Eqs. (B.1) and (B.2) into Eq. (3.27), the result can be written as

$$\vec{q}_r = e_1 - e_2 - e_{\nu c_1} A(y) + e_{\nu c_2} A(L-y) + \int_o^y [e_{\nu c}(y') - e_{\nu c_1}]A'(y-y')$$

$$+ e_{\nu c_1} A(y) - \int_y^L [e_{\nu c}(y') - e_{\nu c_2}]\, A'(y'-y)dy' - e_{\nu c_2} A(L-y) \qquad (B.3)$$

Equation (B.3) can be simplified to

$$q_r = e_1 - e_2 + \int_o^y [e_{\nu c}(y') - e_{\nu c_1}]A'(y-y')dy' - \int_y^L [e_{\nu c}(y')$$

$$- e_{\nu c_2}]A'(y'-y)\, dy \qquad (B.4)$$

Equation (B.4) is the same as Eq. (3.29) if it is written for multi-band gaseous system. The first integral in Eq. (3.28) can be written as

$$\int_o^y [e_{\nu c}(y) - e_{\nu c}(y')]A''(y-y')dy' = \int_o^y [e_{\nu c_1} - e_{\nu c}(y')]\, A''(y-y')dy'$$

$$- \int_o^y [e_{\nu c_1} - e_{\nu c}(y)]A''(y-y')dy'$$

$$= \int_0^y [e_{\nu c_1} - e_{\nu c}(y')]A''(y-y')dy' + [e_{\nu c_1} + e_{\nu c}(y)]\, A'(y-y')\Big|_0^y$$

$$= \int_0^y [e_{\nu c_1} - e_{\nu c}(y')]\, A''(y-y')dy' + [e_{\nu c_1} - e_{\nu c}(y)]A'(0)$$

$$- [e_{\nu c_1} - e_{\nu c}(y)]\, A'(y) \qquad \text{(B.5)}$$

The second integral in Eq. (3.29) can be written as

$$\int_y^L [e_{\nu c}(y) - e_{\nu c}(y')]A''(y'-y)dy' = \int_y^L [e_{\nu c_2} - e_{\nu c}(y')A''(y'-y)dy'$$

$$- \int_y^L [e_{\nu c_2} - e_{\nu c}(y)]A'(y-y')dy$$

$$= \int_y^L [e_{\nu c_2} - e_{\nu c}(y')]A''(y'-y)dy'$$

$$- [e_{\nu c_2} - e_{\nu c}(y)]A'(y'-y)\Big|_y^L$$

$$= \int_y^L [e_{\nu c_2} - e_{\nu c}(y')]A''(y'-y)dy'$$

$$- [e_{\nu c_2} - e_{\nu c}(y)]A'(L-y)$$

$$= [e_{\nu c_2} - e_{\nu c}(y)]A'(0) \qquad \text{(B.6)}$$

Substituting Eqs. (B.5) and (B.6) into Eq. (3.28) can be written as

$$\nabla q_r = [e_{\nu c}(y) - e_{\nu c_1}]A'(y) + [e_{\nu c}(y) - e_{\nu c_2}]A'(L-y)$$

$$- \int_0^y [e_{\nu c_1} - e_{\nu c}(y')]A''(y-y')dy'$$

$$- [e_{\nu c_1} - e_{\nu c}(y)]A'(0) + [e_{\nu c_1} - e_{\nu c}(y)]A'(y)$$

$$- \int_y^L [e_{\nu c_2} - e_{\nu c}(y')]A''(y'-y)dy'$$

$$+ [e_{\nu c_2} - e_{\nu c}(y)]A'(L-y) - [e_{\nu c_2} - e_{\nu c}(y)]A'(0) \qquad (B.7)$$

Equation (B.7) can be simplified and written as

$$\nabla q_r = [(e_{\nu c}(y) - e_{\nu c_1}) + (e_{\nu c}(y) - e_{\nu c_2})A'(0)$$

$$+ \int_0^y [e_{\nu c}(y') - e_{\nu c_1}]A''(y-y')dy' + \int_y^L [e_{\nu c}(y') - e_{\nu c_2}]A''(y'-y)dy' \qquad (B.8)$$

Equation (B.8) is exactly like Eq. (3.30) if it is written for a multi-band system.

APPENDIX C

COMPONENTS OF JACOBIAN MATRIX

In this appendix, the species matrix in the left hand side bracket of Eqs. (4.8) and (4.14) is evaluated. The source term is function of density, temperature and various species. In evaluating $\frac{\partial H}{\partial U}$, the density and temperature dependency is neglected for computational efficiency. Eklund et al. [57] evaluated the species Jacobian matrix with and without density and temperature dependency and found no difference in the steady state solutions. The components of Jacobian matrix are as follows:

$$H_i = \dot{W}_i = \dot{C}_i M_i$$

$$C_i = (\rho f_i / m_i) X_{10}^{-3} \quad \frac{g_m - mal}{Cm^3}$$

$$\frac{\partial \dot{W}_{O_2}}{\partial U_{O_2}} = - K_{f_1} C_{H_2} \tag{C.1}$$

$$\frac{\partial \dot{W}_{O_2}}{\partial U_{H_2O}} = 0 \tag{C.2}$$

$$\frac{\partial \dot{W}_{O_2}}{\partial U_{H_2}} = - K_{f_1} C_{O_2} \tag{C.3}$$

$$\frac{\partial \dot{W}_{O_2}}{\partial U_{OH}} = 2 K_{b_1} \frac{M_{O_2}}{M_{OH}} C_{OH} \tag{C.4}$$

$$\frac{\partial \dot{W}_{H_2}}{\partial U_{O_2}} = - K_{f_1} \frac{M_{H_2}}{M_{O_2}} C_{H_2} \tag{C.5}$$

$$\frac{\partial \dot{W}_{H_2}}{\partial U_{H_2O}} = 2 K_{b_2} \frac{M_{H_2}}{M_{H_2O}} C_{H_2O} \tag{C.6}$$

$$\frac{\partial \dot{W}_{H_2}}{\partial U_{H_2}} = - K_{f_1} C_{O_2} - K_{f_2} C_{OH}^2 \tag{C.7}$$

$$\frac{\partial \dot{W}_{H_2}}{\partial U_{OH}} = 2 K_{b_1} \frac{M_{H_2}}{M_{OH}} C_{OH} - 2 K_{f_2} \frac{M_{H_2}}{M_{OH}} C_{OH} C_{H_2} \tag{C.8}$$

$$\frac{\partial \dot{W}_{H_2O}}{\partial U_{O_2}} = 0 \tag{C.9}$$

$$\frac{\partial \dot{W}_{H_2O}}{\partial U_{H_2O}} = - 4 K_{b_2} C_{H_2O} \tag{C.10}$$

$$\frac{\partial \dot{W}_{H_2O}}{\partial U_{H_2}} = 2 K_{f_2} \frac{M_{H_2O}}{M_{H_2}} C_{OH}^2 \tag{C.11}$$

$$\frac{\partial \dot{W}_{H_2O}}{\partial U_{OH}} = 4 K_{f_2} \frac{M_{H_2O}}{M_{OH}} C_{OH} C_{H_2} \tag{C.12}$$

$$\frac{\partial \dot{W}_{OH}}{\partial U_{O_2}} = 2 K_{f_2} \frac{M_{OH}}{M_{O_2}} C_{H_2} \tag{C.13}$$

$$\frac{\partial \dot{W}_{OH}}{\partial U_{H_2O}} = 4 K_{b_2} \frac{M_{OH}}{M_{H_2O}} C_{H_2O} \tag{C.14}$$

$$\frac{\partial \dot{W}_{OH}}{\partial U_{H_2}} = 2 K_{f_1} \frac{M_{OH}}{M_{H_2}} C_{O_2} - 2 K_{f_2} \frac{M_{OH}}{M_{H_2}} C_{OH}^2 \tag{C.15}$$

$$\frac{\partial \dot{W}_{OH}}{\partial U_{OH}} = - 4 K_{b_2} C_{OH} - 4 K_{f_2} C_{OH} C_{H_2} \tag{C.16}$$

APPENDIX D

RADIATIVE FLUX EVALUATION FOR PSEUDO GRAY MODEL

This appendix shows the discretization and evaluation of the radiative flux for the y-direction. The same thing can be applied in the streamwise direction. Equations (3.17) and (3.18) in the y-direction are written as follows:

$$\frac{d^2 q_r(y)}{dy^2} - \frac{9}{4} K^2(y)\, q_r(y) = 3K(y) \frac{de(y)}{dy} \tag{D.1}$$

$$K(y)\,(\frac{1}{\varepsilon_1} - \frac{1}{2}) q_r(y) \Big|_{y=0} - \frac{1}{3} \frac{dq_r(y)}{dy} \Big|_{y=0} = 0 \tag{D.2}$$

$$K(y)\,(\frac{1}{\varepsilon_2} - \frac{1}{2})\, q_r(y) \Big|_{y=L} + \frac{1}{3} \frac{dq_r}{dy} \Big|_{y=L} = 0 \tag{D.3}$$

The above equations are discretized by central differencing. The second derivative of q_r in the physical domain is discretized as

$$\frac{d^2 q_r}{dy^2} \Big|_j = \frac{2}{\Delta y_j (1+\beta_j)} [\frac{q_{j+1} - q_j}{\beta_j \Delta y_j} - \frac{q_j - q_{j-1}}{\Delta y_j}] \tag{D.4}$$

where

$$\Delta y_j = y_j - y_{j-1} \quad \text{and} \quad \beta_j = \frac{y_{j+1} - y_j}{y_j - y_{j-1}}$$

Equations (D.1-D.3) in discrete forms are written as

$$\frac{2}{\Delta^2 y_j (1+\beta_j)} q_{j-1} - [\frac{2}{\Delta y_j (1+\beta_j)} (\frac{1}{\beta_j \Delta y_j} + \frac{1}{\Delta y_j}) + \frac{9}{4} K_j^2]\, q_j$$

$$+ \frac{2}{\Delta y_j^2 (1+\beta_j)\beta_j} q_{j+1} = 1.5\, K_j\, [\frac{e_{j+1} - e_j}{\beta_j \Delta y_j} + \frac{e_j - e_{j-1}}{\Delta y_j}] \tag{D.5}$$

$$\left[K_1\left(\frac{1}{\varepsilon_1} - \frac{1}{2}\right) + \frac{1}{3\Delta y_1}\right] q_1 - \frac{1}{3\Delta y_1} q_2 = 0 \qquad (D.6)$$

$$-\frac{1}{3\Delta y_J} q_{J-1} + \left[\left(\frac{1}{\varepsilon_2} - \frac{1}{2}\right) K_J + \frac{1}{3\Delta y_J}\right] q_J = 0 \qquad (D.7)$$

The above can be written in matrix form as

$$\begin{bmatrix} A & B & 0 & \cdots & 0 \\ C & A & B & 0 & \cdots & 0 \\ \vdots & & 0 & C & A & B \\ 0 & \cdots & & 0 & C & A \end{bmatrix} \begin{bmatrix} q_{r_1} \\ \vdots \\ q_{r_{J-1}} \\ q_{r_J} \end{bmatrix} = \begin{bmatrix} R_1 \\ R_2 \\ \vdots \\ R_J \end{bmatrix} \qquad (D.8)$$

where

$$A_{1,1} = K_1 \left(\frac{1}{\varepsilon_1} - \frac{1}{2}\right) + \frac{1}{3\Delta y_1}$$

$$A_{i,j} = -\left[\frac{2}{\Delta y_j(1+\beta_j)}\left(\frac{1}{\beta_j \Delta y_j} + \frac{1}{\Delta y_j}\right) - \frac{9}{4} K_j^2\right] ; \quad j = 2, J-1$$

$$A_{I,J} = K_J\left(\frac{1}{\varepsilon_2} - \frac{1}{2}\right) + \frac{1}{3\Delta y_J}$$

$$B_{1,2} = -\frac{1}{3\Delta y_1}$$

$$B_{i,j} = \frac{2}{\Delta y_j^2(1+\beta_j)\beta_j} \qquad j = 3, J$$

$$C_{i,j} = \frac{2}{\Delta y_j^2(1+\beta_j)} \qquad j = 2, J-2$$

$$C_{i,J-1} = -\frac{1}{3\Delta y_J}$$

$$R_1 = 0.$$

$$R_j = 1.5\ K_j\left[\frac{e_{j+1} - e_j}{\beta_j\ \Delta y_j} + \frac{e_j - e_{j-1}}{\Delta y_j}\right] \quad j = 2, J - 1$$

$$R_J = 0.$$

The tri-diagonal matrix on the left hand side of Eq. (D.8) is solved efficiently by the Thomas algorithm.

APPENDIX E

BOUNDARY CONDITIONS FOR ADIABATIC WALL TEMPERATURES

The adiabatic wall condition is given as

$$\left.\frac{\partial T}{\partial y}\right|_{y=0} = \left.\frac{\partial H}{\partial t}\right|_{y=0} = 0 \tag{E.1}$$

Substituting for the total enthalpy, its gradient is written as

$$\left.\frac{\partial H}{\partial y}\right|_{y=0} = \left.\frac{\partial}{\partial y}\left(C_p T + (u^2 + v^2)/2\right)\right|_{y=0} = 0 \tag{E.2}$$

The velocity terms (u, v) are equal to zero at the boundary for the viscous fluid. Assuming specific heat is a constant Eq. (E.2) reduce to

$$\left.\frac{\partial H}{\partial y}\right|_{y=0} = C_p \left.\frac{\partial T}{\partial y}\right|_{y=0} \tag{E.3}$$

Specific heat is a constant, therefore, temperature gradient must be equal to zero. For Pr = 1 total enthalpy remain constant, while for variable Prandtl number total enthalpy changes, the gradient remains very small. Therefore, at the solid boundary, one can enforce the zero enthalpy gradient by setting

$$H_w = H_1 \tag{E.4}$$

Substituting the relation for total enthalpy Eq. (E.4) is written as

$$C_p T_w = C_p T_1 + (u_1^2 + v_1^2)/2 \tag{E.5}$$

Therefore, the adiabatic wall temperature can be approximated by

$$T_w = T_1 + (u_1^2 + v_1^2)/2\ C_p \ . \qquad (E.6)$$

BIOGRAPHY

Mortaza Mani was born on August 26, 1954, in Isfahan, Iran. He received his high school diploma from Saadi High School in May of 1972. In December of 1977, he received his B.S. in mechanical engineering from Kansas State University in Manhattan Kansas. The following January he joined The Babcock and Wilcox Company in Barberton, Ohio, where he designed boilers for power plants.

In the fall of 1980 he returned to Kansas State University to pursue a graduate degree in engineering; his M.S. in mechanical engineering was earned in December 1982. He entered the Ph.D. program at Old Dominion University in Norfolk, Virginia in 1983. There, he was in the ICAM program, a graduate program between Old Dominion University and NASA Langley Research Center.

In February 1988, he jointed MacDonnell Douglas Aircraft Company in St. Louis, Missouri. He is married to Marcia Mani and has two children, Rosaly and Camran.